4   CSX: COHERENT SOFT X-RAY BEAMLINE

4.1   Executive Summary

The coherent soft x-ray beamline design described in this chapter is state-of-the-art and will be able to fully exploit the brightness and flux provided by the NSLS-II storage ring. The source, an EPU45 Elliptically Polarizing Undulator, will allow full control of the polarization (circular and linear) of the incident photons. The beamline optics design will either preserve this polarization or, additionally, will allow fast-switching of the polarization state of the photon beam on the sample. In addition to providing very high photon flux at high energy resolution, the beam on sample will have a high degree of transverse spatial coherence.

The current design, presented here, will satisfy the requirements of "photon hungry" experiments that demand high photon flux ($\sim 10^{13}$ photons/sec), at high resolving power ($\sim 10^4$), coherent (a few transverse modes), focused into a small spot (~ 1.5 μm x 3μm 1-σ).

4.2   Scientific Objective

The scientific motivation for this beamline is that its superior properties will expand the very exciting field of "photon hungry" experiments that currently are limited by their long acquisition times. This set of experiments includes any the uses the coherent part of the photon beam, such as coherent diffraction, phase retrieval imaging using coherent scattering, coherent based microscopy, phase contrast microscopy, and STXM. In addition and in particular, soft X-ray Photon Correlation Spectroscopy (XPCS) experiments demand very high coherent photon flux and have been severely limited by count rates available to date. In a different direction, but equally important, are the studies driven by a scientific case or interest in the understanding of the properties of new materials or artificially engineered systems. Examples of those systems are highly diluted materials, the study of micrometer size single crystals, nanosized-materials and interfaces. Obviously these systems could also be studied using the previously cited techniques, but in many cases other experimental techniques, so called standard, will provide with more precise information about their specific properties.

In general, either justifying the beamline from a technique or the scientific motivation point of view, a beamline working in the soft x-ray energy range will dramatically enhance its scientific capabilities with the possibility to select the incident polarization. This is a characteristic that in the past ten years has been extensively proven in the study of soft-matter and magnetic materials.

The beamline has been designed to host experiments in the soft x-rays energy range from 200eV to 2000eV requiring high coherent photon flux   The current CSX beamline design provides high photon flux ($\sim 10^{13}$ photons/sec), at high resolving power ($\sim 10^4$), coherent (a few transverse modes), focused into a small spot (~ 1.5 μm x 3μm 1-σ). Taken together, the CSX beamline performance is expected to be better than any other soft x-ray beamline currently operational in the US.

4.3   Insertion Device

This insertion device chosen for the CSX beamline is a pair of 45mm-period Elliptically Polarizing Undulators (EPU45's) that can operate either as one insertion device (same gap and polarization) or in canted mode, where the two EPU45's, separated in angle by ~0.16 mrad, can provide a beam with different polarization. Having two statically-canted (in horizontal angle) insertion devices allows one to control the

polarization switching rates outside the storage ring by the use of a mechanical chopper that selects beam from one of the EPU45's at a time. The switching rate for such a chopper can be quite high, up to kHz rates. Use of switching rates from 10 Hz to 1 kHz are well matched to lock-in technique detection techniques. The use of the lock-in technique has been demonstrated to be very effective in the detection of small signals from magnetic systems, especially in highly dilute samples.

4.4   Sector Layout

4.4.1   Front-End Layout

This is a soft x-ray beamline that will operate windowless and under ultrahigh vacuum conditions. Under these conditions there is no need for a differential pumping section in the front end, although one could be included in order to provide an extra degree of vacuum protection. A 15 mm-square fixed aperture will be located at 18.25 m from the center of the insertion device straight section. Non-absorbing type x-ray beam position monitors (XBPM) should be located at approximately 18.85 meters and 24.15 meters from the center of the straight. An adjustable white beam aperture should be located in the section between the fast gate valve and the second beam position monitor, to define the beam size in real time.

4.4.2   Beamline Layout

The equipment layout for this beamline allows many options. Before discussing the details of the equipment it will be helpful to have an overview of the beamline and define some names. There are three undulator configurations and two branches allowing six major modes of operation. The undulators could be configured to provide one straight beam, two canted circularly polarized beams (upstream and downsteam), two canted linearly polarized beams (upstream and downstream). It would also be possible to configure the accelerator so the beam is steered alternately though the two undulators producing a straight beam with time dependant polarization oscillations. While this case was considered, the decision was made to complete this conceptual design considering the constant **canted** and **straight** cases. For any undulator configuration the beam(s) can be directed along the **short** branch with the branching mirror retracted or along the **long** branch by deflecting off the branching mirror.

The CAD model in Figure 4.1 show an isometric overview of the beamline from the ratchet wall to the end of the short branch. Figure 4.2 shows a side view and Figure 4.3 a top view. Starting at the ratchet wall the major components are:
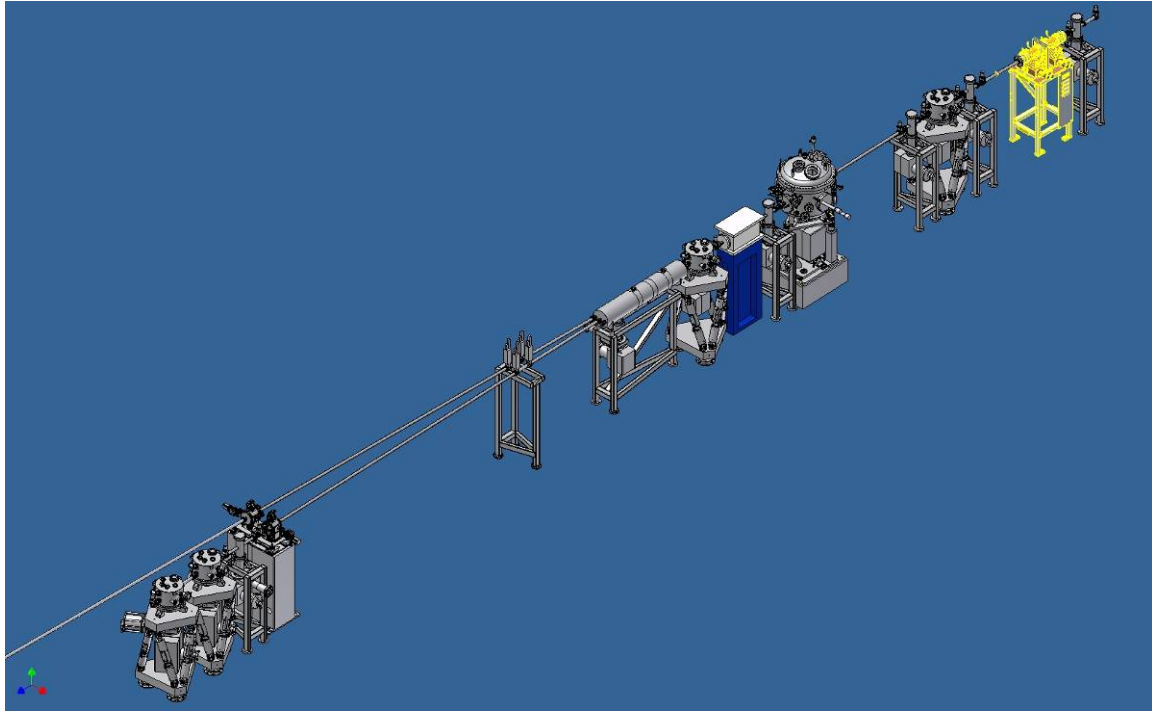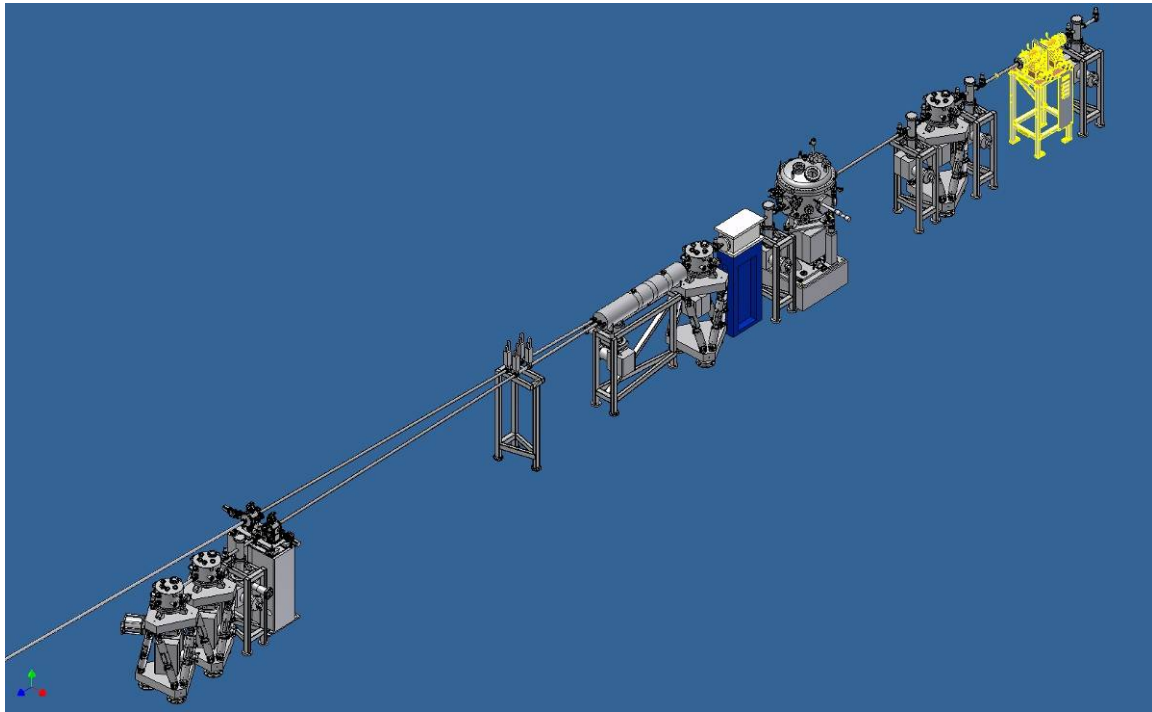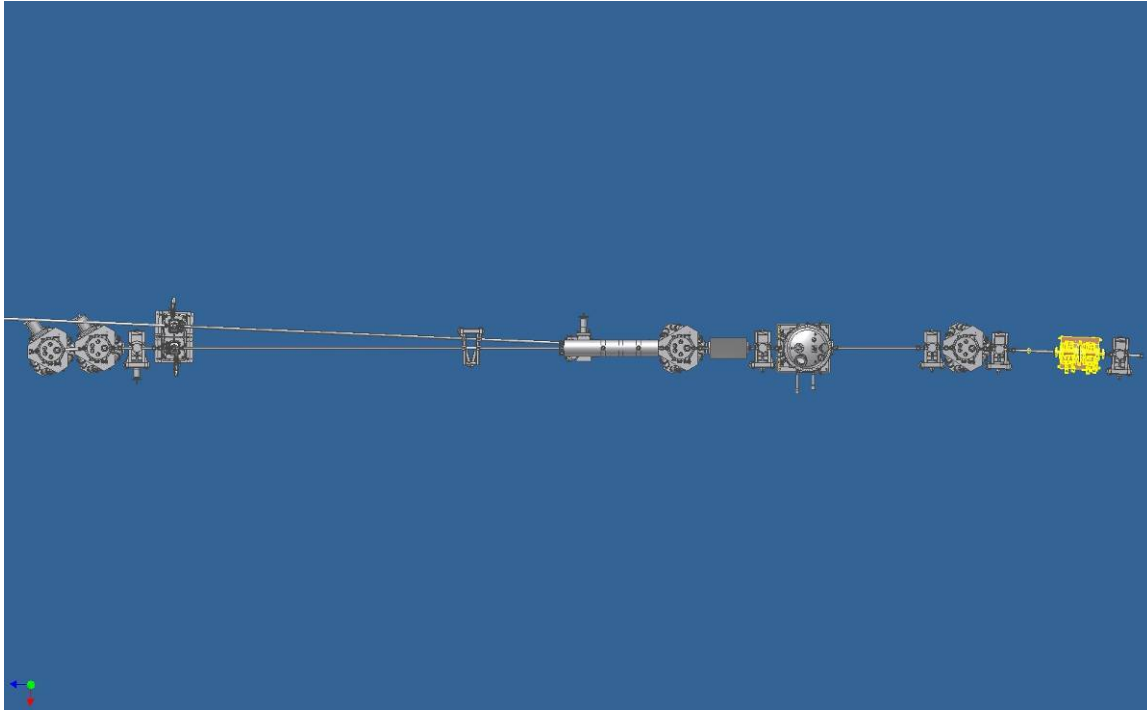
Figure 4.1

Figure 4.2

Figure 4.3

White Beam Aperture – rough beam sizing and power absorption

M1 – absorbs high energy beam reducing heat load on downstream optics and collimates the beam vertically

Monochromator – uses M2 and one of three gratings to vertically focus a selected energy on the slit

Chopper – blocks alternating polarizations when operating in canted mode

Branching Mirror – allows diverting the beam into the long branch. Each branch has the following components

Exit Slits – allows the selected energy radiation to pass to the refocusing optics

Beam Defining Slits and Gas Cell – combined chamber allow sizing of the beam, measurement of photon current, and energy calibration

M3 – Horizontal refocusing mirror

M4 – Vertical refocusing mirror

End Station

The mirrors along the beamline are supported with hexapod mounts. To the extent possible these will be made the same and share common mirror boxes. A close up of a hexapod with mirror box, pump, and valves for M3S and M4S can be seen in Figure 4.4.
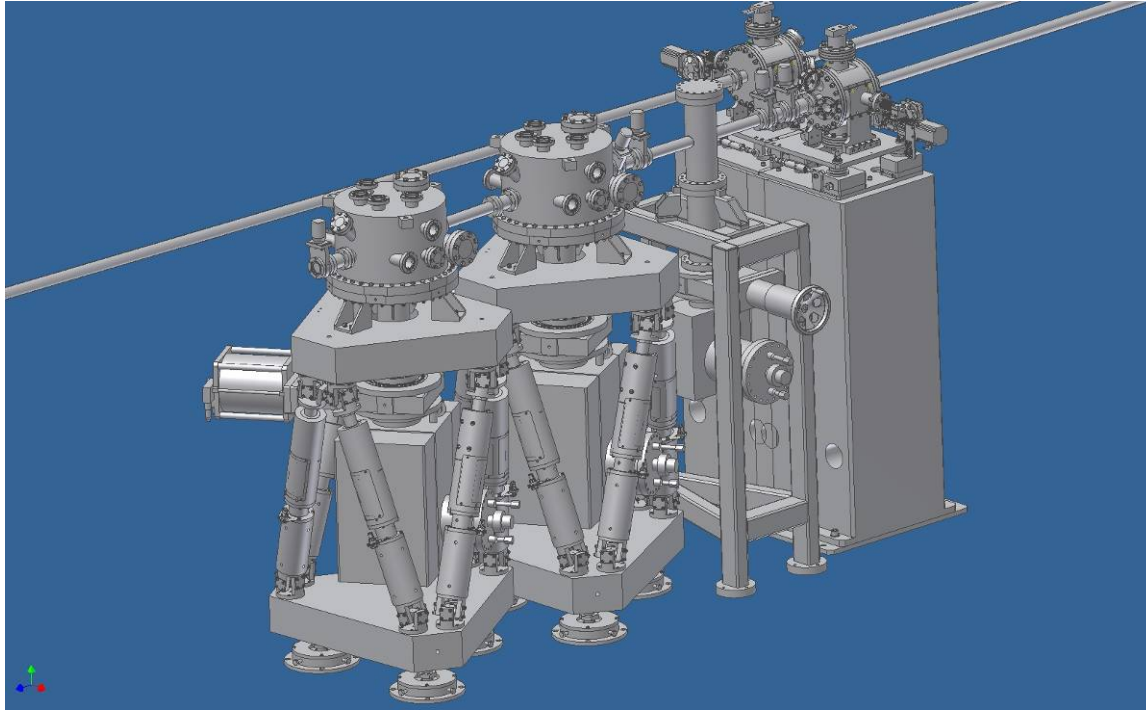
Figure 4.4

Diagnostic chambers are also standardized and placed between mirrors. in the diagnostic chambers shown in the drawings are missing many ports. The design contemplates the use of a Kimball Physics expanded sphere cube as the basic element adding the necessary equipment to the different available ports.. The space between the exit slit and the short M3 is very cramped to include beam defining slits, a gas cell, and a diagnostic chamber. The exit slit was moved as far downstream as possible to maximize the resolution and M3 was moved upstream as far as possible to maximize the space for the end station. The gas cell is included in the diagnostic chamber in front of M3. While it may be possible to fit the beam defining slits in as well, it would be more prudent to move M3 0.5 m downstream in the next design pass. In this CAD model we have only shown the beam defining slit chamber on the long line.

    i) CAD model of beamline and hutch layout.

    ii) Appropriate shadow model of beamline

4.4.2.1   Survey and Alignment Plans

All beamline components will be surveyed and aligned in place by the facility. In order to facilitate ease of alignment, all components will be fiducialized to external reference points on their table during assembly. All components are designed with a liberal tolerance allowance greater than 0.5 mm.

4.4.2.2   Utility Layouts

The utilities will require the coordination between the beamline and the project infrastructure. At this point in the beamline design the goal is to identify the utility requirements at a high level. Appendix C, List of Key Components, has a spreadsheet with some columns included for utility requirements. Here is a brief summary.

Cooling will be all by chilled water. The total beam heat load of about 12 kW should end up in the cooling

water. There is also the need of cooling for vacuum components including pumps and Titanium sublimator pumps (TSP). The system is envisioned to be a pressurized supply pipe of good quality water and a return pipe supplied by the lab infrastructure. This water should be low-conductivity (LC) to allow electrical isolation of cooled parts. If the water provided by the lab is not LC water, then a separate deionizing and water circulation system will be need for the beamline. The beamline will need about 24 taps into the supply and return for cooling loops. 3 of these taps would go to heat exchangers for separate temperature controlled loops for M1, M2, and the gratings. If we need to cool these below room temp a compressor-based chiller could be added to each of these loops. No cryogenic cooling is envisioned for this beamline. There will be cryogenic requirements for the end stations.

Electricity will be primarily 120 V 60 Hz, but it would be beneficial to have access to 240 V. A rough estimate is 91 duplex 120 V outlets and 9 outlets at 240 V. It would be convenient to have some clean power available in a subset of these outlets. Some of these outlets should be provided with UPS protection. Pneumatics will be required for valve actuation. This could be a pipe with local taps for valves. A rough estimate is 29 air taps. Some of these will be critical safety systems so need to be guaranteed pressure. If the project does not supply this there should be a N2 backup system to guarantee valve operation.

4.4.2.4   Beamline Vacuum System

The details of the design do not allow detailed vacuum calculations. Using the experience of Diamond I06 as a guide, each mirror box was fitted with a 500 l/s pump with TS(After consultation with Diamond beamline responsible beamline I06 does not have the TSPs and wishes they did). Smaller 150 l/s ion pumps were placed at each of the diagnostic chambers, chopper, exit slits, gas cells, and long transport lines. A valve was placed between the chambers and the pumps to allow isolation of the pumps while working on the chamber. These were cost as metal valves. Potentially some of the valves could be changed to O-ring or eliminated. In the spreadsheet of Appendix C, List of Beamline Components, there are columns detailing pump and gauge locations. Each chamber with a pump was fit with a cold cathode gauge. There is a controller for each 6 gauges. Each mirror box was fit with an RGA head. There is one RGA controller. Additional piezo axis on the mirrors may limit the bakeout temperatures to 110 C as they did at Diamond. It would be good to find a work around for this.

There are three fast isolation valves associated with this beamline. One is in the standard front end. There is one on each line between the branching mirror and the exit slit. In the final design there will need to be enough vacuum impedance down steam of these valves to allow leak detection and valve actuation before the pressure wave reaches the valve. The distances between the endstations and the branch valves are long enough that this is not expected to be a problem. The location of the valve in the front end is not defined, but the beamline will have appropriate restriction to insure 15 ms of shutting time if there is a leak in the white beam apertures. Pressure sensing switches were included in each mirror box and the white beam apertures. They should also be included in the end stations as well. The control of these valves will be through the EPS system

4.4.3   Beamline Components

The major beamline components are discussed in this section. Table QQQ covers all the optics and provides information on position, size, spot size, thermal load, and distortion requirements. In the discussion below the numbers for location are referenced from the center of the straight which is the source for the linear straight mode of operation. The mirror sizes referenced are the size of the good optical surface so actual physical size may be larger to accommodate manufacturing. Some ray tracing results are included below but the original reports from Ruben Reininger can be found in appendix A.

Mirror Summary - NSLS-II Soft X-ray Coherent Beamline

Mirror Name	Beam from Source Radius/Wall	Mirror Material	Source Position Cooling	Along Beam	Bend Plane	Figure Required - D Length urad	Width urad	Bend Angle	Heat Absorbed B 5.2mm@M1 Beam Size - E 183eV Total W	Density W/mm^2	Sigma Y W mm	X Sigma W mm	Heat Absorbed C 3.0mm@M1 Density W/mm^2	Total W	Heat Absorbed C 4.0mm@M1 Mirror Size LEG Length Slit Total W	Width	Shape and Properties	Heat Absorbed C 7.1mmx5.2mm @M1 183eV Total W	Density W/mm^2
M0	No Longer in Beamline																		
M1 central	Silicon 2.80	Internal 29.50	Horz	0.25		8		966.558 88.75	0.9221 0.864	1900 @183eV 47.617	0.92 250	50	Sagital Cylinder	1160 mm rad	1287.08 mm rad			
M1 upstream									0.9828	47.935	250	50	1338.89 mm rad					
M1 downstream									0.9066	44.543	250	50	1234.89 mm rad					
M2	Silicon 5.13	Internal 31.85	Vert	0.17		3.5 @183eV, 150l/mm -A @2.3keV, 400l/mm -A @183eV, 1200l/mm -B		101.624 87.11 88.725 84.012	0.3653 1.2150 1.1331	236 17.945 21.853 @183Ev	0.36 380	50	Planar	132				
Grating LEG	Silicon 5.30	Edge 32.00	Vert	0.13		5.5 @183, 150l/mm -A @2.3keV, 400l/mm -A		1.8125 87 69, 86.53 88 98, 88.47 86 24, 81.73	0.0041 1.1267 1.1388	40 21.425 @LEG 27.550eV	0.06 130	25	a0 l/mm 150	a1 l/mm^2 0.0540	a2 l/mm^3 8.09E-06	c ~1.5		
Grating MEG		32.00									130	25	400	0.1438	2.15E-05	~1.5		
Grating HEG		32.00									130	25	1200	0.3018	4.51E-05	~2.2		
BM	Silicon 7.30	Edge 34.00	Horz	0.22		8.8		88.70	1.1532	33.745		3 10	0.004 Planar 0.24					
SLIT	15.30	42.00							1.4784 1.4804	0.00846 0.00573								
M3S central	Silicon 16.50	None 43.20	Horz	0.17		14		88.5	0.1560 0.2017	69.421 66.822	0.30 350	50	0.002 2.2E-05 Plane Elliptical - Bimorph 0.30 x 138.0 spot (1 sigma) 22479 mm rad	189.68 mm rad				
M3S downstream									0.1417	68.144	350 0.002	50	23128 mm rad 2.3E-05 23823 mm rad	191.51 mm rad 186.8 mm rad				
M4S	Silicon 17.25	None 43.95	Vert	0.37		14		88.5	0.8672 0.9627	11.589 13.224	75	50 0.008	Plane Elliptical - Bimorph 18414 mm rad	30.463 mm rad				
End Station S	18.25	44.95							0.00188 0.00205	0.00269 0.00248			0.0038 x 0.0054 spot (1 sigma)					
M3L central	Silicon 24.50	None 51.20	Horz					88.5			450	50	Plane Elliptical - Bimorph 26600 mm rad	220.75 mm rad				
M3L downstream	Silicon	None							1.2742	75.034	450	50	25950 mm rad	217.93 mm rad				
M4L																		
End Station L	26.50	53.20							0.00188 0.00164	0.00046 0.00047			5600 mm rad	69.67 mm rad				

Reference Sources - all by Ruben Reininger

A	Traces 070827.pdf	APPLE II, 85 Period, 45 mm/period, 183eV, X=46.4 um, Y=37.2 um, dX=35.1 urad, dY=29.2 urad
B		5.2 mm square apperture at 29.5 m, 183eV, 1200l/mm (HEG), Zeiss drawing lower case
C	Power, deformations 0709	Various cases with different appertures and gratings
D	Slope Errors 070904.doc	Limits required so resulution, horizontal spot and vertical spot do not degrade by more than half the
E	Traces 070911.doc	Canted Beam cases

4.4.3.1   White Beam Apertures

The power produced by the undulators is about 12 kW with power densities up to 40.1 kW/mrad^2. The white beam apertures, located at 28 m, would see a power density of up to 51 W/mm^2. They will have sufficient cooling to be able to absorb 12 kW at these power densities. An appropriate choice for these would be the IDT design used at Diamond. This consists are two water cooled copper cylinders with tapered square holes mounted on a translation stand. One cylinder is translated to define the bottom and right edge of the beam while the other is translated to define the top and left edge of the beam. The cylinders are water cooled but there are no water joints exposed to vacuum. This design has been used at Diamond I06 at similar power levels. The aperture needs to be adjustable to allow a spot size as large as 7.1 mm vertically (to over illuminate M2 for thermal stability) and 9.5 mm horizontally (canted beam case). The Diamond set incorporates some tungsten to help better define the beam.

4.4.3.2   M1 Mirrors

The first mirror makes a horizontal bend of 2.5° (88.75° from normal) so it absorbs a considerable amount of power passing only the softer X-rays to the downstream optics. With a 7.1 x 5.2 mm beam in the M1 plane at 29.5 m the mirror absorbs 1160 W with the undulators in the straight mode and adjusted for 183 eV. This gives a maximum power density of 0.92 W/mm2. These mirrors will be cylindrically ground to vertically collimate the beam. Thermal distortions in the length direction (meridional) beyond 0.25 µrad will increase the size of the horizontal beam spot and in the width direction (sagittal) beyond 8 µrad will decrease the energy resolution. Internally water cooled silicon mirrors have been selected for the M1s to provide the maximum thermal control. Cryogenic cooling would provide better thermal stability due to the lowered coefficient of thermal expansion (CTE) and the improved thermal conductivity of silicon at low temperatures, but with soft X-rays even a small layer of ice build up is a problem. Thermal modeling done for the Diamond I06 beamline showed expected rms slope errors of 20 µrad sagittally and 3 µrad meridionally at similar power levels (0.92 W/mm2) for an internally cooled silicon mirror. Preliminary ray tracing results have shown that this level of distortion can be compensated for by adjusting the operating angles of the monochromator and curvature of the M3 optic. Reduction of the levels of distortion may be obtained by reducing the coolant temperature enough to gain some improvements in silicon properties but not enough to produce ice build up. Both the optical correction and distortion minimization need further study to insure thermal distortions in M1 do not significantly reduce the beamline performance. The use of an M0 mirror before M1 was investigated. To split the power between the two mirrors, the M0 would need to be at a very shallow angle. This makes the mirror very large, expensive, and prone to distortion at the high power levels. There was significant cost saving in eliminating this option.

There are three M1 mirrors in this design. One for the straight operation mode and two (an upstream and a downstream) mirrors for the canted operation mode. Several options were considered to reduce the number of mirrors and some of these options may end up working. However, the three mirror option is the only one we could adequately verify during this design pass. It may be worthwhile to reopen this issue when answers to some of the accelerator related questions can be definitively answered. The three mirrors have slightly different shapes because the distance to the source varies between the operation modes. The size of the M1 mirrors was set to 250 mm long x 50 mm wide. This length is 5 σ from the expected spot size for a 5.2 mm horizontal beam size in the plane at 29.5 m. Figures QQQ, QQQ, and QQQ produced by Ruben Reininger show the expected spot on M1 with undistorted optics for the straight, canted upstream, and canted downstream configurations. Internally cooled silicon mirrors of this size with the required ~1300 mm sagittal cylindrical radius and meridional figure slope error of 0.5 µrad rms are within the normal manufacturing capability of InSync. This beamline requires meridional figure slope error of 0.25 µrad rms which may

require the addition of profile coating to the process. Detailed thermal modeling may show a longer mirror would be useful to reduce the effects of distortion at the ends of the heated stripe. The width should be enough to allow multiple stripes to be used. Wider mirrors would increase the vertical movement requirement to switch between the straight and canted modes (see below).
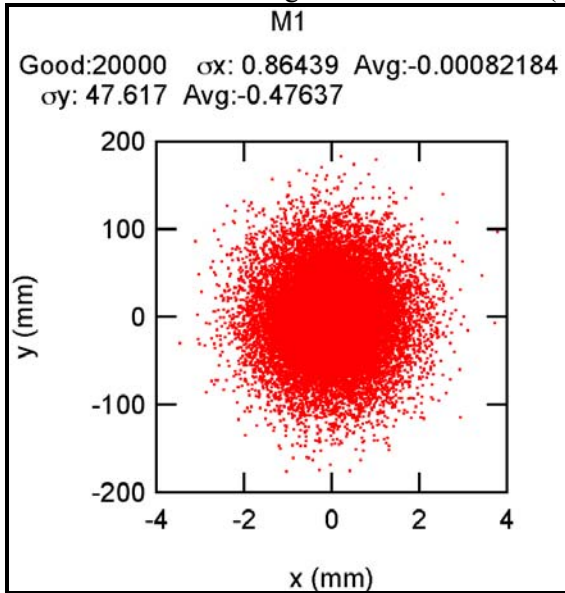

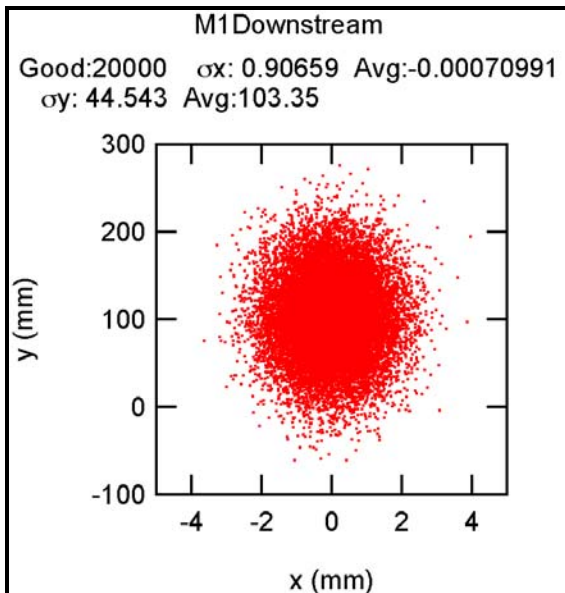**Figure 4.1.** M1 illumination, undulator 183eV linear straight mode

Figure 4.2. M1 illumination, undulator 230eV circular canted mode
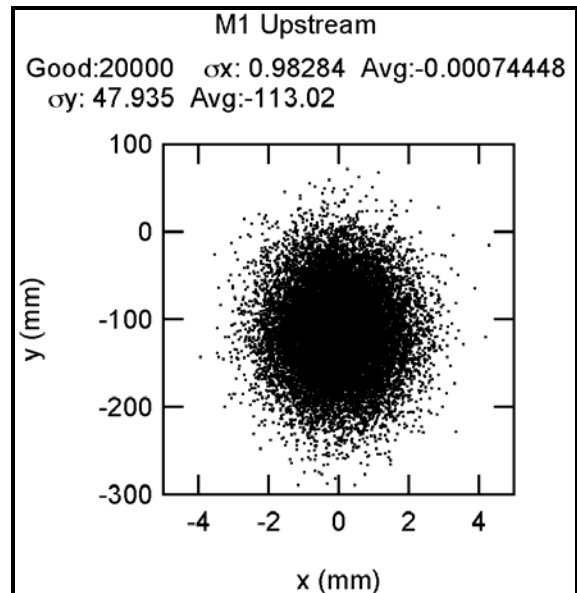
Figure 4.3. M1 illumination, undulator 230eV circular canted mode

The support system for mirrors is a hexapod system. The hexapods build by Oxford Danfysik for the Diamond I06 beamline would be a good choice. By standardizing on a flexible support the beamline will be easier to install, maintain, and operate. Controlled changes to the lengths of the six supporting legs can

Figure 2 M1 illumination, undulator 230eV circular canted mode

provide translations and rotations about convenient axis. The repeatability of motion is 1 μm and 2 μrad at the 2 σ level. This would be sufficient for single mirror alignment requirements except the bending angle. For this, additional piezoelectric axes in the vacuum chamber will be used. In the canted beam case the first mirror can be aligned with the hexapod, but the second mirror will require additional alignment. The second mirror will be fit with four in vacuum axes. With detailed study of the kinematics of the hexapod and alignment sensitivities it may be possible to reduce this number. The large translation required to change between the one mirror straight mode and the two mirror canted mode is outside the normal 25 mm range of the hexapod. A larger range can be accommodated but at some loss in repeatability. If the repeatability degradation is too large an additional vertical axis may be required. This will need additional study. The stiffness (vibration modes) of the hexapods has proven adequate for operation at Diamond I06 with similar requirements.

4.4.3.3　　Monochromator

The beam enters the monochromator, makes an upward vertical bend at the M2 mirror and then another vertical bend at one of the three variable line spaced gratings. The angles of the M2 and gating are set so the beam exiting horizontally with a 15 mm vertical offset (aimed at the exit slit) is of the selected energy. The line spacing of the grating is set so the light of the selected energy hitting the bottom of the grating is exiting at a slightly upward direction and the light of the selected energy hitting the top of the grating is exiting at a slightly downward direction thus focusing the light to a minimum vertical size at the exit slit. There are three sets of grating, LEG 150 l/mm, MEG 400 l/mm, and HEV 1200 l/mm to allow a trade off between energy resolution and delivered photons. Consideration was given to adding a fourth grating position with a spherical mirror to direct a "hot pink" beam to the experiment station. The decision was made that the 150 l/mm grating could provide enough pink beam power by opening the exit slit to the desired size. This keeps the number of gratings to three allowing use of more standard monochromator designs and reduces concerns for heating of downstream optics.

The M2 mirror makes a vertical bend of 12.0° (84.01° from normal) when operating at 183eV with the HEG grating so it absorbs a considerable amount of power passing only the softest X-rays to the downstream optics. With a 5.2 x 5.2 mm beam in the M1 plane at 29.5 m the M2 mirror absorbs 102 W with the undulators in the straight linear mode and adjusted for 183 eV. This gives a maximum power density of 0.36 W/mm2. M2 is a flat mirror that does no intentional focusing. Thermal distortions in the length direction (meridional) beyond 0.17 μrad will reduce the energy resolution and in the width direction (sagittal) beyond 3.5 μrad will increase the horizontal spot size. Internally water cooled silicon mirrors have been selected for the M2 to provide the maximum thermal control. Cryogenic cooling would provide better thermal stability due to the lowered coefficient of thermal expansion (CTE) and the improved thermal conductivity of silicon at low temperatures, but with soft X-rays even a small layer of ice build up is a problem. Thermal modeling was done with Finite Element Method by Ken Kriesel. A detailed report can be found in Appendix E. The thermal load produces a raised bump on the M2 surface. This bump has the largest slope changes near the ends of its length. With a beam size of 5.2 mm square at M1 the ends of the thermal bump on M2 are still part of the active optical path and greatly degrade the vertical optical performance doubling the vertical beam size at the exit slit. Increasing the aperture to 7.1 mm vertically increases the total heat load on M2, but moves the high slope areas out of the active optical path. The remaining thermally induced distortions can be corrected. The figure change in the central part of the M2 thermal bump can be approximated by a convex radius of ≈1.8×107 mm, which means the beam incident on the grating is not vertically collimated as in the optical design. This change in the virtual source position can be corrected by operating the grating with a c value of 2.193 instead of the nominal value of 2.184 at this energy. This change in operation essentially restores the vertical size of the beam at the exit slit. While 183eV appears to be the worst case, further work needs to be done to verify that this correction method can be done at higher beam energies. The horizontal distortion of M2 increases the horizontal spot size at the end station. The plan is to correct this by changing the shape of

the focusing mirror. The M3 and M4 mirrors are planned to be bimorphs. Preliminary work suggests that this method will work. Reduction of the levels of distortion may be obtained by reducing the coolant temperature enough to gain some improvements in silicon properties but not enough to produce ice build up. Both the optical correction and distortion minimization need further study to insure thermal distortions in M2 do not significantly reduce the beamline performance.
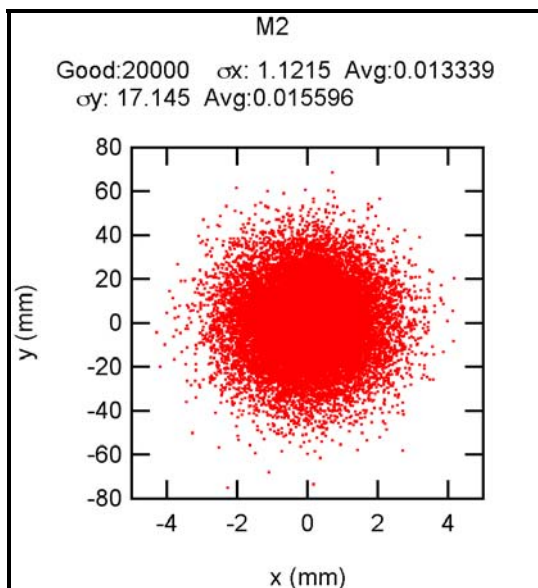

Figure 4.4. M2 mirror illumination, undulator 183eV linear straight mode
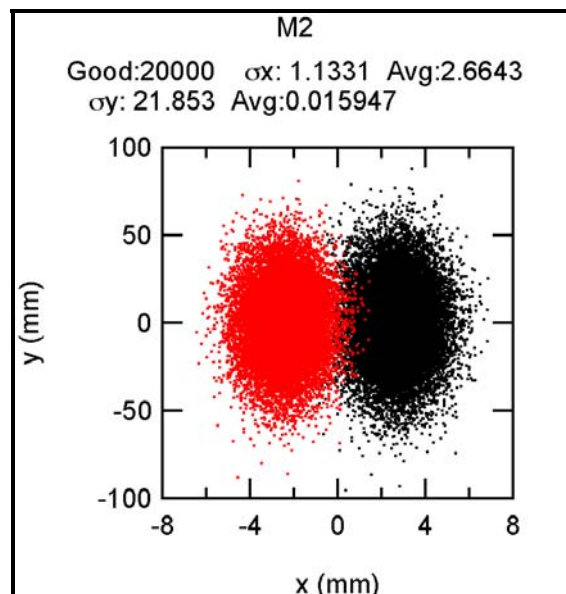
Figure 4.5. M2 mirror illumination, undulator 230eV circular canted mode

The size of the M2 mirrors was set to 380 mm long x 50 mm wide. The monochromator motion rotates M2 about a point 7.577 mm above the optical face of the grating. This changes the distance along the beamline that the center of the beam strikes the mirror from 31.66 m at 2.3 keV (88.73° from normal to beam) to 31.93 m at 183 eV (84.01° from normal to beam). This effective translation of the mirror relative to the beam helps determine the length requirement of the optic. Figures QQQ, and QQQ produced by Ruben Reininger show the expected spot on M2 with undistorted optics for the straight, canted configurations. Internally cooled silicon plane mirrors of this and figure slope error of 0.17 µrad rms are slightly pushing the current state of the art manufacturing capability of InSync. However, InSync is currently quoting 0.25 µrad rms and has produced somewhat better, without using profile coating. Addition of profile coating should allow achievement of the required figure with current technology.

Gr

Good:20000   σx: 1.1267 Avg:-0.013402
σy: 21.425 Avg:0.019428
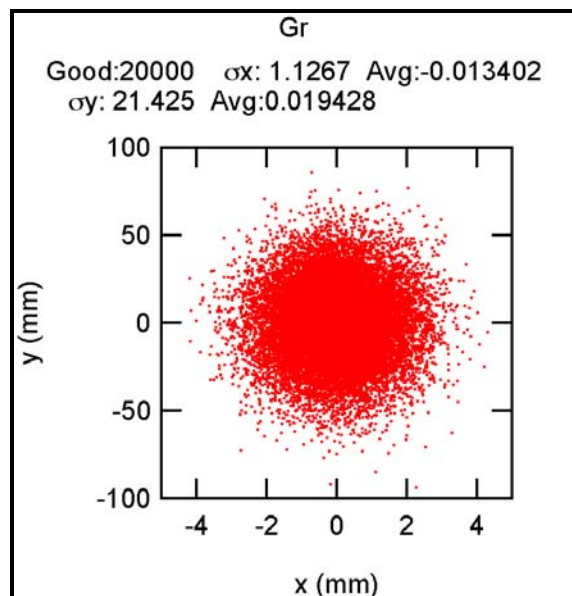
Figure 4.6. Grating illumination, undulator 183eV
linear straight mode

Grating

Good:20000   σx: 1.1388 Avg:-2.6777
σy: 27.31 Avg:0.019861
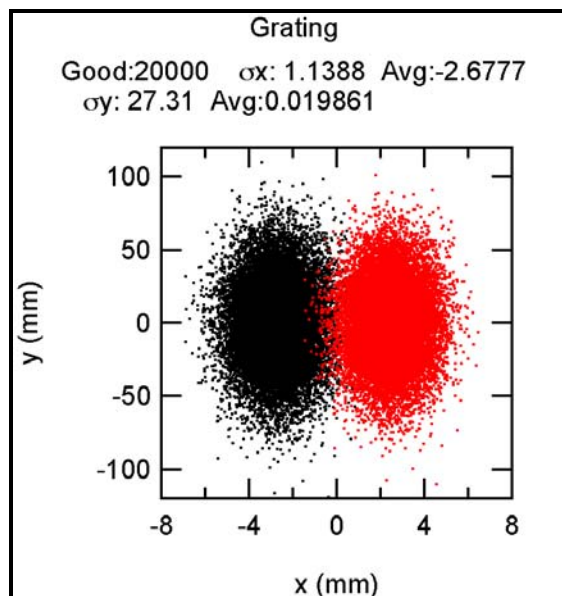
Figure 4.7. Grating illumination, undulator 230eV
circular canted mode

The size of the gratings was set to 130 mm long x 25 mm wide. This length is 5 σ from the expected spot size for canted beam operation at 230eV. The monochromator motion rotates the grating about the central face of the grating and can translate the grating support to place any of the three gratings into the beam. The gratings will be edge cooled silicon because the expected heat load is less than 40 W in the worst case with a power density of 0.016 W/mm^2. Figures QQQ, and QQQ produced by Ruben Reininger show the expected spot on the gratings with undistorted optics for the straight, canted configurations. These gratings are within standard manufacturing capability.

JenOptik makes a CPGM that is suitable for this beamline. The required resolution in angle is 0.03 µrad for the gratings and 0.05 µrad for the mirror. These requirements are better than the advertised capability of the JenOptik monochromator.

4.4.3.4   Chopper

The chopper is a mechanical device with a double function, block the non-desired radiation to come down to the end stations from the two canted insertion devices and provides with the switching frequency between the two different polarizations delivered by the EPU's selecting in time the beam from one of the two canted insertion devices serving this beamline. The chopper will also have a neutral position were x-rays from both insertion devices may pass without any being blocked. The preferred location of this piece of equipment will be between the monochromator and the branching mirror. It is desired that the switching frequency of the chopper could be selected from a few Hz up to several kHz. Having the possibility to select the different frequencies will allow choose a noise free frequency without interfering with noise from other frequencies. This can be achieved utilizing a rotating blade using ferrofluidic© style feedthroughs to connect with the driving motor and the switching control mechanism located outside of the vacuum chamber. A new design of an existing chopper located at the NSLS X13A beamline, is being improved. The X13A beamline requires a chopper because of the fast switching 22Hz characteristic of its unique source an Elliptically Polarizing Wiggler (EPW).

4.4.3.5   Exit Slit

The exit slits used by the Diamond I06 beamline were manufactured by Bestec. They would also be appropriate for this beamline. The power at the exit slits is expected to be less than 10 W with a power density less than 0.24 W/mm. According to Bestec this will not require cooled slits. The two exit slits are pretty close together on the branching line, but do fit without interference. The standard stands do interfere but can be easily modified. Pictures of the spot size at the exit slits for various conditions can be found in the reports from Ruben Reininger in Appendix A, SAS Optics Reports.

4.4.3.6   M3 and M4

The final focusing mirrors, M3 & M4 are Silicon Elliptical Bimorph mirrors. The same Hexapod mounting strategy is used for these as for M1 and the branching mirrors. The heat load at these mirrors is small so they do not require cooling. Correction for the thermal distortions of the M1 mirror and M2 mirror can be made respectively by changing the curvatures of M3 and the monochromator to recover the small spot size. Preliminary investigation suggests that this could be accomplished with a simple bending of the mirrors. The bimorph technology is exciting and would allow more complete correction at a small cost premium. This cost was included. For the canted beam case there needs to be three M3 mirrors just like there are three M1s. This will require additional in vacuum axis to get precision alignment of the mirrors as with M1. Each line has just one M4. The short branch M3s and M4 are 350 mm and 75 mm long respectively. The long branch M3s and M4 are 450 mm and 350 mm long respectively. The spacing between the long branch mirrors was increased to 1 m from the 0.75 m for the short branch. The tentative distance to sample spot from the M4 is 1 m for both lines. Pictures of the spot size on the final focusing mirrors for various conditions can be found in the reports from Ruben Reininger in Appendix A, SAS Optics Reports.

4.4.3.7   Diagnostics

Diagnostics are included for vacuum, beam current monitoring, beam position monitoring, temperature and flow sensing, and energy measurement. Vacuum RGAs and cold cathode gauges are discuss in the vacuum section. Costs were included to monitor the temperatures of all 25 cooled surfaces and the flow of the corresponding 14 coolant paths. Sensor signals would be conditioned and readout over a network to the central computer. This can provide a warning for temperatures going out of range and possibly be used as input into beamline operating setting. 4 fluorescent screens are anticipated to help locate the beam. These will be housed in the diagnostic chambers. Instrumented mesh will allow measurement of beam current upstream of the exit slits. Photo diode will monitor beam current after the exit slits. These will also be housed in the diagnostic chambers. The photo current on mirror surfaces, and beam defining slits will also be monitored. These devices will also report to the network either directly or through signal conditioners. A gas cell is included on each branch to allow energy calibration. The length of these was set to 0.5 m. A decision was made to use a Kimbal Physics Expanded Sphere for the diagnostic chambers, but there was not time to include this in the CAD model.

4.4.4   Endstations

The beamline has been designed to have two branches, each of which has the capability to host one or more independent endstations, depending on user demand. The angular separation between the two branches will be 2.5° and the two branches will be of unequal length, in order to provide adequate non-interfering floor space for endstations. This beamline will be able to host a wide variety of types of endstations, including diffractometers, spectrometers, and microscopes. The only restrictions on endstation types compatible with this beamline will be space and vacuum compatibility for windowless connection to the storage ring vacuum. A very important component of the beamline equipment protection system will be interlocks that

continuously monitor the end station vacuum pressure and temperature to avoid accidental venting of the storage ring. The endstation design and hardware will provide experimental capabilities (detectors, sample environments, and sample and detector motions) with enough degrees of freedom to permit users to carry out specific experiments using focused, high-resolution, high flux, coherent soft x-rays from the beamline. The endstation will also provide pinholes and/or specific coherent soft x-ray focusing optics (e.g. Fresnel zone plates) to perform experiments using the coherent part of the photon beam.

One example of an endstation well-matched to the capabilities of the CSX beamline is a multipurpose ultrahigh vacuum compatible four-circle diffractometer that will fully utilize the energy range, high photon flux, extraordinary brightness, and polarization control provided by the beamline. Conceptually, this endstation will emphasize scattering experiments, but at the same time will have the flexibility to introduce optical elements such as pinholes, Fresnel zone plates, and polarization analyzers, allowing one to conduct an wide range of experiments. The use of pinholes of different sizes in the chamber will enable coherent scattering and/or small angle scattering experiments to be performed, depending on the pinhole size. Combining polarization control of the soft x-rays incident on the sample with the capability to analyze the polarization of the soft x-rays reflected/emitted from the sample will provide an extremely powerful tool to study orbital and spin magnetic moments and molecular orientation in crystalline and partially ordered samples.

In more detail, a multipurpose endstation would consist of a high vacuum compatible vacuum vessel containing a basic four-circle in-vacuum diffractometer, two independent concentric circles dedicated to the detector and the sample rotations. The detector arm should be able to move a wide angular range exceeding 180 degrees. It is desirable that the incident beam on the sample and the beams detected by a number of detectors be unimpeded by any other instruments in the chamber over their full intended ranges of motion. The chamber should incorporate an electromagnet, using high T_c superconducting technology that will provide with homogeneous (1% in a distance +- 5 mm from the center of the magnet) magnetic fields up to 1 Tesla in x, y and z directions. This magnet will be able to rotate together with the sample keeping constant the direction of the magnetic field relative to the sample surface, or will be able to rotate independently of the movement of the sample, without disrupting in either case the incidence of the beam on the sample. The sample stage will be mounted on a cold finger that will cover a sample energy temperature range from 4K up to 300 K. Currently it is under study the possibility to raise the temperature of the samples above room temperature, but we are aware that this could cause the quench of the superconducting magnet. The chamber it self is conceive to have a sample transfer system that will allow to transfer samples when they are cool without breaking the vacuum, reducing the down time when samples get changed.

The design of the endstation and its vessel provides space for a motorized system of pinholes or refocusing optics in the front part of the chamber to allow the use of the coherent characteristics of the x-ray beam. The design of the detector arm includes space for the future a polarization analyzer. The vessel and its ports have been designed to allow the insertion of these two instruments during a maintenance period.

The endstation will also be provided with a pressure and temperature monitoring system connected to the beamline Equipment Protection System that will protect the beamline vacuum and instruments from possible errors in the operation of the end station that could lead to loss of vacuum.

4-A   Appendix A: SAS Optics Reports

Canted Beams for the Coherence Beamline.

August 23, 2007

Questions were raised about the required separation between the canted beams when the insertion devices are operated to deliver right and left circular polarized light. Since there is no horizontal focusing until the plane elliptical mirrors downstream the exit slit, the horizontal acceptance for the beams and the canting angle between them should be as small as possible. However, a too small canting angle is not desirable since the two polarizations will overlap.

Since only the first harmonic is emitted on axis when the ID is tuned to deliver circular polarized radiation, higher harmonics will be in the acceptance of the other ID. Furthermore, there could be some "at energy" flux emitted by one ID in the horizontal acceptance of the other ID.

To address these issues, we calculated the angular flux and angular power density over a wide horizontal angle when the upstream insertion device (ID) is tuned to emit circular polarized radiation. The calculations were performed with the SPECTRA code [1] at three photon energies. In the calculations we assumed that the ID center is 1.3 m upstream the center of the straight section. The machine parameters at this position are listed in Table 4.A.1. The parameters of the ID and photon energies are given in Table 4.A.2.

Figure 4.A.1Figure 4.A.2, and Figure 4.A.3 show the angular dependence of the flux density when the upstream ID is tuned to 231, 501, and 1008 eV, respectively. From these data, we obtained the integrated flux as a function of the horizontal aperture and full vertical aperture. As seen in Figure , a horizontal aperture of 0.16 mrad allows to collect practically the whole central cone flux at 501 and 1008 eV and most of this flux at 231 eV. The "at-energy" flux leaked in the acceptance window of the downstream ID was integrated from the data in Figure 4.A.1Figure 4.A.2, and Figure 4.A.3 assuming that the separation between the beams axis is equal to the acceptance angle. The leaked flux is plotted in Figure 4.A.5 for the three energies. Clearly, there is no optimal aperture for all energies. A reasonable compromise, which gives at most a 3% leak at the three energies, is a canting angle and an aperture of 0.16 mrad. A smaller leak percentage could be achieved with a canting angle of 0.2 mrad or larger and a (variable thickness) beam stop inserted in between the two beams. at high energies.

The angular power densities when the upstream ID is tuned to the three photon energies are shown in Figure ,4.A.6, Figure 4.A.7, and Figure 4.A.8. For an horizontal aperture and canting angle of 0.16 mrad the power obtained at 231 eV in the upstream ID aperture is 10.5 W and in the downstream ID aperture 22.7 W. At 501 (1008) eV the values are 45 (97) W for the upstream and 95 (71) W for the downstream.

References

1.   T. Tanaka and H. Kitamura, J. Synchrotron Rad., **8**, 1221, 2001

Tables

Table 4.A.1. Machine parameters used in the calculations. Upstream ID.

Energy (GeV)	3.0
Current (mA)	500
ε_x (pm rad)	550
ε_y (pm rad)	8
β_x (m)	2.61
β_y (m)	2.88
α_x (μrad)	0.914
α_y (μrad)	1.58

Table 4.A.2: ID parameters used in the calculations.

ID type		APPLE II	
Number of periods		44	
Period length (mm)		45	
Energy (eV)	230.6	501.3	1008
kx and ky	2.69	1.67	0.94

Figures
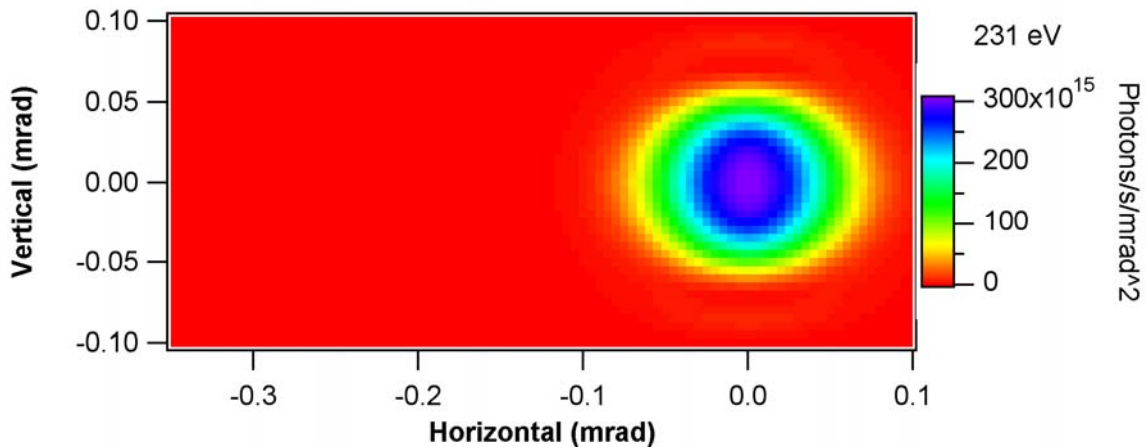
Figure 4.A.1. Angular flux density (in 0.1% BW) when the upstream ID is tuned to 231 eV.
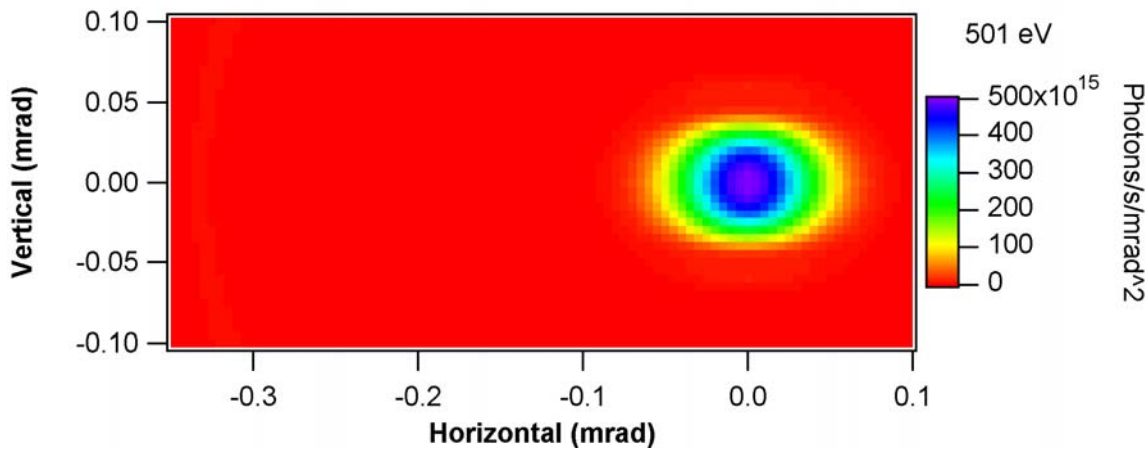
Figure 4.A.2. : As Figure 4.A.1 when the upstream ID is tuned to 501 eV.
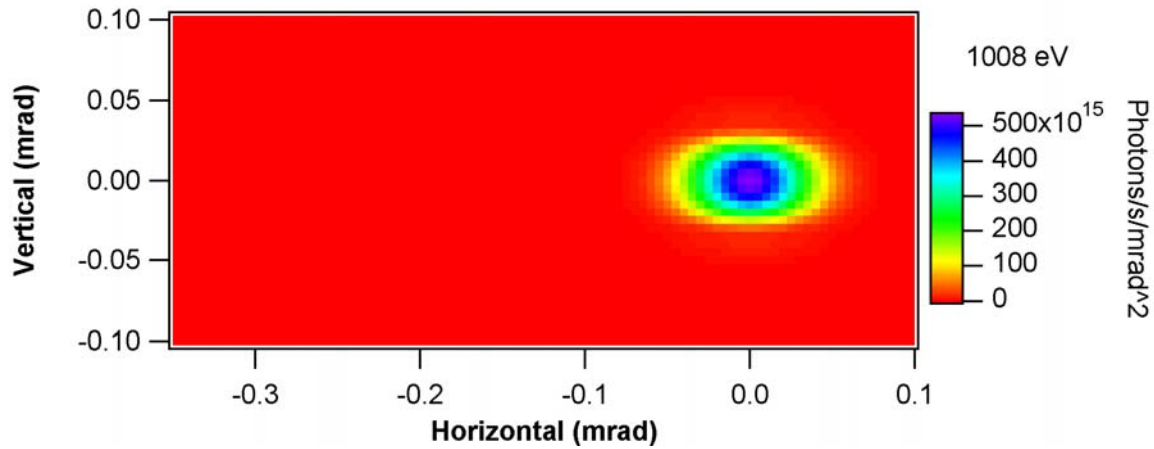
Figure4.A.3. As Figure 4.A.1 when the upstream ID is tuned to 1008 eV.
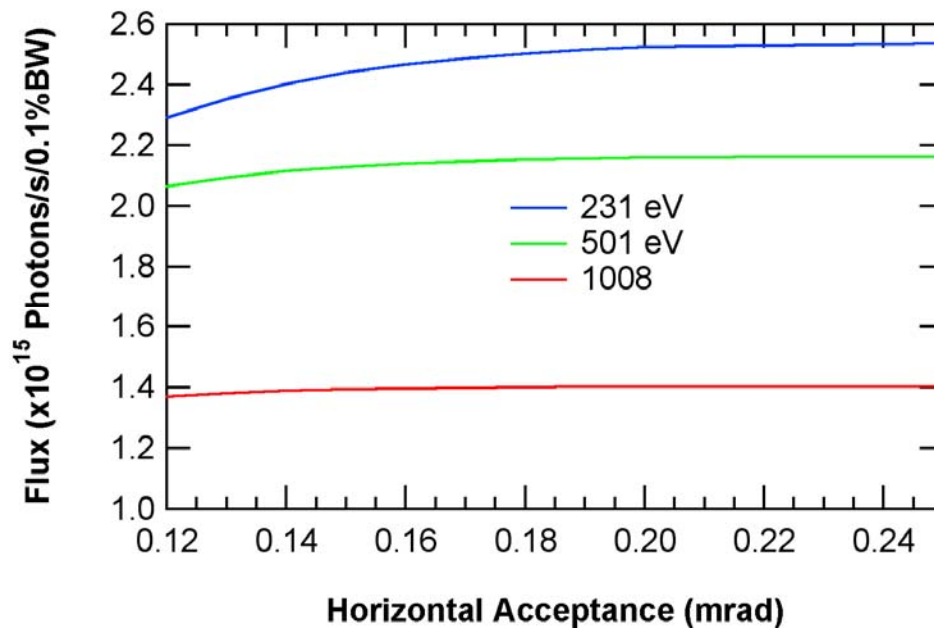
Figure 4.A.4. Flux as a function of the horizontal aperture (over full vertical aperture) for 231, 501, and 1008 eV.
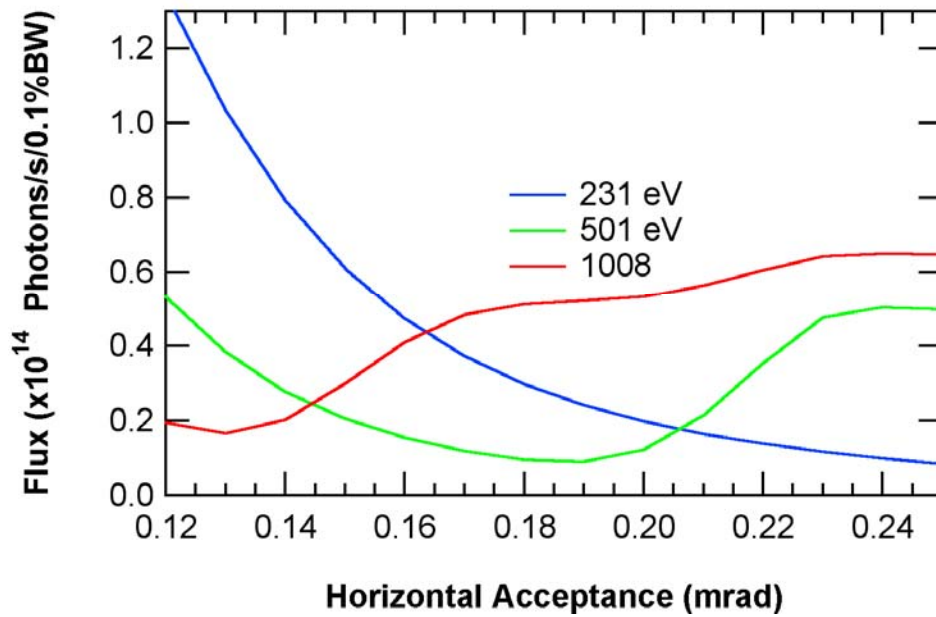
Figure 4.A.5. At–energy flux leaked onto the acceptance of the other ID as a function of the horizontal aperture (over full vertical aperture) for 231, 501, and 1008 eV. The canting angle is equal to the horizontal aperture.
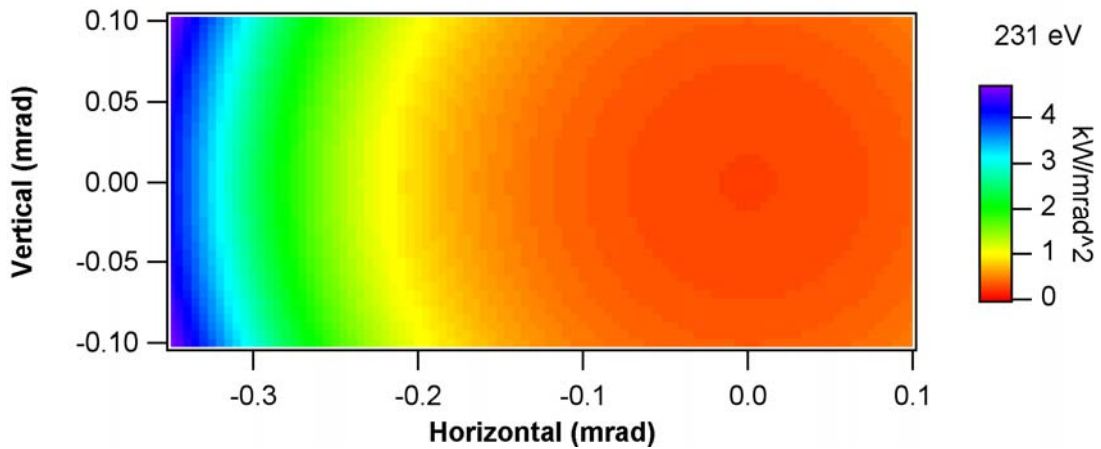
Figure 4.A.6. Angular power density when the upstream ID is tuned to 231 eV.
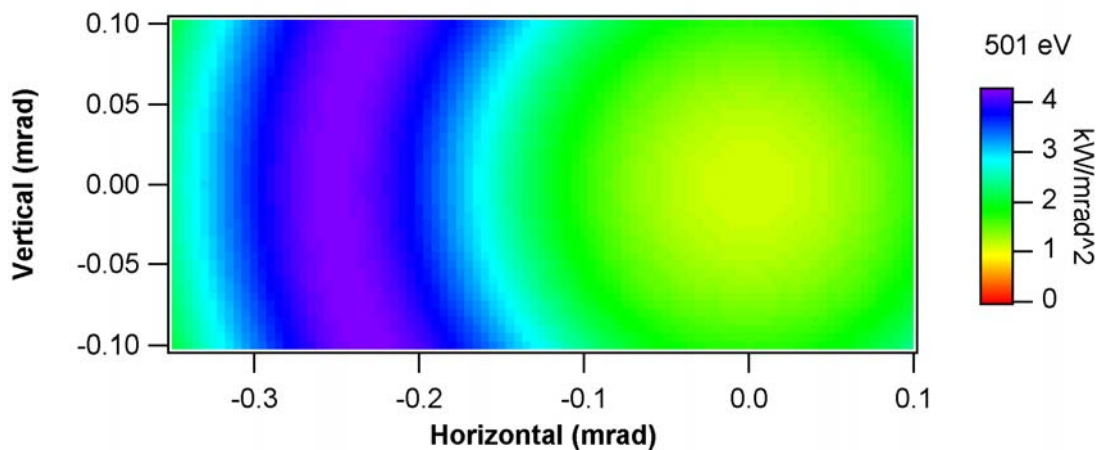
Figure 4.A.7. Angular power density when the upstream ID is tuned to 501 eV.
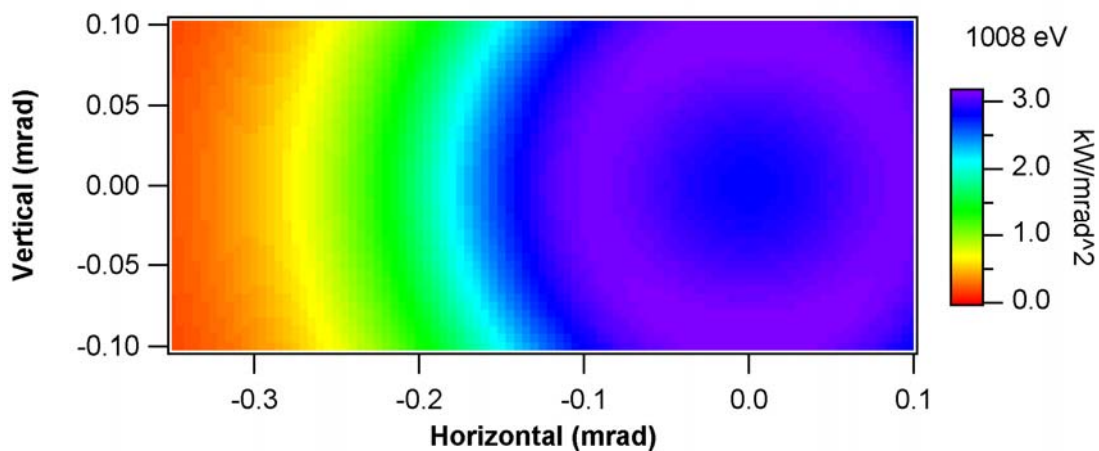
Figure 4.A.8. Angular power density when the upstream ID is tuned to 1008 eV.

4-A Appendix B: SAS Optics Reports

Preliminary Ray Tracings, Single Beam.

The purpose of this brief report is to give a first impression on the optical sizes and the size at the sample with the parameters we have discussed until now.

The machine parameters used are those at the straight center and are listed in Table 4.B.1. The parameters of the ID as well as the total source size and divergence calculated (as in our report dated July 16, 2006) at 183 eV are given in Table 4.B.2.

The distances from the source, angles of incidence, and deflection of the optical components are given in Table 4.B.3. M2 and the grating, a 150 l/mm VLS operating with c≈1.5, are tuned for 183 eV.

Figure 4.A.1, Figure 4.B.2, Figure 4.B.3, Figure 4.B.4, and Figure 4.B.5 show the illumination on M1, M2, grating, M3 and M4 with the above parameters. The ray tracings at the slit are shown in Figure 4.B.6. The spot at the sample when the slit width is set to 20 μm is seen in Figure 4.B.7. No slope errors have been assumed on the optical elements.

Tables

Table 4.B.1: Machine parameters used in the calculations.

Energy (GeV)	3.0
Current (mA)	500
σx (μm)	28
σy (μm)	2.6
σx' (μrad)	19.7
σy' (μrad)	3.1

Table 3.B.2: ID parameters used in the calculations.

ID type	APPLE II
Number of periods	85
Period length (mm)	45
Energy (eV)	183
Σx (μm)	46.4
Σy (μm)	37.2
Σx' (μrad)	35.1
Σy' (μrad)	29.2

Table 4.B.3: Distance from the source, angle of incidence, and deflection of the optical components. (183 eV, LEG)

Element	Distance (mm)	Angle (deg)	Deflection
M1- Sagittal Cylinder	29500	88.75	horizontal
M2- Plane	31851.8	87.11	vertical
Gr - Grating	32000	87.69 (inc.)	vertical
Slit	42000		
M3 - Plane Elliptical	43200	88.5	horizontal
M4 – Plane Elliptical	43950	88.5	vertical
Sample	44950		

Figures

M1

Good:20000   σx: 0.86439 Avg:-0.00082184
σy: 47.617 Avg:-0.47637
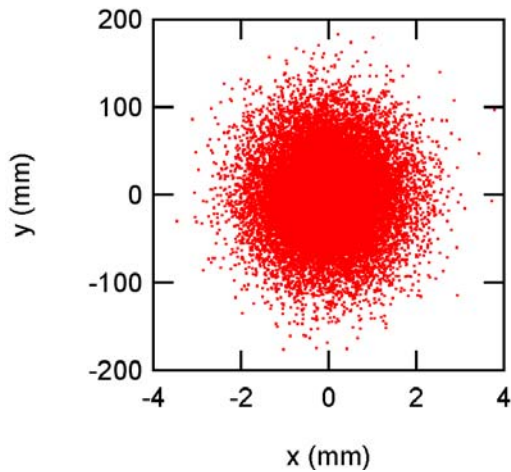
Figure 4.B.1. M1 illumination

M2

Good:20000   σx: 1.1215 Avg:0.013339
σy: 17.145 Avg:0.015596
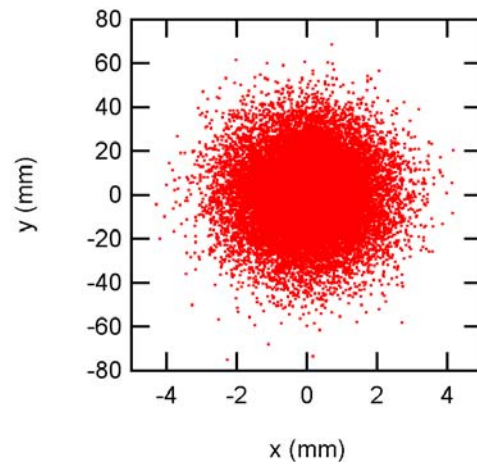
Figure 4.B.2. M2 illumination

Gr

Good:20000   σx: 1.1267 Avg:-0.013402
σy: 21.425 Avg:0.019428
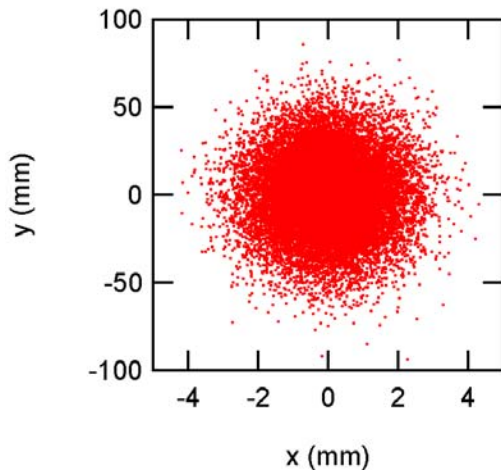
Figure 4.B.3. Grating illumination

M3

Good:15134   σx: 0.15597 Avg:0.00071034
σy: 69.421 Avg:-0.23242
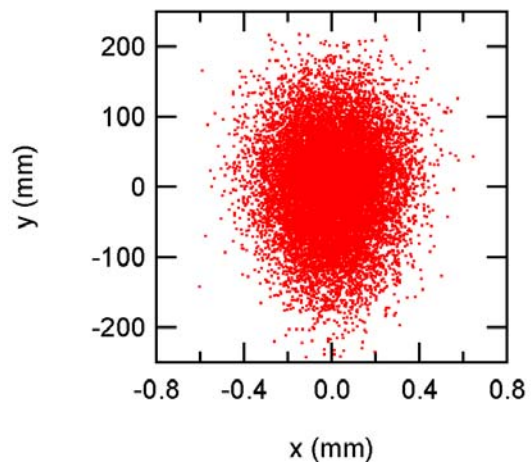
Figure. 4.B.4. M3 illumination

M4

Good:15134   σx: 0.86722 Avg:-0.022557
σy: 11.589 Avg:-0.019085

Slit

Good:20000   σx: 1.4784 Avg:-0.017567
σy: 0.00846 Avg:0.0014756
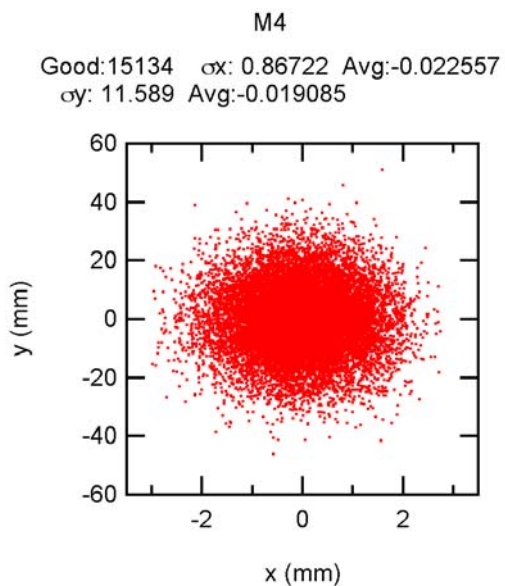
Figure 4.B.5. M4 Illumination

Figure 4.B.6. Image at slit

Sample 20 µm slit

Good:15134   σx: 0.0018844 Avg:-1.4188e-05
σy: 0.0026883 Avg:-0.00026337
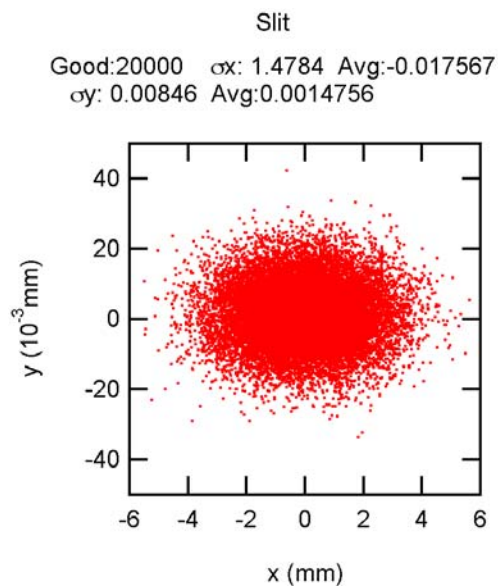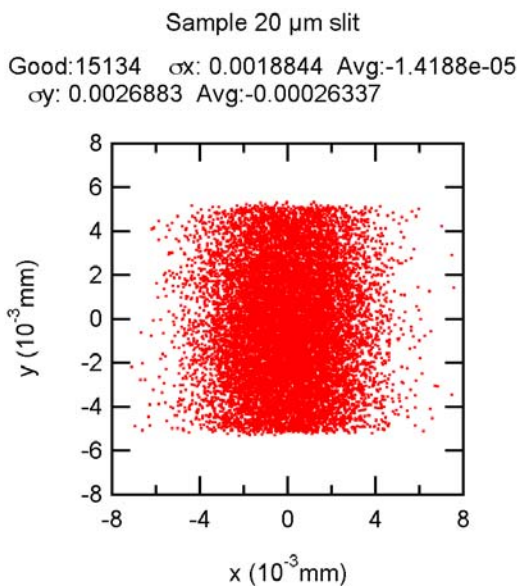
Figure 4.B.7. Image at sample position.

4-A   Appendix C: SAS Optics Reports

Slope Errors on the Optical Elements.

The meridional slope errors on M1, diverting mirror, and M3 contribute to the horizontal spot size. The sagittal slope errors on M2, grating, and M4 also affect the horizontal spot size. The required slope errors were obtained from the condition that each contribution is less or equal half the minimum RMS horizontal spot size at the sample.

The meridional slope errors on M2 and the grating contribute to the resolution. The sagittal slope errors on M1 and diverting mirror also affect the resolution. The required slope errors were obtained from the condition that each contribution is less or equal half the combined resolution due to the source and a 10 µm exit slit.
The meridional slope error on M4 and the sagittal errors on M3 contribute to the vertical spot size at the sample. The required slope errors were obtained from the condition that each contribution is less or equal half the minimum RMS vertical spot size at the sample with a 10 µm slit.

The required RMS slope errors (and the condition determining it) are given in the table below.

Table 1. Maximum RMS slope errors on the optical elements

Element	Meridional(µrad)	Condition	Sagittal(µrad)	Condition
M1- Sagittal cylinder	0.25	Hor. spot size	8.0	Resolution
M2- Plane	0.17	Resolution	3.5	Hor. Spot Size
Gr - Grating	0.13	Resolution	5.5	Hor. Spot Size
Div. Mirror – Plane	0.22	Hor. Spot Size	8.8	Resolution
M3 - Plane Elliptical	0.17	Hor. Spot Size	14	Ver. Spot Size
M4 – Plane Elliptical	0.37	Ver. Spot Size	14	Hor. Spot Size

4-A   Appendix D: SAS Optics Reports

Position of the Optical Elements, Optics Parameters, and Ray Tracings

with Canted Beams

Position of the Optical Elements

The coordinates of the optical elements in the case of a single beam are given in Table 4.D.1. The center of the coordinate system is in the middle of the straight. The y coordinate is along the beam propagation, x is in the horizontal plane and perpendicular to y, and z is along the vertical. The distance between M3 II and M4 II was increased to 1 m.

Table 4: Coordinates of the optical elements.

Element	x (mm)	y (mm)	z (mm)
Source	0.000	0.000	0.000
M1	0.000	29500.000	0.000
M2	-102.583	31849.537	0.000
Grating	-109.0485	31997.621	-15.000
Slit	-545.242	41988.103	-15.000
M3	-597.586	43186.961	-15.000
M4	-662.952	43934.107	-15.000
Sample	-750.025	44929.353	28.619
Branching Mirror	-196.287	33995.717	-15.000
Slit II	-893.533	41965.275	-15.000
M3 II	-1695.366	51130.266	-15.000
M4 II	-1825.892	52121.711	-15.000
Sample II	-1956.294	53112.212	28.6193

Optical parameters

Table 2. Parameters of the optical components.

Element	Figure	Major axis (mm)	Minor axis/sagittal radius (mm)
M1 Center	Meridional Cylinder		1287.08
M1 Upstream	Meridional Cylinder		1338.89
M1 Downstream	Meridional Cylinder		1234.89
M3 Center	Meridional Elliptical Cylinder	22475.	189.68
M3 Upstream	Meridional Elliptical Cylinder	23125.	192.51
M3 Downstream	Meridional Elliptical Cylinder	21825.	186.80
M4	Meridional Elliptical Cylinder	1475.	30.463
M3 II Center	Meridional Elliptical Cylinder	26600.	220.75
M3 II Upstream	Meridional Elliptical Cylinder	27250.	223.54
M3 II Downstream	Meridional Elliptical Cylinder	25950.	217.93
M4 II	Meridional Elliptical Cylinder	5600.	69.67

Grating Parameters

The line density of the gratings is given by $k(w) = a_0 + a_1 w + a_2 w^2 + \ldots$ where w is positive towards the slit. These parameters and the c parameter are listed in Table 3.

Table 3. Grating parameters

Grating	a_0 (mm^{-1})	a_1 (mm^{-2})	a_2 (10^{-6} mm^{-3})	c parameter
LEG	150	0.05397	8.09	≈1.5
MEG	400	0.14381	21.5	≈1.5
HEG	1200	0.30181	45.1	≈2.2

Accuracy in Optics Positioning.

The resolution of the hexapods is 1µm for the translations and 1 µrad for the rotations[1]. These values are sufficient for most of the required movements besides the pitches of M1, the branching mirror, M3 and M4. Since the goal is to overlap the beams from the two IDS, lets say within 0.2 the sigma value, one needs a resolution better than 0.07 µrad on the most sensitive element, M3. We note that this resolution is 2/5 the meridional slope error specified previously for M3.

Ray Traces with Canted Beams

As in the case of the IDs emitting linearly polarized light[2], we determined the source sizes as a function of the longitudinal position using SRW. In this case, the upstream ID (located at 1.3m upstream the center of the straight) was tuned to emit circular polarized radiation at the lowest possible energy (230 eV). As seen in Figure 2, the RMS vertical size is 26 µm and it is located very close to the ID center. The vertical RMS size is 42 µm and occurs close to the ID end. The lines in the right part of the figure are linear fits to the RMS size giving RMS divergences of 32 µrad for the vertical and 34 µrad for the horizontal. In the ray tracings described below, we used these divergences and vertical RMS sizes. For the horizontal RMS size, we used the RMS beam size at the center of the ID, i.e., 45 µm.

In the canted mirrors, y=0 corresponds to the coordinates of the mirror collecting the central beam.
Figure and Figure show the illumination of the M1 mirrors collimating the upstream and downstream beams, respectively.

Figure , Figure , and Figure show the illumination of the plane mirror, the grating, and the slit plane with both beams when using the 150 l/mm grating and c=1.5. Note that the upstream beam is wider (diverging beam) but the vertical image at the slit is smaller for the upstream beam due to the larger demagnification.
The illumination of M3 with the upstream beam is seen in Figure and with the downstream beam in Figure 9. Note that due to the mirror orientation in Shadow, the y coordinates have the opposite sign. The illumination of M4 with both beams is presented in Figure 10.
The spot at the sample position with the upstream beam is displayed in Figure 11 and that of the downstream beam in Figure 12. Note that the image of the downstream beam is narrower due to the higher

---

[1] According to Ken Kriesel.
[2] Report "ID's Source Positions" dated September 9, 2007. The same electron beam parameters were used.

demagnification. This can be corrected by detuning the plane elliptical mirror as done in the initial beamline design.

The illumination of the mirrors of the branch line are shown in **Figure 13** (diverting mirror), **Figure 14** (M3 II upstream ID), **Figure 15** (M3 II downstream beam), and **Figure 16** (M4 II). The sample illumination with both beams is seen in **Figure 17** and **Figure 18**.

Figures
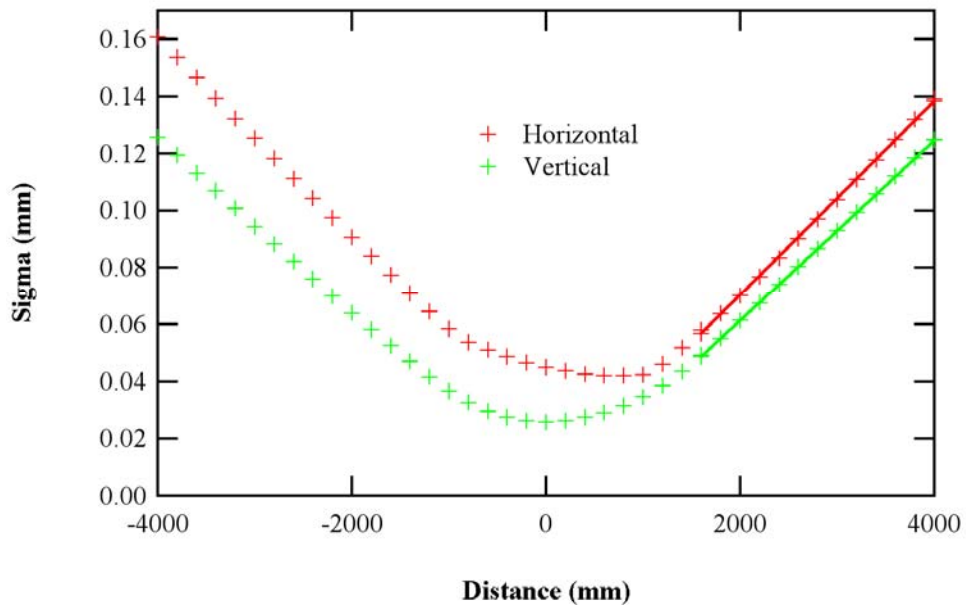
Figure 2. RMS image size of the upstream ID radiation as a function of the longitudinal position. The photon energy is 230 eV and the straight center is at +1.3 m.
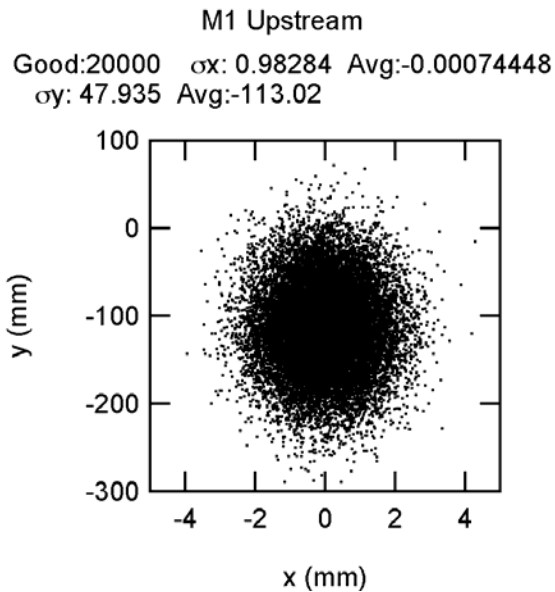
Figure 3. M1 illumination. Upstream ID.
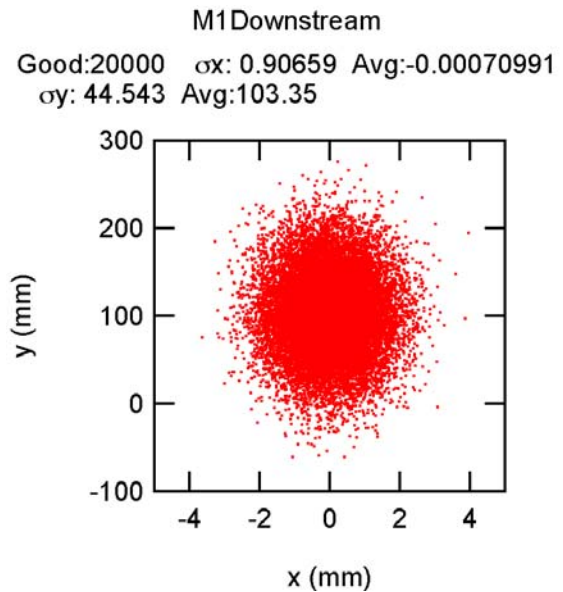
Figure 4. M1 illumination. Downstream ID.

M2

Good:20000   σx: 1.1331 Avg:2.6643
σy: 21.853 Avg:0.015947
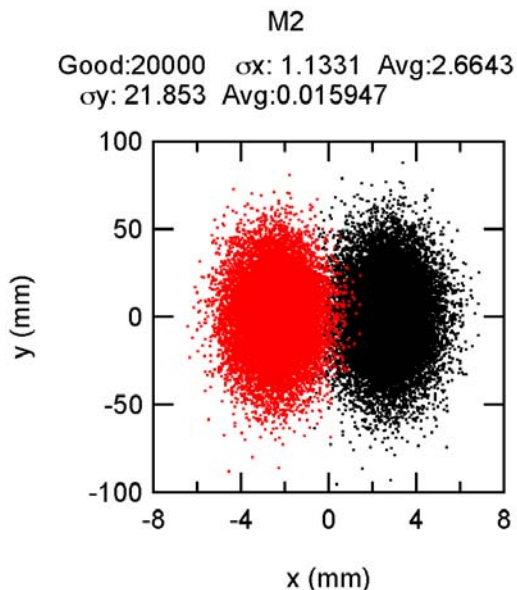
Figure 5. M2 illumination. Black: Upstream ID, Red: Downstream ID.

Grating

Good:20000   σx: 1.1388 Avg:-2.6777
σy: 27.31 Avg:0.019861
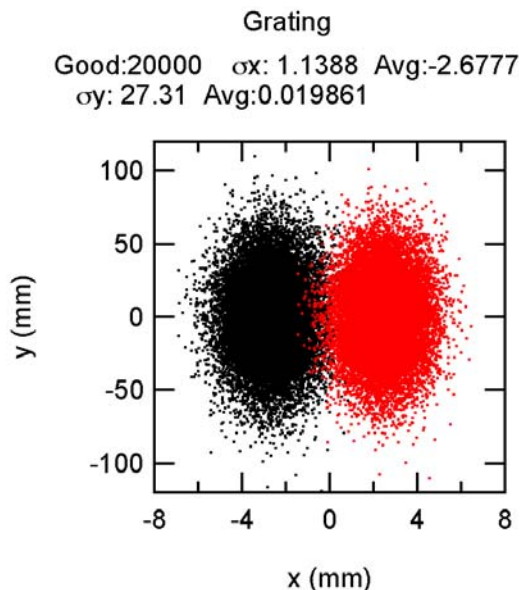
Figure 6. Grating illumination. Black: Upstream ID, Red: Downstream ID.

Slit plane

Good:20000   σx: 1.4804 Avg:-3.4818
σy: 0.00573 0.00615 Avg:0.00030836
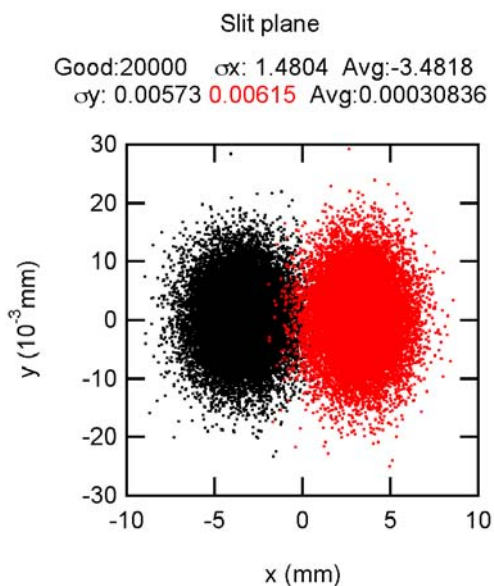
Figure 7. Slit plane. Black: Upstream ID, Red: Downstream ID.

M3 Upstream

Good:20000   σx: 0.20169 Avg:0.0010866
σy: 66.822 Avg:159.99
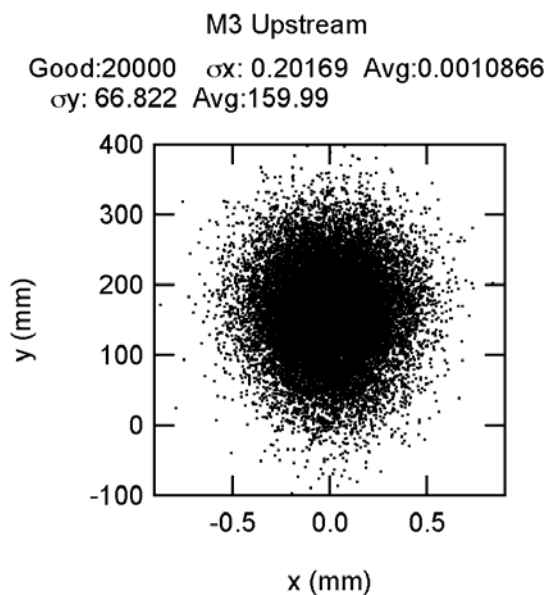
Figure 8. M3 illumination. Upstream ID.

M3 Downstream

Good:20000   σx: 0.14168   Avg:0.0008594
σy: 68.144   Avg:-156.29

M4

Good:20000   σx: 0.96269   Avg:2.1701
σy: 13.224   Avg:0.085581
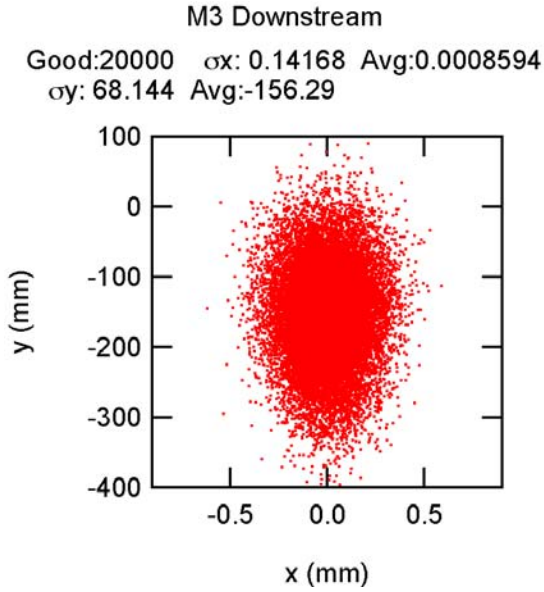
Figure 9. M3 illumination.
Downstream ID.
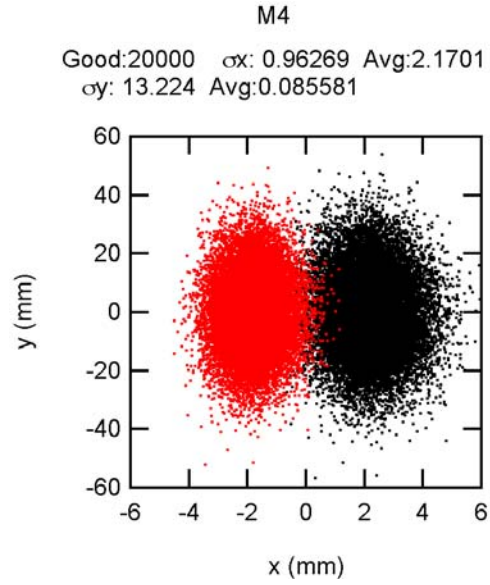
Figure 10. M4 illumination.
Black: Upstream ID, Red: Downstream ID.

Sample Upstream

Good:15562   σx: 0.001626   Avg:1.4949e-05
σy: 0.0023946   Avg:6.6055e-05

Sample Downstream

Good:16085   σx: 0.0020494   Avg:-4.6097e-06
σy: 0.002479   Avg:7.996e-05
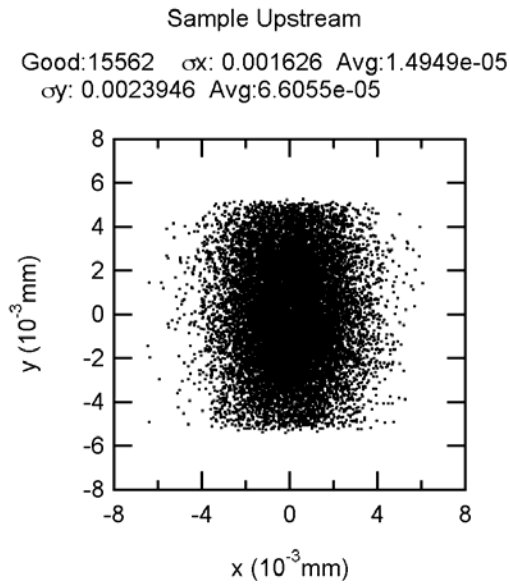
Figure 11. Sample illumination.
Upstream ID.
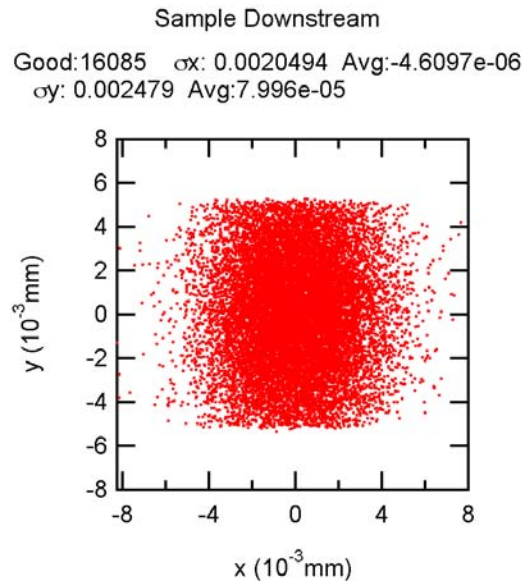
Figure 12. Sample illumination.
Downstream ID.

Div. Mirror

Good:20000   σx: 1.1592 Avg:-0.0039031
σy: 55.745 Avg:130.69
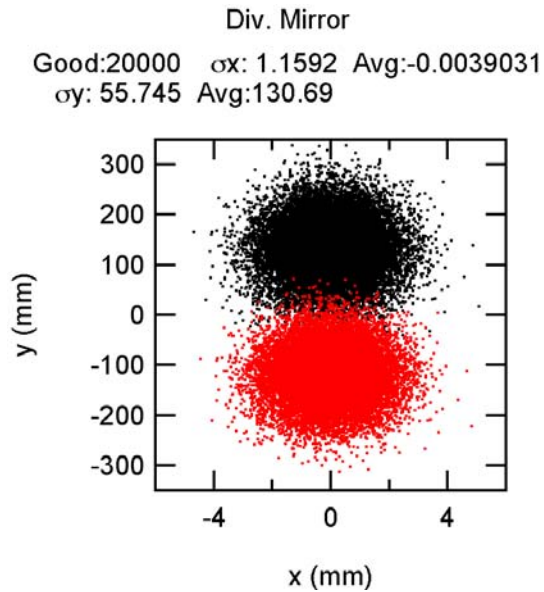
Figure 13. Illumination of the diverting mirror.
Black: Upstream ID, Red: Downstream ID.

M3 II Upstream

Good:20000   σx: 1.3281 Avg:0.0051097
σy: 85.754 Avg:-198.36
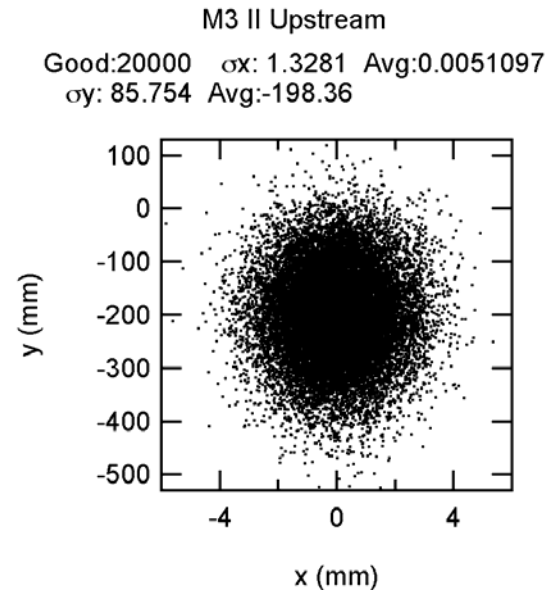
Figure 14. M3 II illumination.
Upstream ID.

M3 II Downstream

Good:20000   σx: 1.2742 Avg:0.0047459
σy: 75.034 Avg:177.7
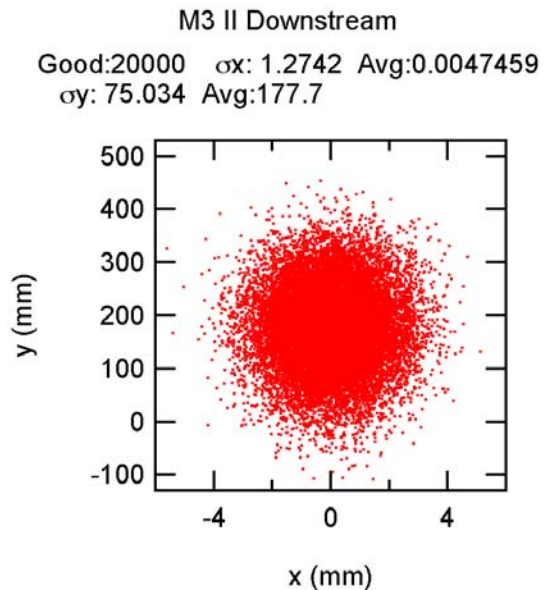
Figure 15. M3 II illumination.
Downstream ID.

M4 II

Good:20000   σx: 0.82755 Avg:-1.9947
σy: 68.919 Avg:-0.57335
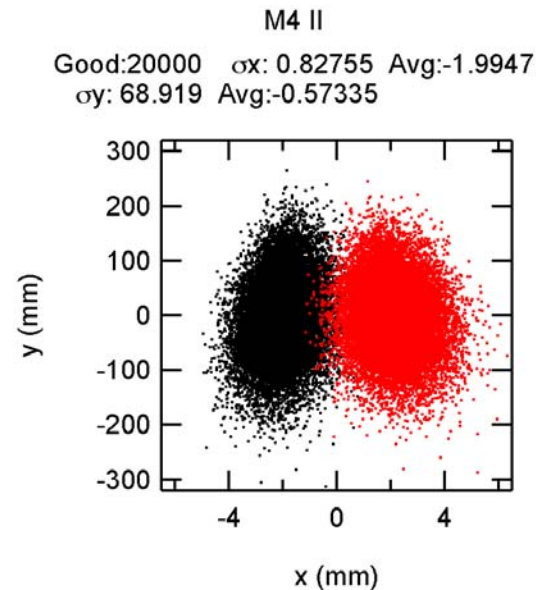
Figure 16. M4 II illumination.
Black: Upstream ID, Red: Downstream ID.

Sample Upstream

Good:15562 σx: 0.0018763 Avg:-1.5795e-05
σy: 0.00045984 Avg:9.0743e-06
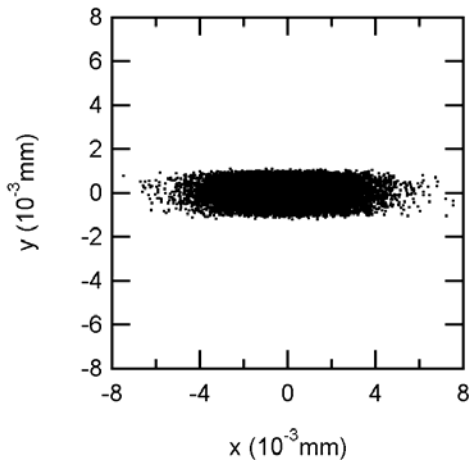
Figure 17. Sample II illumination.
Upstream ID.

Sample Downstream

Good:17943 σx: 0.0016431 Avg:3.3949e-06
σy: 0.00047404 Avg:1.7407e-05
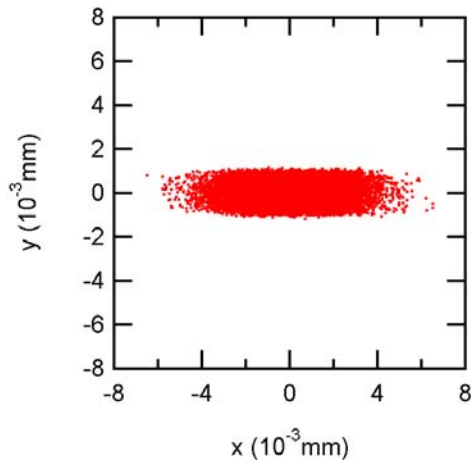
Figure 18. Sample II illumination.
Downstream ID.

Power Absorbed by Optical Elements.

Corrected for the values used by Ken Kriesel on the FEA.

NOTE: Ken Kriesel corrected the illuminated length he used in the FEA of M2 in section 2 from (what I wrote) 80 mm to 68 mm. I calculated the total power on M1, M2 and the grating, for an aperture of 8×8 mm^2 at the position of M1. I added to the table (in parenthesis) the power values for the aperture used by Ken, i.e., 7.1×5.15 mm^2 at the position of M1. The effect of the reduced horizontal aperture on the slope errors along the horizontal direction needs to be investigated.

Power Absorbed by the Optical Elements

The power and power densities absorbed by M1, M2, and the grating were calculated with the IDPower routine in SRCalc with the machine and ID parameters listed in our report dated August 27, 2007. We assumed Au as the reflective coating on all optics. Table 7 summarizes the maximum power values for elements up to the slit.

The highest absorbed power and power density in M1 and M2 occur when the two IDs are operated in tandem and tuned to the lowest photon energy, 183 eV. The worst case for M2 is when it is used with the high energy grating (HEG) since its angle of incidence is the smallest, 84.0º. As described in section 2, the power incident along the length of M2 needs to extend beyond the central cone of the "good" radiation to minimize the meridional slope error. Therefore, the horizontal and vertical apertures at the position of M1 were set to 8×8 mm^2. The power densities absorbed by M1 and M2 are shown in Figure 2 and Figure 20. The total absorbed power in M1 is 1.9 kW and in M2 236 W. The maximum power densities in M1 and M2 are 0.92 and 0.36 W/mm^2, respectively.

The maximum power density on the gratings (obtained from a few cases at different energies using the LEG) is less than 16 mW/mm^2. This value was obtained with the ID tuned to 555 eV (Figure 21). The total power absorbed with the aperture mentioned above is almost 40W. The horizontal aperture could be reduced to half, which will decrease the total power to 20 W. However, this could have a negative effect on the figure of M1, which will impair the horizontal spot at the sample.

The grating efficiencies and the diffraction angles are required to obtain the power densities and power downstream the grating. Since we already calculated the monochromatic flux for this beamline with a slightly different ID (42 mm period instead of 45 mm) we used those results to estimate an upper limit for the power and power densities on those elements.

The calculated flux at the sample at 1 keV with the LEG and 10 µm slit is 5×10^{13} photons/sec, or a power of 8 mW. With an aperture of 4×4 mm^2 at the position of M1, the illuminated vertical (horizontal) size at the slit with this grating is approximately 7.2 (5.7) mm. This means that the power at the slit plane is less than 10 W and the power density is less than 0.24 W/mm^2. Approximately the same power will be incident on the diverting mirror but the absorbed power and absorbed power densities are less than 3 W and less than 4 mW/mm^2.

With a 10µm slit, the power absorbed in M3 and M4 is less than 2 mW. The total power will increase linearly with the slit width. The power densities are negligible.

The power on the chopper in the CP fast switching mode is less than 10 W and the power density is less than 0.2 W/mm^2.

Slope Errors on M2

Ken Kriesel did a FEA analysis to obtain the temperature rise and surface deformation due to the power absorbed in M2. He initially performed[3] the calculations assuming a homogeneous power density of 0.362 W/mm^2 over a length of 48 mm and a width of 5.4 mm. Ken included in the model the fact that that beam is not centered on M2 but at 307 mm from its end.

We ray traced the system up to the exit slit with the deformed surface obtained by Ken and realized that the RMS spot at the exit slit increased from 5.8 μm to more than 11 μm. The reason for the large increase is mainly due to the sharp discontinuity in the absorbed power along the mirror length, giving a large slope error in the region of the central cone.

At our request, Ken increased the length over which the power is absorbed to 68 mm. The surface deformation he obtained (assuming a constant power density instead of the small variations seen in Figure 20) is displayed as an image plot in Figure 22. From these results we extracted the surface deformation along the mirror length (at zero width) and along the mirror width (at zero length). The height profiles and the calculated slope errors are shown in Figure 23 and Figure 24.

The maximum surface deformation is actually not at the center of the beam, i.e. at 307 mm (Figure 23). As Ken pointed out, this is due to the fact that the long M2 mirror is not illuminated at the center[4]. The sharp increase in the slope error towards the edge of the region being heated by the beam is clearly seen in Figure 23. However, the beam in the central cone sees only an RMS slope error of ≈0.9 μrad and not the high slope error region.

Ray Traces with Deformed M2

The spot at the exit slit plane when the ID is tuned to 183 eV, the high energy grating is used, and there are no deformations on the optics, is shown in Figure 25. The effects of the induced figure error on M2 due to the absorbed power are evident when comparing Figure 26 to the previous one.
The figure change in the central part of M2 can be approximated by a convex radius of ≈1.8×10^7 mm, which means the beam incident on the grating is not vertically collimated as in the optical design. This change in the virtual source position can be corrected by operating the grating with a c value of 2.193 instead of the nominal value of 2.184 at this energy. The spot at the exit slit plane with the deformed M2 and the corrected c value is presented in Figure 27. The vertical RMS size is reduced to 6 μm, very close to the initial value.

The above example shows the possibility of correcting the spot size at the slit for the highest absorbed power in M2. At this energy (183 eV) the beam size is the largest. Further studies at higher energies (where the beam is smaller) need to be performed to verify that this "correction" is also possible. Still to be tested is whether the deformations along the meridional direction on M1 can be corrected with a change in the curvature of M3. FEA of this mirror are then required.

---

[3] I proposed that length since it is the part illuminated by the central cone.
[4] Ken Kriesel checked that illuminating the mirror center gives a symmetric deformation.

Effect of Single M1

We discussed the option of performing the fast switching of CP with the electron beam instead of canting the beams. This requires using a single collimating mirror. To assess the effect of using a single M1, we have ray traced the system when each ID has an M1 with the correct sagittal radius and when the radius is the one required when the two IDs are operated in tandem.

The ray tracings at the exit slit plane when the upstream ID is tuned to 230 eV, M1 has the correct sagittal radius, and the LEG is used, are seen in Figure 28. Changing the radius to that required for the case when the IDs are operated in tandem increases the vertical spot by almost a factor of two (Figure 29). This means that the contribution to the resolution due to the source will degrade by the same factor. Practically the same results are obtained for the downstream ID.

Table 5. Maximum power and power densities absorbed by the optical elements. Values in parentheses are for an aperture of 7.1×5.15 mm^2 at the position of M1.

Element	Power Absorbed (W)	Power Dens. Abs (W/mm^2)	Case
M1	1910 (1160)	0.92	183 eV
M2	236 (132)	0.37	183 eV HEG
Gr	40 (22)	0.016	555 eV LEG
Div. mirror	<3	<0.004	1 keV LEG
Chopper	<10	<0.2	1 keV CP LEG
Slit	<10	<0.24	1 keV LEG

Figures
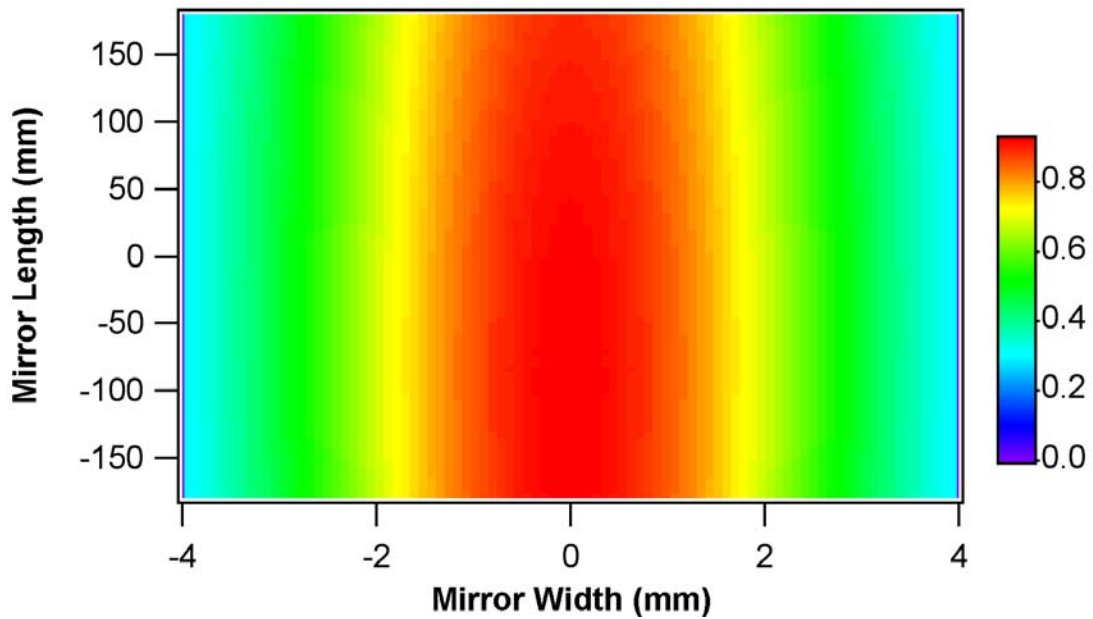
Figure 19. Power density (W/mm^2) absorbed in M1. 183 eV.
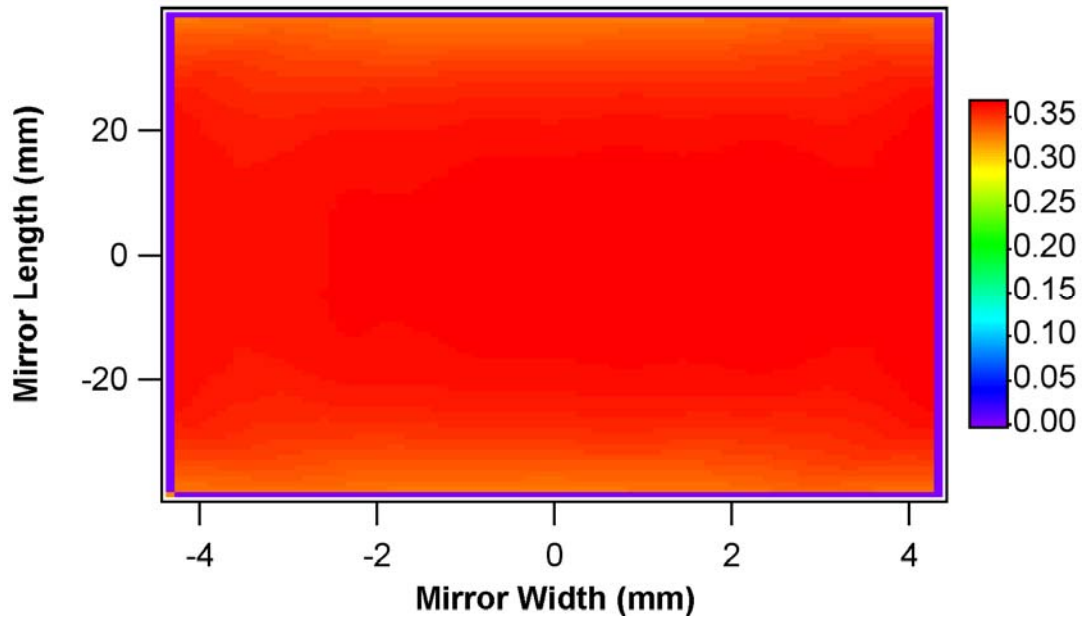
Figure 20. Power density (W/mm^2) absorbed in M2. 183 eV HEG.
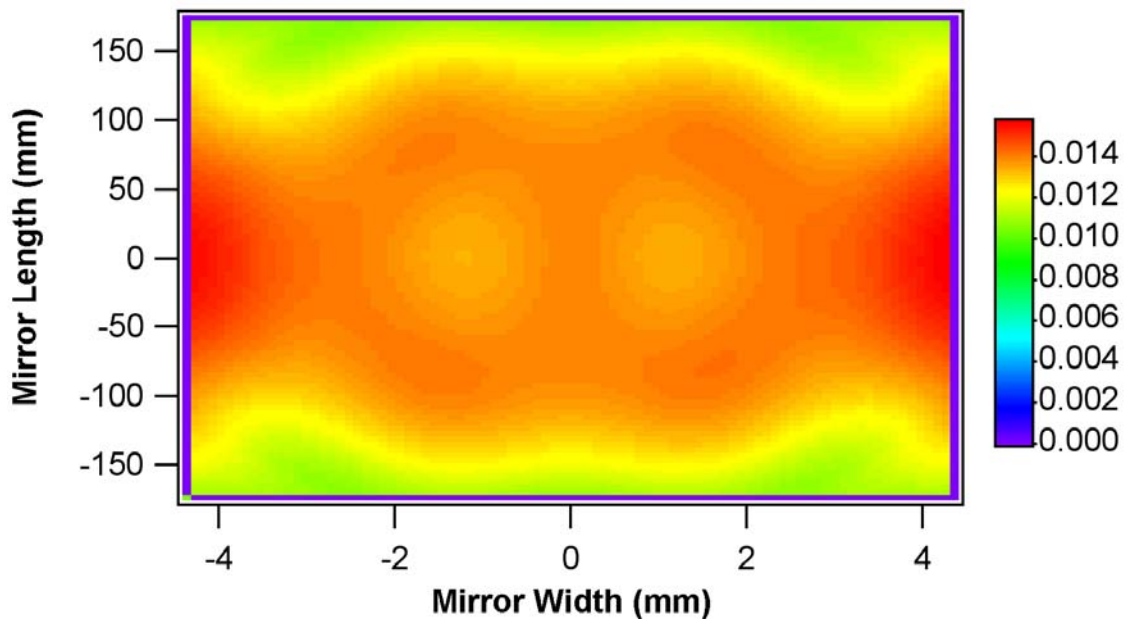
Figure 21. Power density (W/mm^2) absorbed in the LEG at 555 eV.
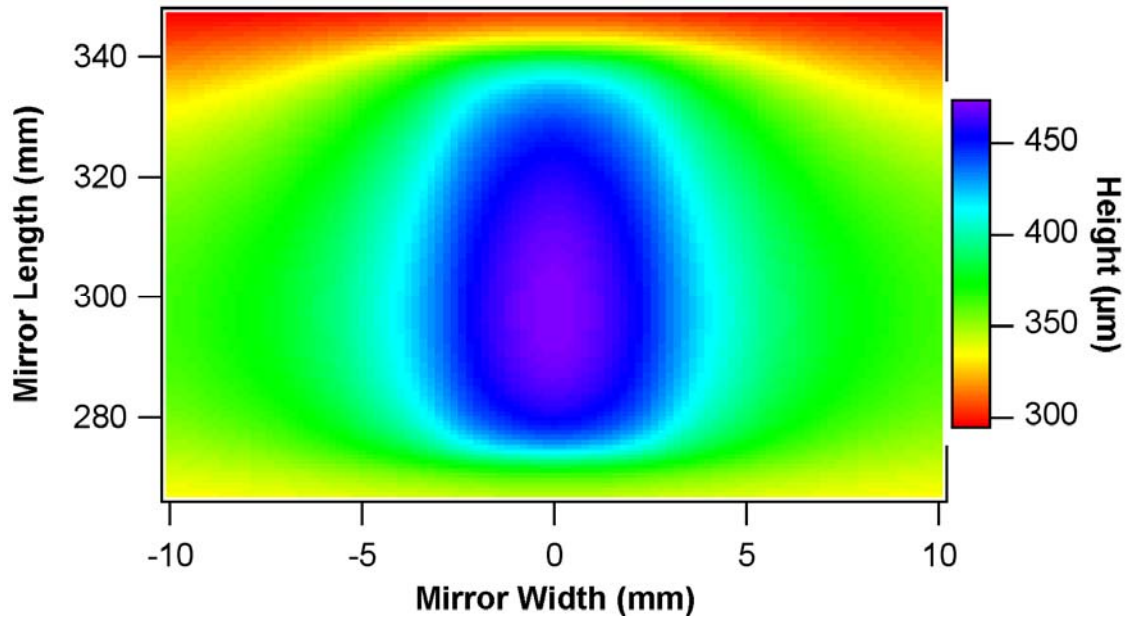
Figure 22. Height change on M2 due to the absorbed power density.
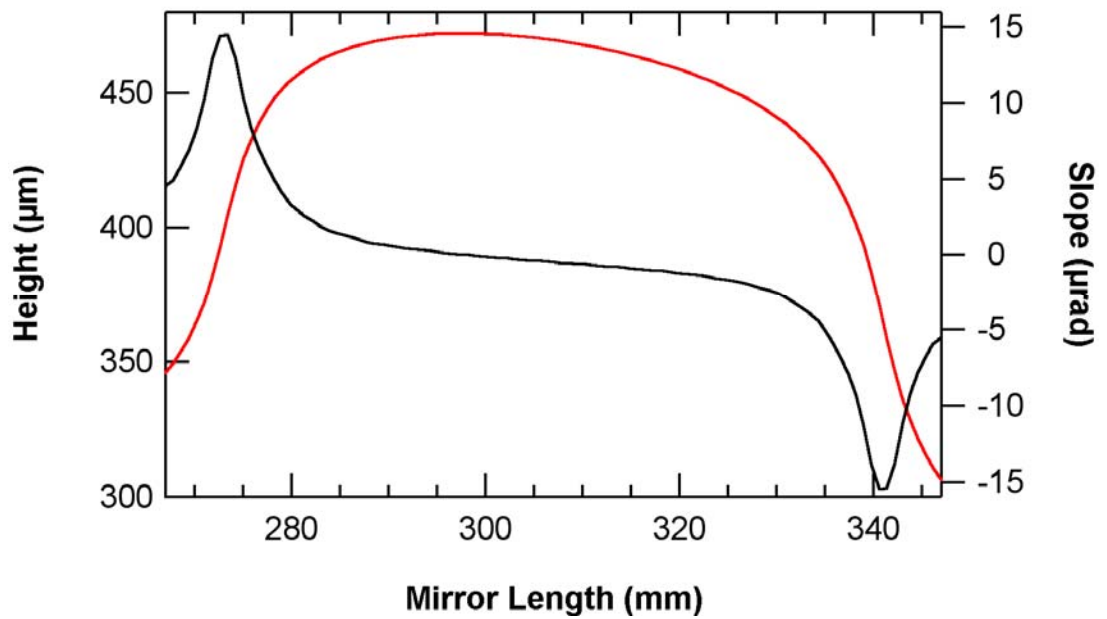
Figure 23. M2 Surface deformation (red trace) and meridional slope error (black trace) at zero width.
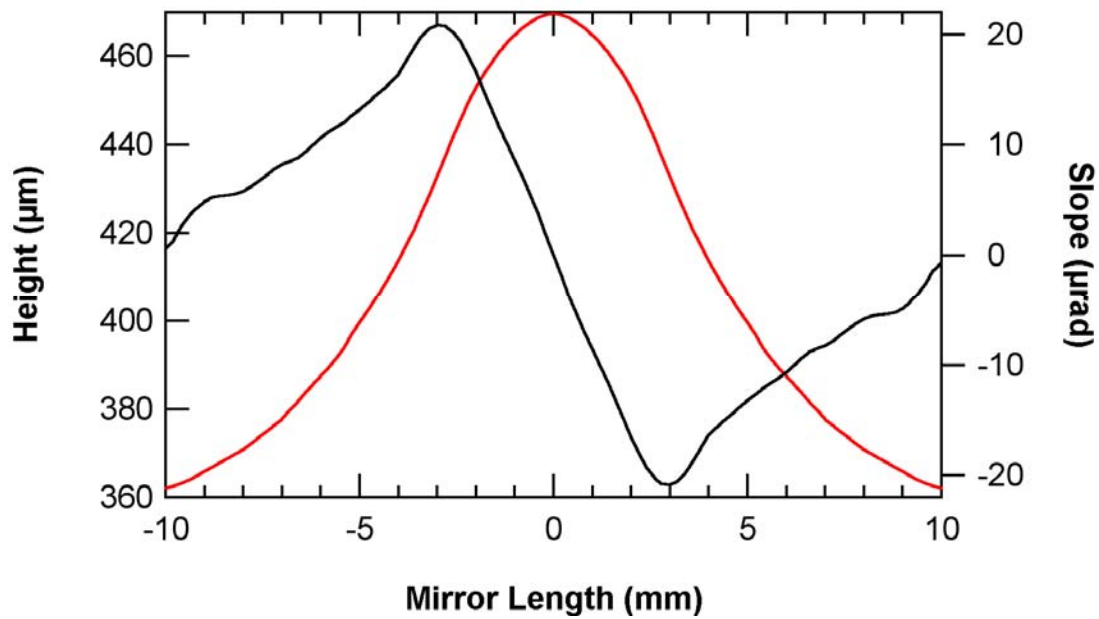
Figure 24. M2 Surface deformation (red trace) and sagittal slope error (black trace) at zero length.
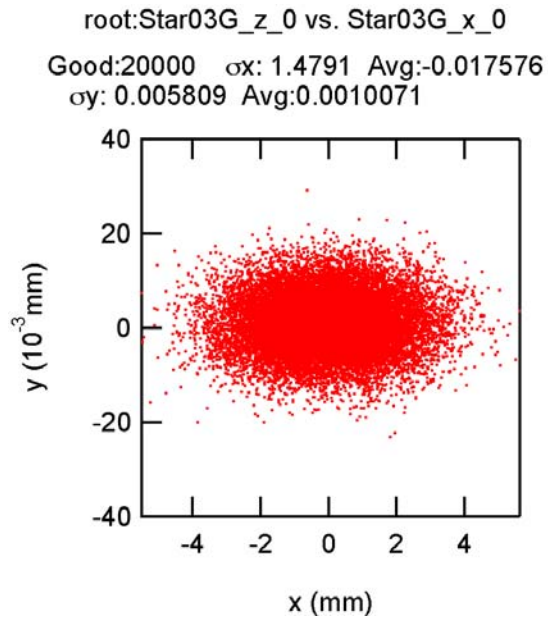
Figure 25. Ray tracings at the exit slit plane with perfect optics
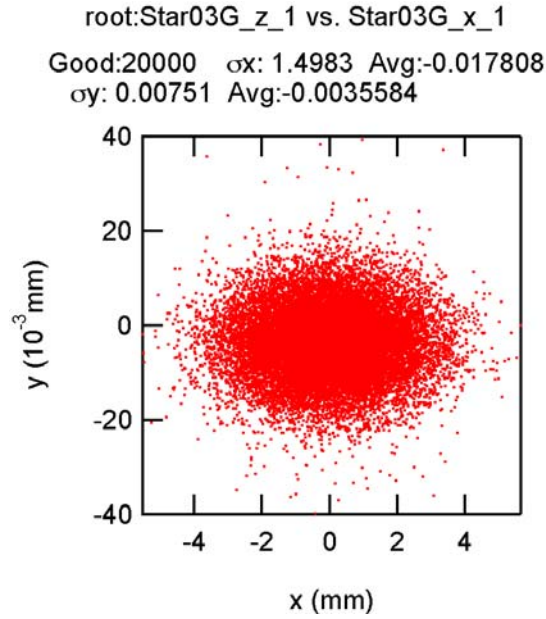
Figure 26. Ray tracings at the exit slit plane with deformed M2.
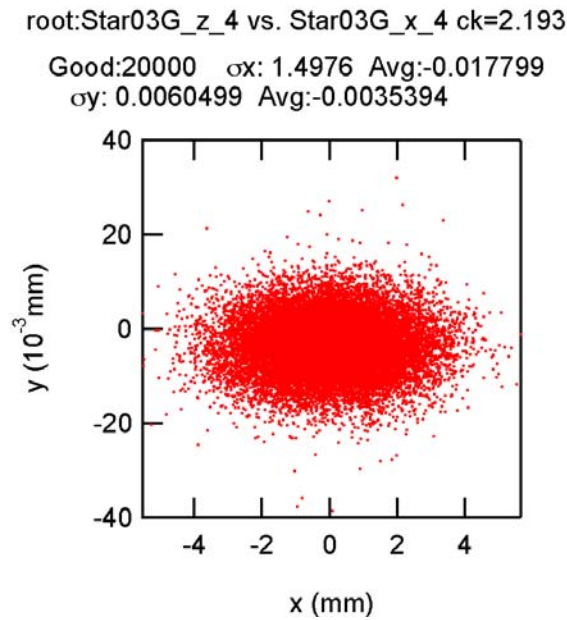
Figure 27. Ray tracings at the exit slit plane with deformed M2 and optimized c value.

root:Star03G_z_0 vs. Star03G_x_0
Up rho=1338.9 mm
Good:20000   σx: 1.4804 Avg:-0.017784
σy: 0.0057115 Avg:0.00030765

root:Star03G_z_1 vs. Star03G_x_1
Up rho=1287.1 mm
Good:20000   σx: 1.4804 Avg:-0.017812
σy: 0.01113 Avg:0.00026726
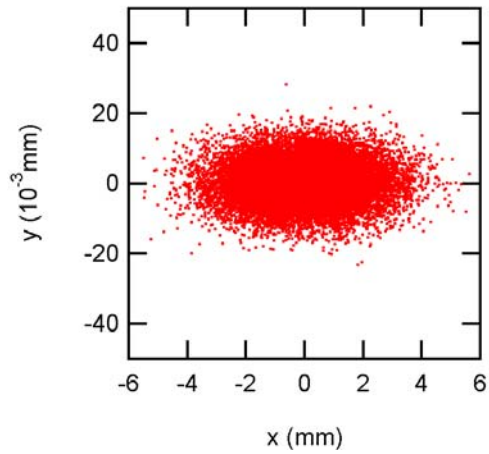
Figure 28. Ray tracings at exit slit plane for the upstream ID with correct M1 radius.
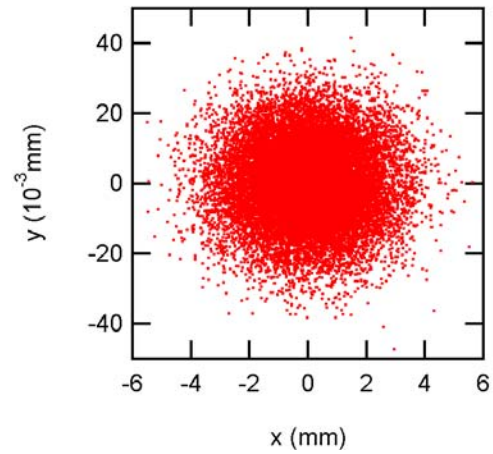
Figure 29. Ray tracings at exit slit plane for the upstream ID with M1 radius of phased IDs.

Appendix E. M2 Finite Element Analysis

A parametrically driven ANSYS input file was developed and employed for 3-D thermal-structural analysis of the M2 mirror in the NSLS2 soft x-ray coherent scattering and imaging beamline. It solves for surface deflections in two passes. The first is a thermal analysis. The second pass has the thermal solution's resulting temperature field as input along with symmetry and other structural constraints and solves for thermal stresses and deflections. It allows for temperature dependencies of some properties; varying number, dimensions, and depth below heated surface of rectangular longitudinal coolant passages; variation in overall dimensions of the mirror substrate, changes in size, location or intensity of mirror heating; and certain other variations, with single parameter value changes in some cases and modest editing of the model file in others. Currently these variations are constrained by interaction with the definition of the heat load. Further development to support significantly spatially varying power densities will allow simulation of additional load cases. This work was performed with perhaps the most demanding defined load case, single-beam 183eV operation of the beamline.

Properties of bulk single-crystal silicon were gathered. Temperature dependencies of thermal conductivity and thermal expansion coefficient[1] were included in the model file. Data[2] for directional thermal conductivity below 40 degrees K was found, showing the anisotropy disappears in the range above 30 K, so the conductivity was treated as isotropic in our range of interest. No data for directionality of thermal expansion was found. (It would seem reasonable that if structural stiffness varies with direction that there would be some variation in thermal expansion as there is in other anisotropic materials. But in the absence of directional property data, we do not model directionality of thermal expansion.)

Beginning with coolant and heat transfer parameters as well as coolant passage geometry matching the Diamond I06 beamline, some simple optimization simulations were made. Peak temperature was used as a proxy for the optical surface deformations we desire to minimize. These preliminary optimization runs resulted in a move to 1.5mm thick silicon between coolant passages and a reduction to 1mm between the optical surface and the beginning of the coolant passages. These parameters are within the range of what is workable for silicon optics manufacturers such as InSync to produce with good optical figure. A number of ANSYS FEA runs were then made using this basic set of parameters. A subset will be documented here. Initial results were compared to the closest case documented in the Diamond I06 TDR as an additional check on the modeling accuracy in this work. Several models were rerun to generate graphics files from model development to results path plots.

There are a number of simplifications and approximations in common among all ANSYS models of the M2 mirror to date. The silicon is treated as isotropic rather than orthotropic structurally. This is a significant approximation structurally (in how the silicon responds structurally to the thermally produced strains). The coolant passages as modeled run the full length of the optic, and the back of the optic is solid; a real optic will require UHV-tight end manifolding of the coolant slots and inlet & outlet connections on the back with air guarding. The optic is modeled with symmetry constraints to exploit left-right symmetry. (Because the location of the heat load in general is not centered axially, only bilateral symmetry is present in the model, not four-fold as is often modeled.) The thermal effects of the glass frit bond are treated as negligible, which is rather optimistic given the thermal resistance of the approximately 50 micron layer can equal that of several mm of silicon. The bulk temperature of the coolant is held constant at 23°C. Heat transfer coefficient is treated as constant, invariant to both silicon surface temperature and location in the flow channel. Geometric effects such as the slope increasing on the front portion of the heat bump and thereby raising its power density are minor and safely ignored; peak meridional slope of about 14 microradians change was observed at the front & back of the heat input area of 6 degrees grazing incidence, giving about ±0.013% power density change. The effect of mirror coating is trivial since the gold over chromium is nominally only 30nm thick, one millionth the substrate thickness or less. It is also likely that the thin film's conductivity being lower than that of bulk properties[3], approximates that of silicon, reducing this error further. The change in shape of the optic due to other influences including manufacturing tolerances, gravity load, support clamp loads etc. are

ignored. Structural effects of the thin coating and frit layers including residual stress and differential thermal expansion are also ignored. Differential pressure between the coolant passages and vacuum surface are ignored. Optical figure error as manufactured is ignored.

1. Basic Mechanical and Thermal Properties of Silicon, Virgina Semiconductor Inc. http://www.virginiasemi.com/pdf/Basic%20Mechanical%20and%20Thermal%20Properties%20of%20Silicon .pdf

2. Anisotropic Heat Conduction in Cubic Crystals in the Boundary Scattering Regime, Physical Review B, Volume 2, No. 10, pages 4077-4083.

3. Strain and size effects on heat transport in nanostructures, Journal of Applied Physics, Volume 93, No. 6, pages 3535-3539.

Thermal load & optic parameters were as follows.

Table 1. Parameters comparison.

Parameter	As initially described	As modeled in ANSYS
Power deposition, W/mm^2	Nearly flat at 0.354 to 0.365 (maximum variation from average is 2.36%)	Flat at average 0.36223
Size of region with power deposition	5.4 x 48.045 mm	5.4 x 48.046mm
Location of center of beam spot	307 or 307.3mm downstream of upstream end	307mm downstream of upstream end
Taper in area illuminated due to beam divergence	(not described)	Divergence treated as zero
Mirror substrate overall length mm	<380	380
Mirror substrate overall width, mm	100	60
Mirror substrate overall thickness, mm	unstated	30

Following are details of a coarsely meshed run for 5 coolant partitions ("fins") per mirror half. For modeling convenience the optic was modeled upside down as shown in the figure below. The heat load is applied on a 48.046 mm long stripe 2.7 mm wide from the origin to the slanted line shown in the figure. Note, the system of units defined & used through the simulation runs is mm, gm, second, degrees C, coulomb, newton, & joule. Consequently stresses are displayed in N/mm^2 (MPa).
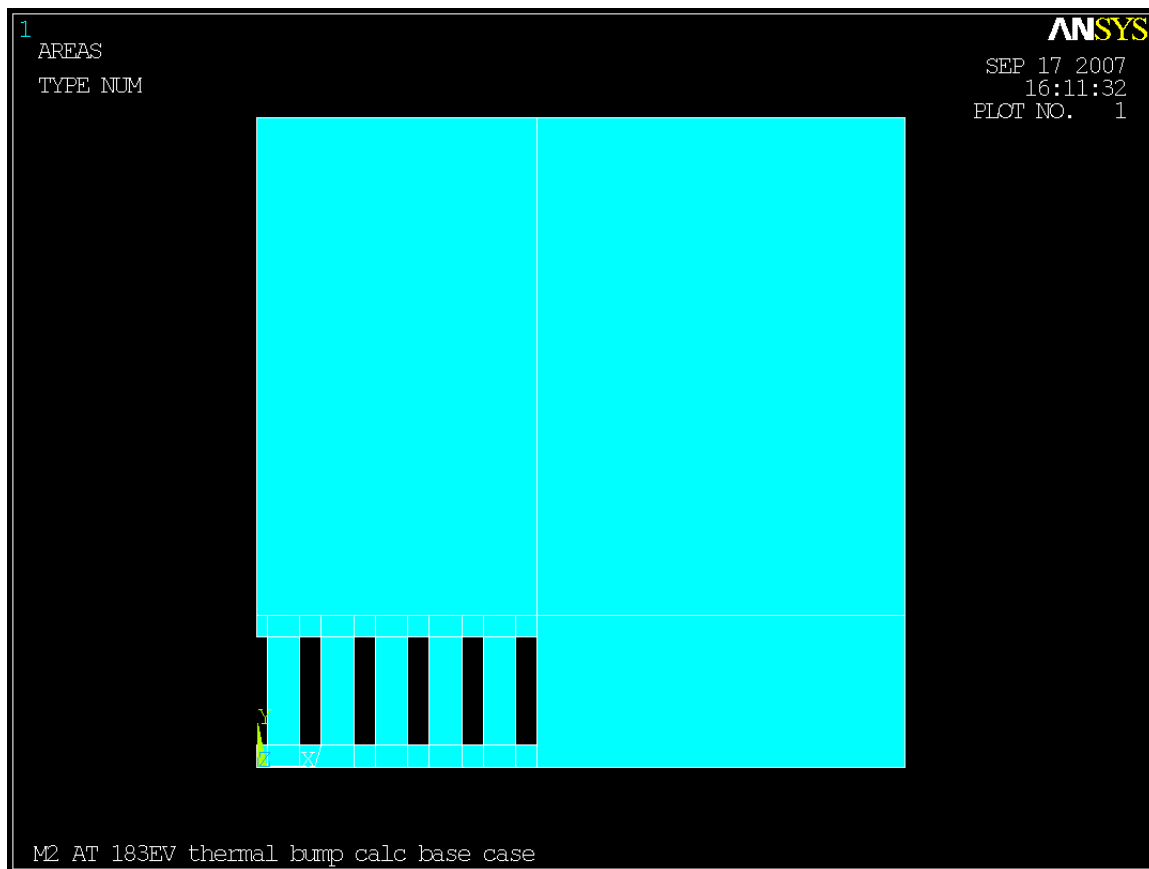
Figure 30. Silicon area shown in color; symmetry plane is at left.
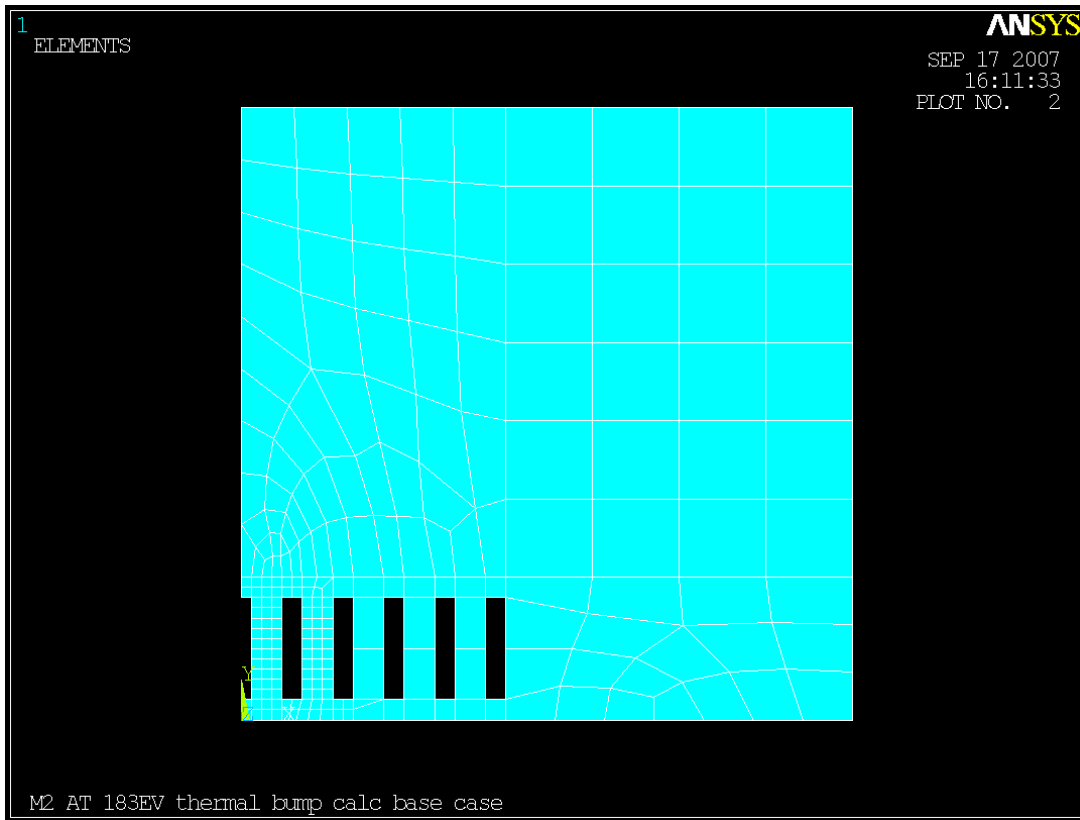
Figure 31. Initial meshing end view
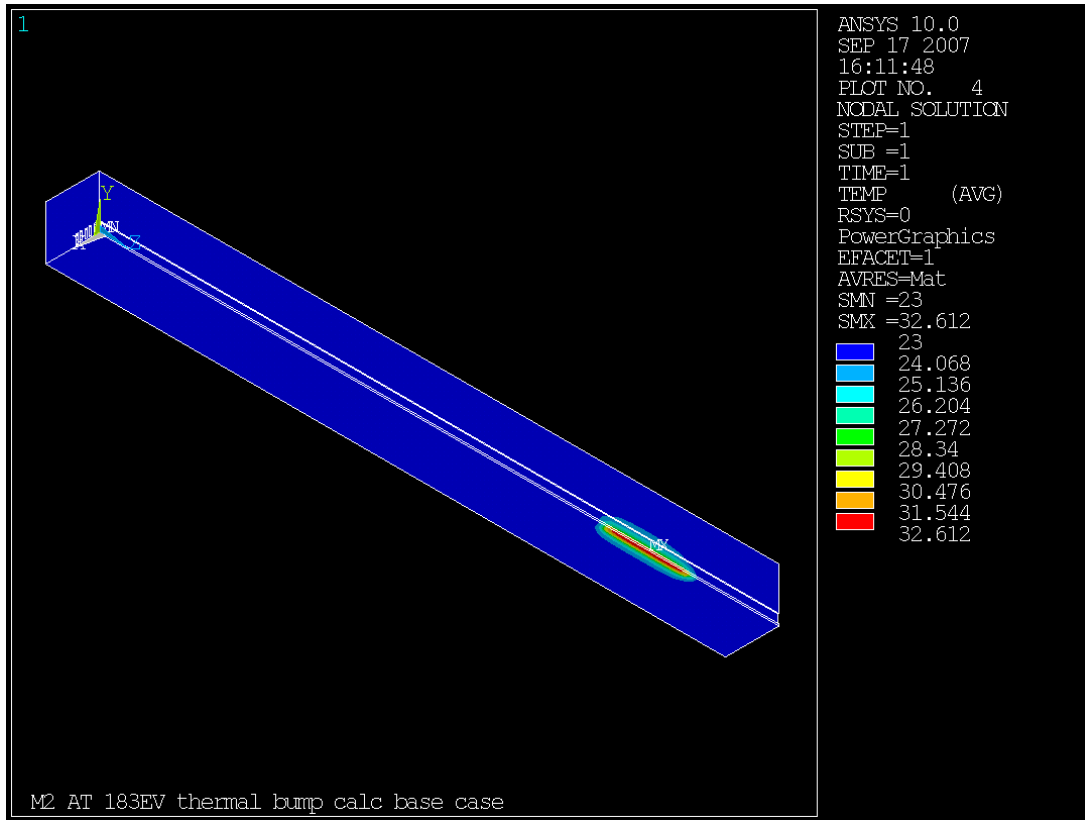
Figure 32. Thermal response, degrees C.
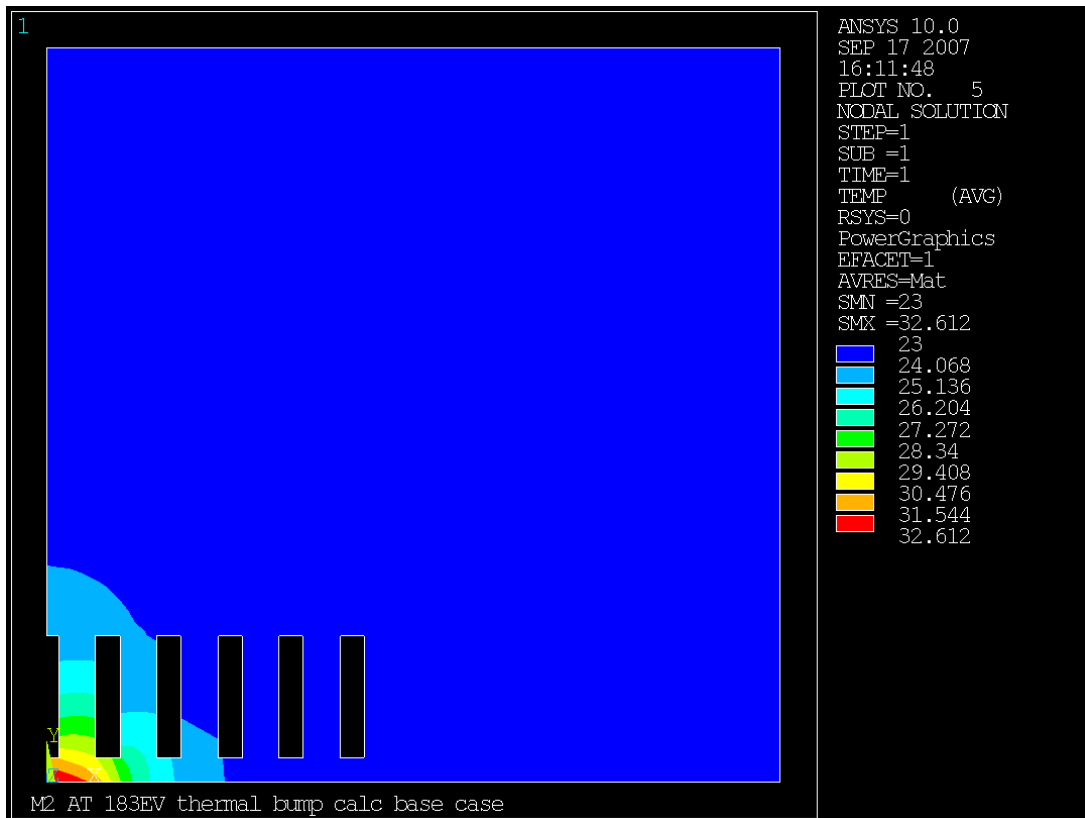
Figure 33. Thermal response at section through midpoint of heat load (Z=307mm).
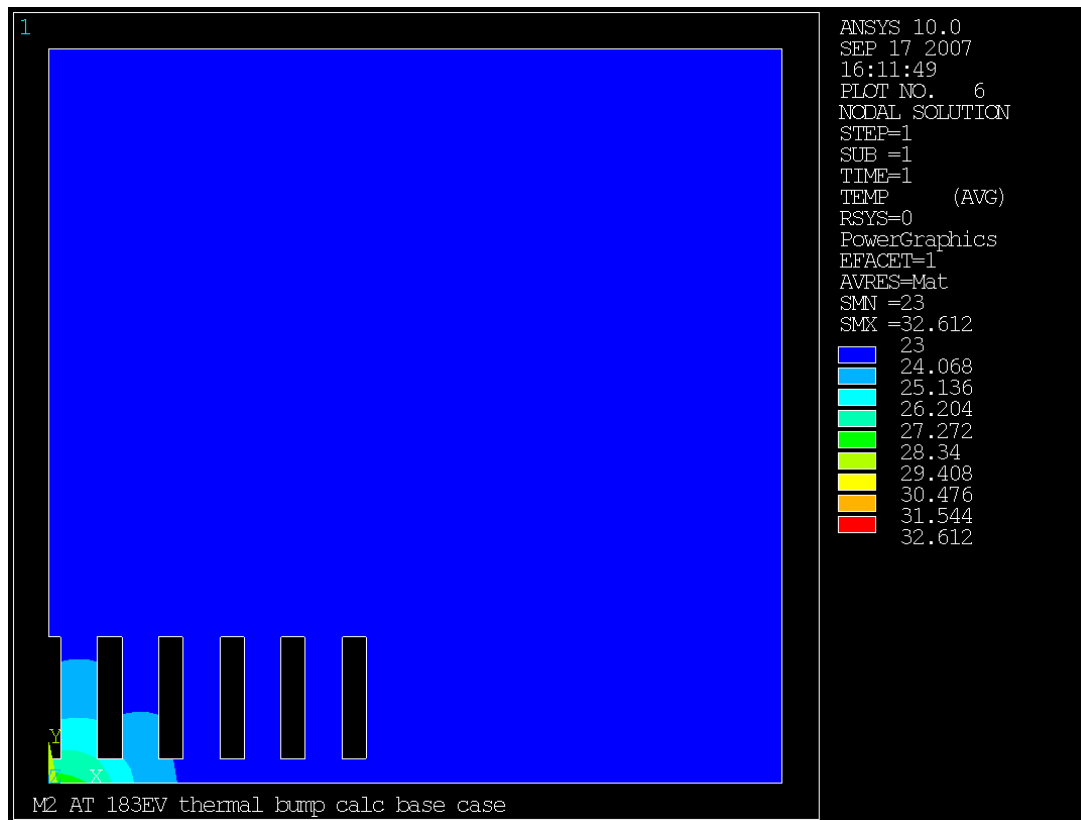
Figure 34. Thermal response, section through upstream edge of heat load (Z=283mm).
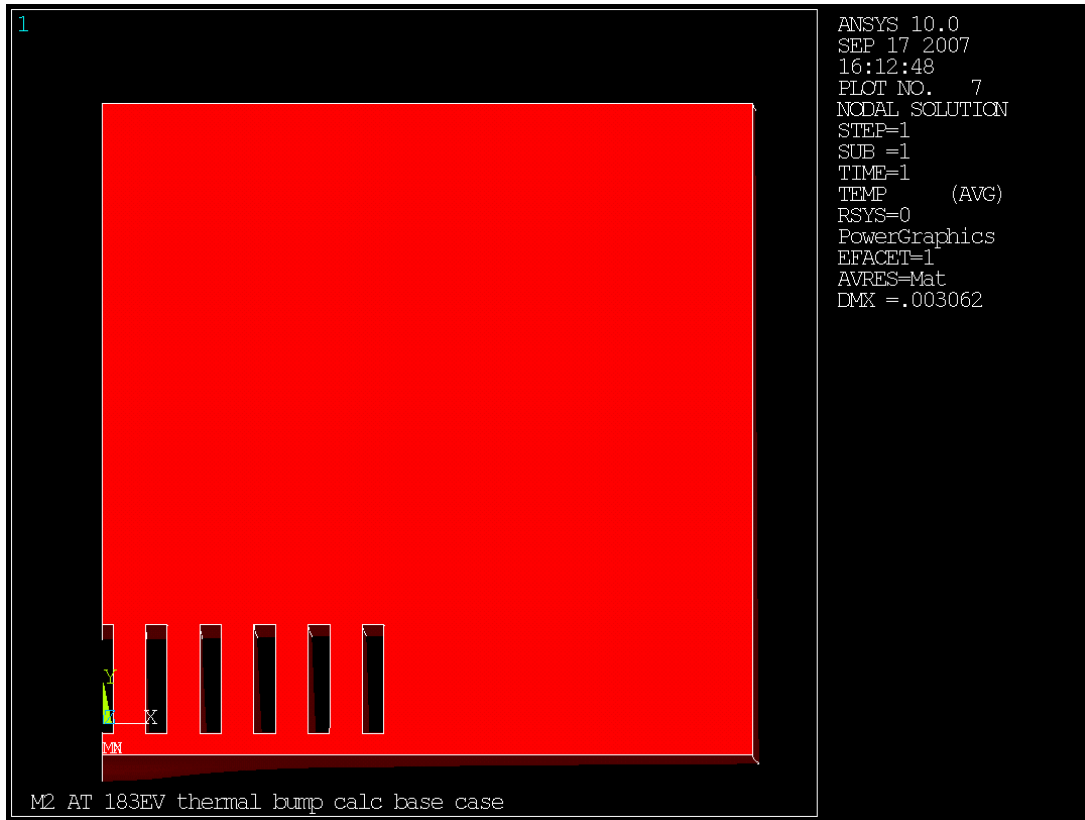
Figure 35. Exaggerated deformation end view.
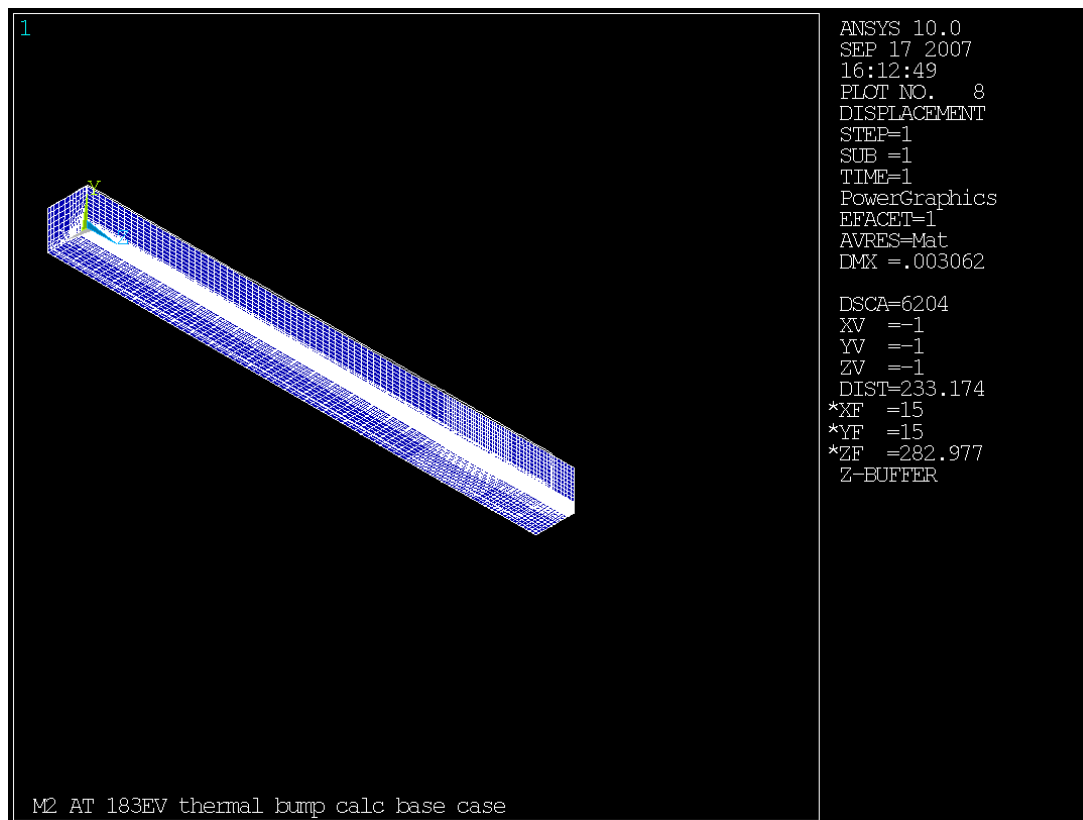
Figure 36. Displacement plot showing deformed and undeformed mesh; uniform thermal expansion dominates under the modeled conditions.
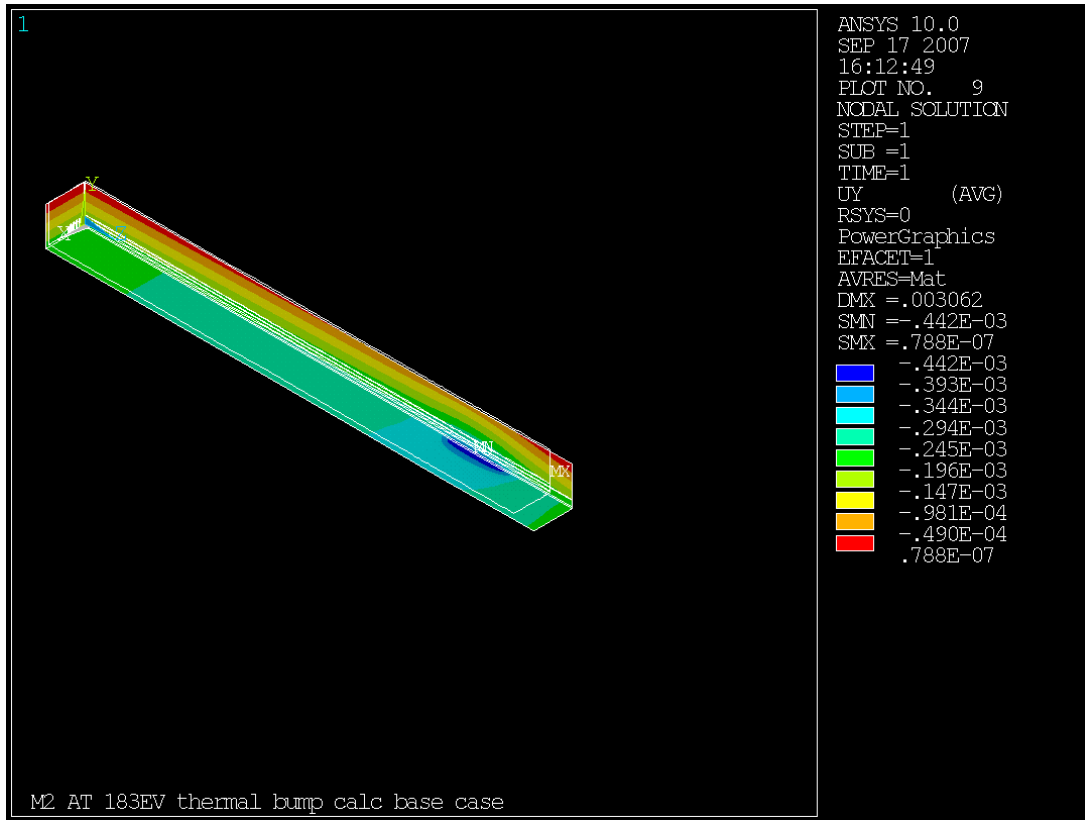
Figure 37. Displacement normal to the optical surface. Longitudinal bending and uniform thermal expansion dominate in producing the gross deflections.
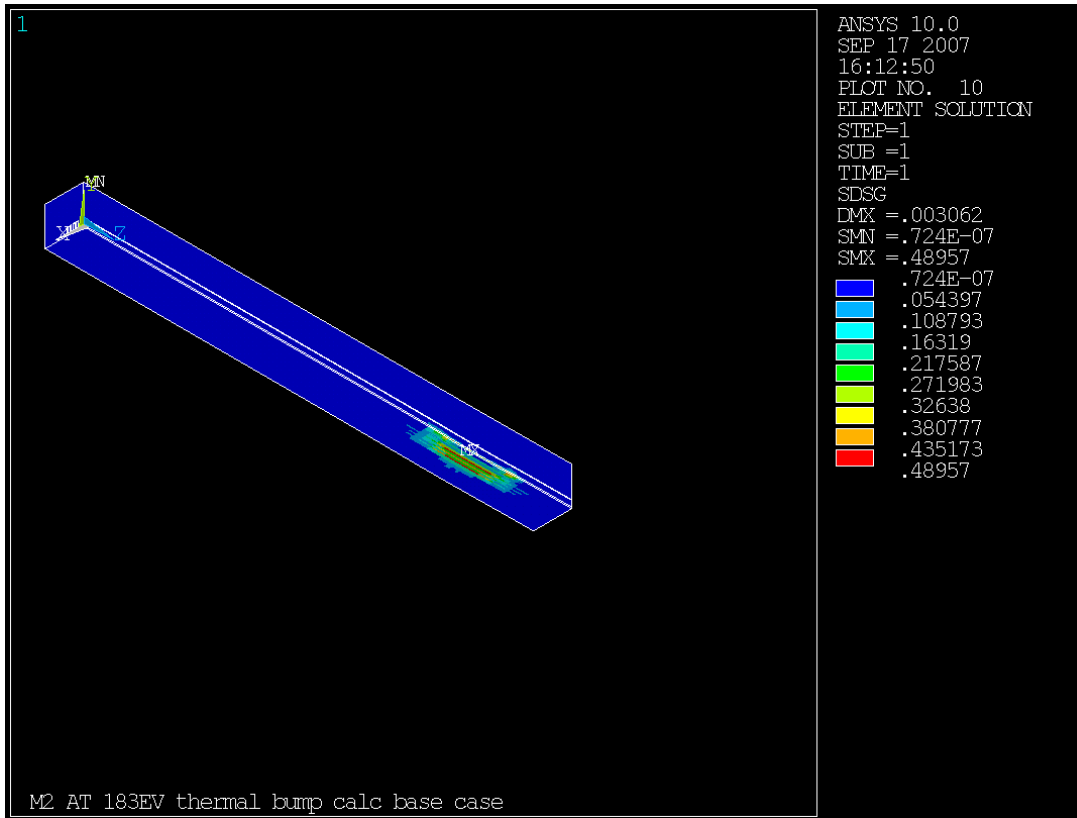
Figure 38. Absolute value of the maximum variation of any nodal stress component. Magnitude is high enough that calculated stresses should be regarded as very approximate.
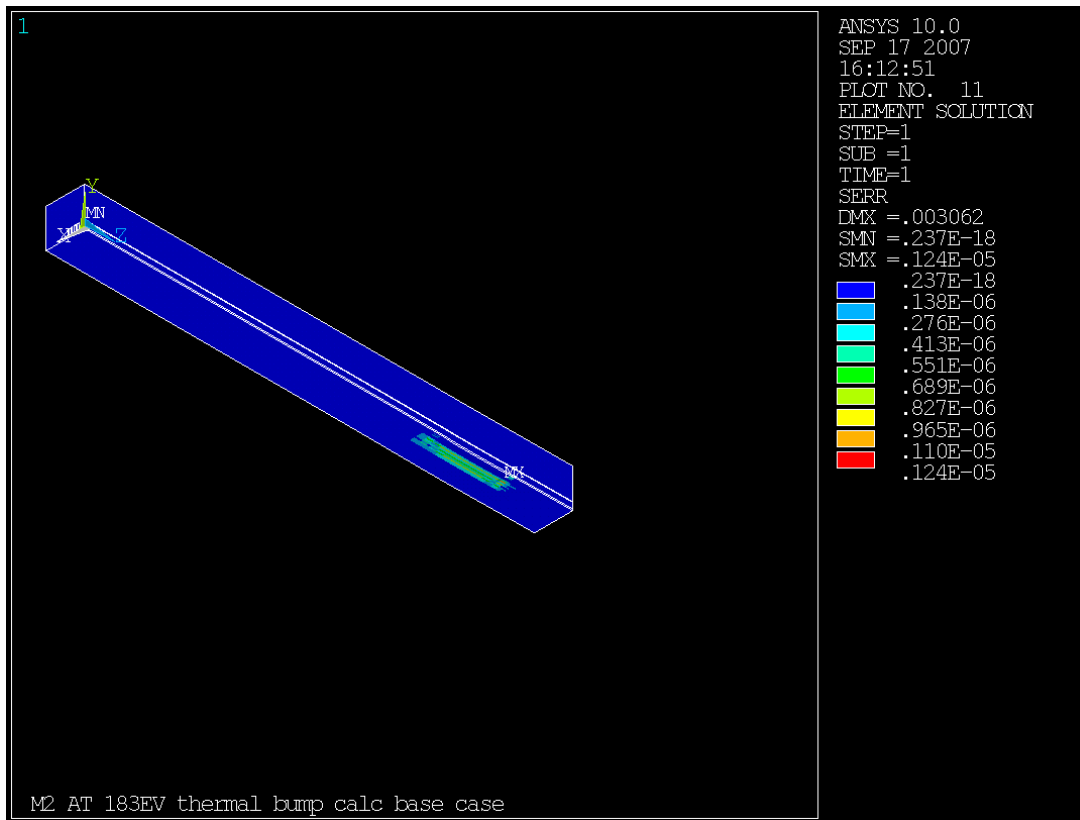
Figure 39. Energy error for the elements.
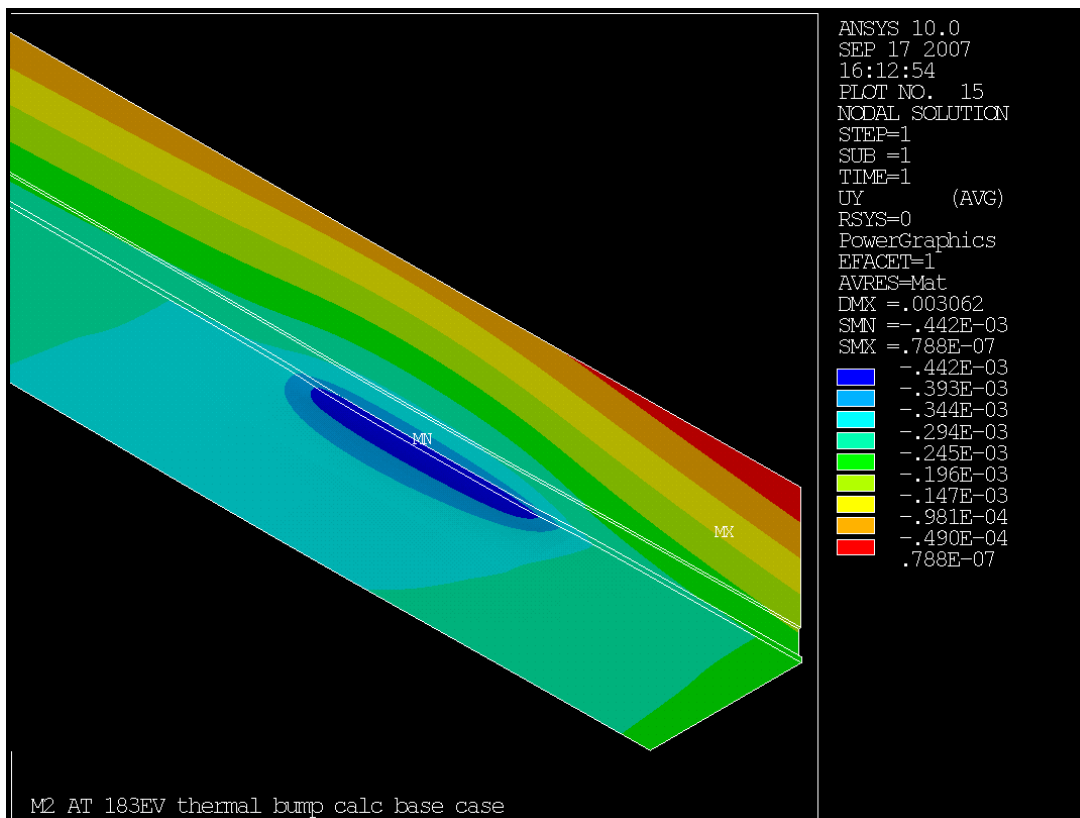
Figure 40. Displacements normal to optical surface at heat load and downstream end.
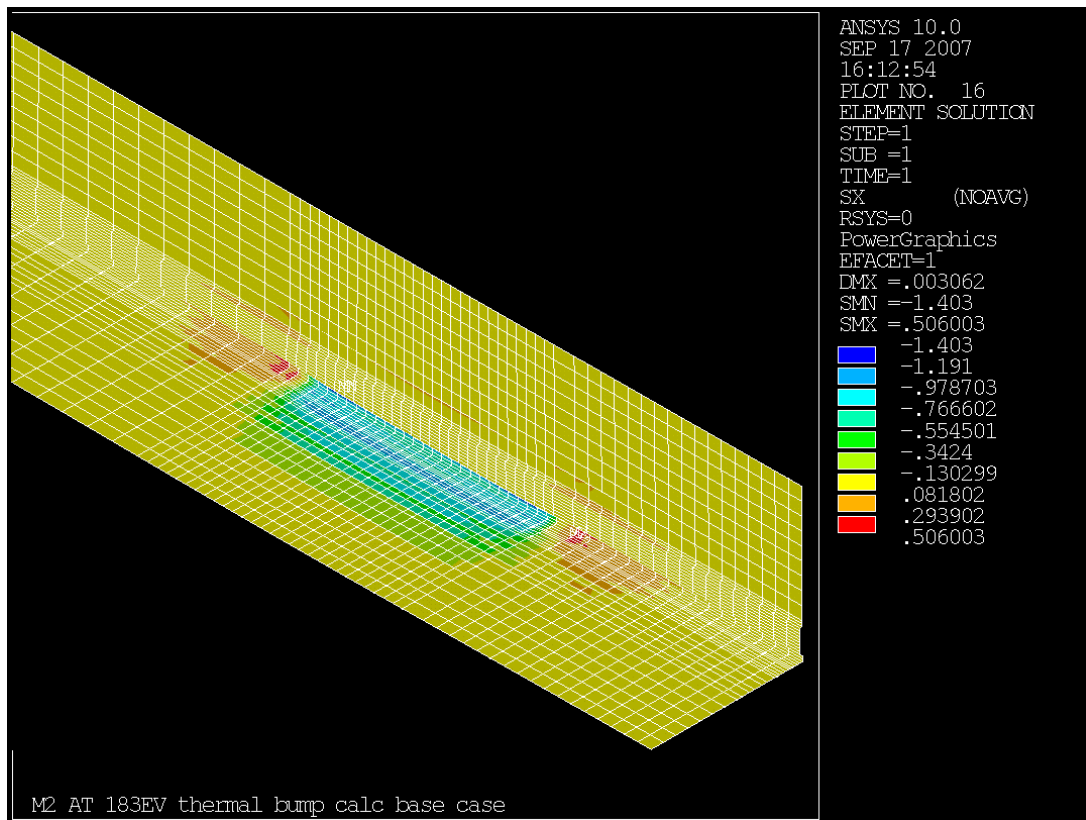
Figure 41. X axis stresses.
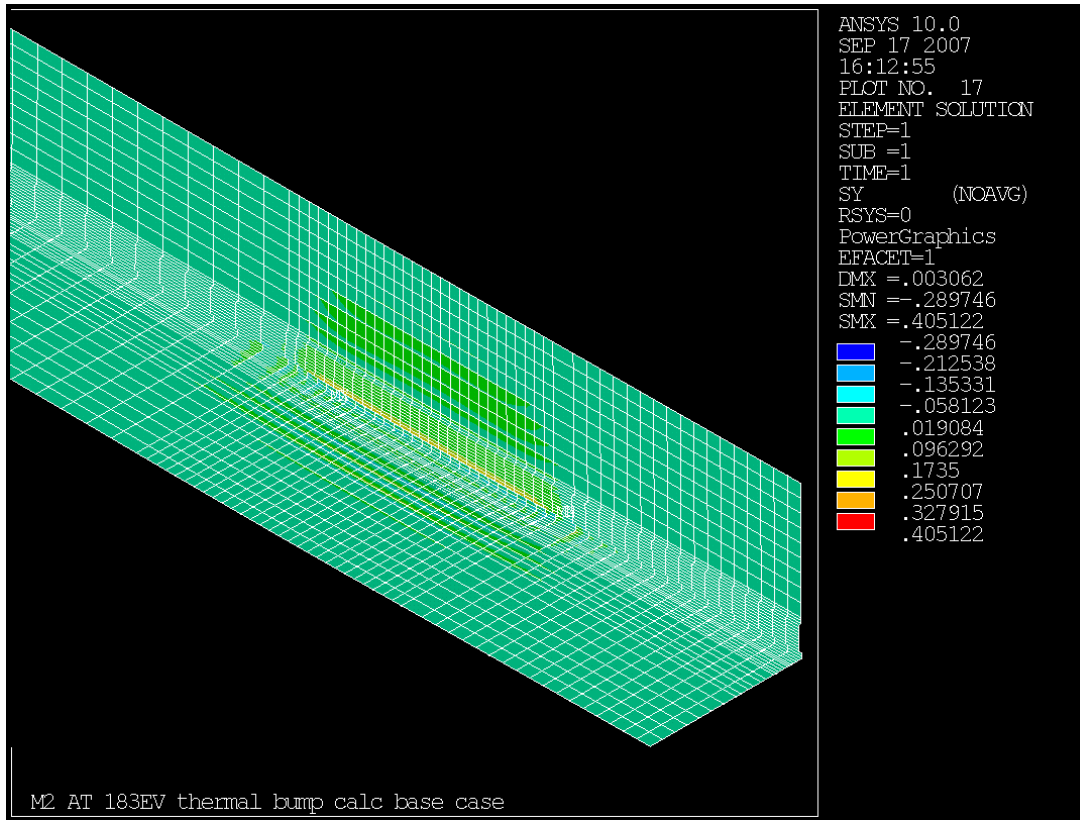
Figure 42. Y axis Stresses.
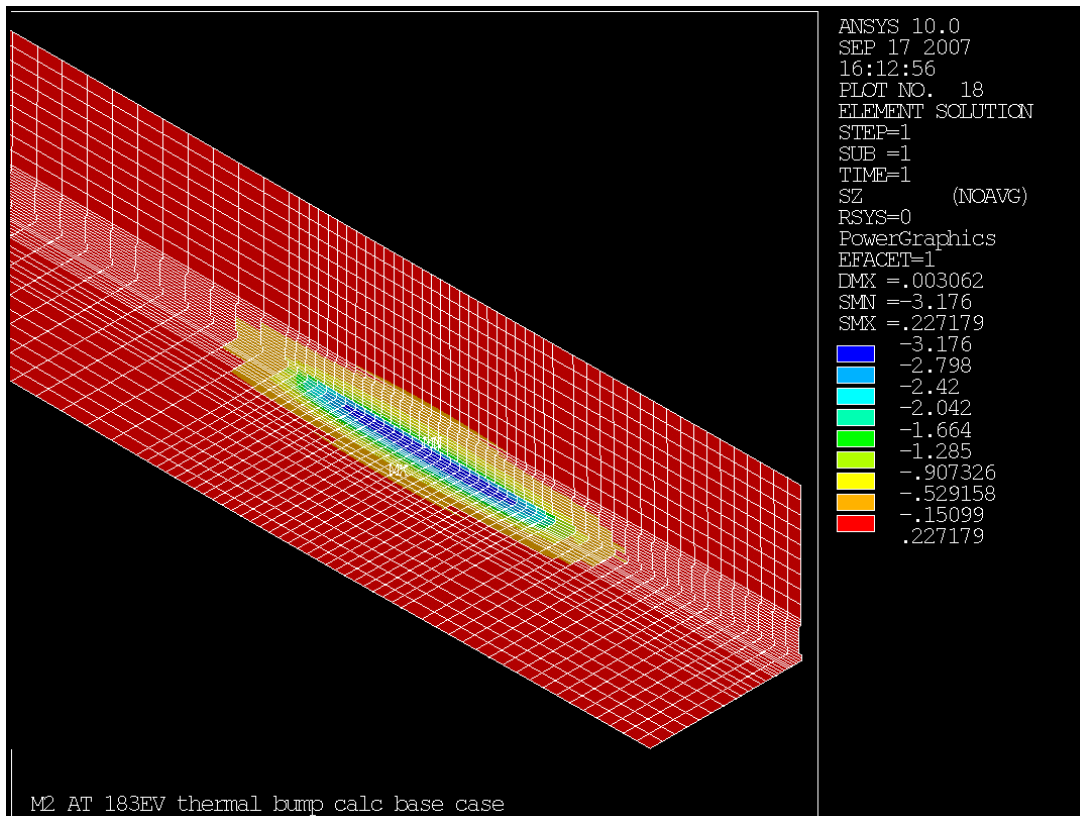
Figure 43. Z axis stresses. Contours resemble the temperature contours and the surface normal displacements.
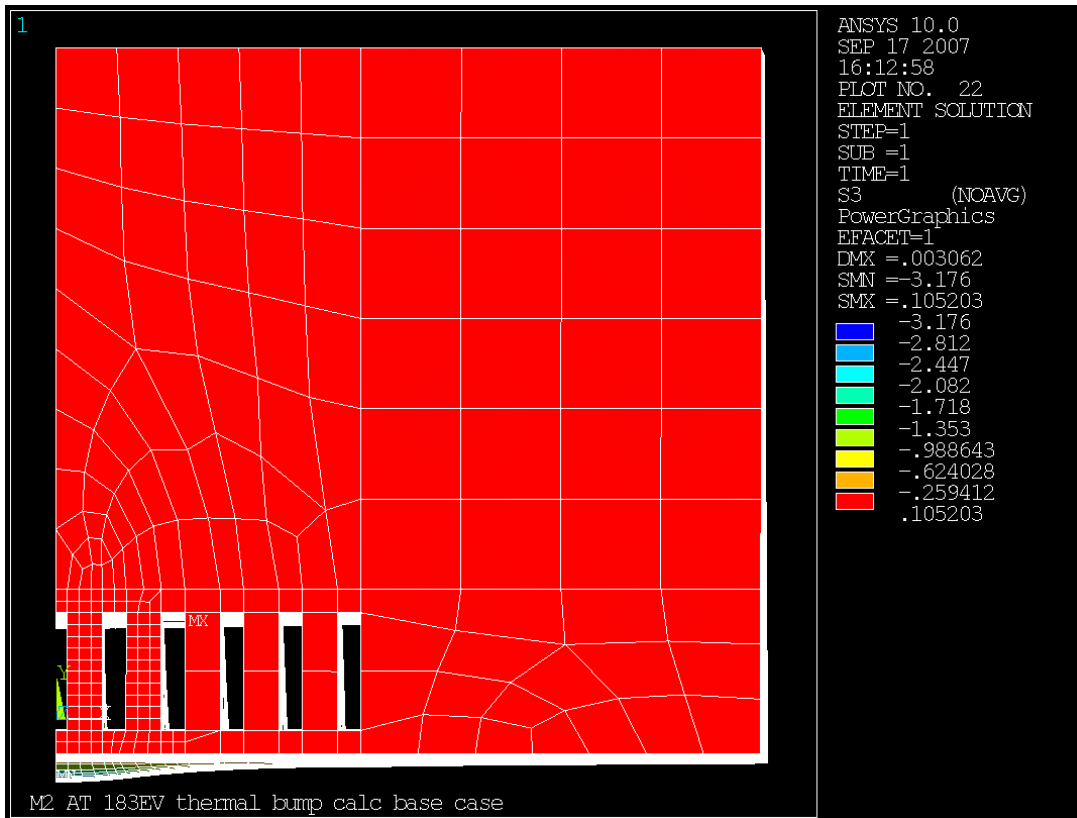
Figure 44. Third principal stress.

ANSYS path plots were generated for meridional and sagittal displacement and slope, with 380 points per meridional and 300 per sagittal plot. Small point counts (even considerably above the ANSYS default) result in the peak value of slope being understated in the path plots. The high count needed to represent the peak seems to introduce artifacts elsewhere in the sagittal slope plots.
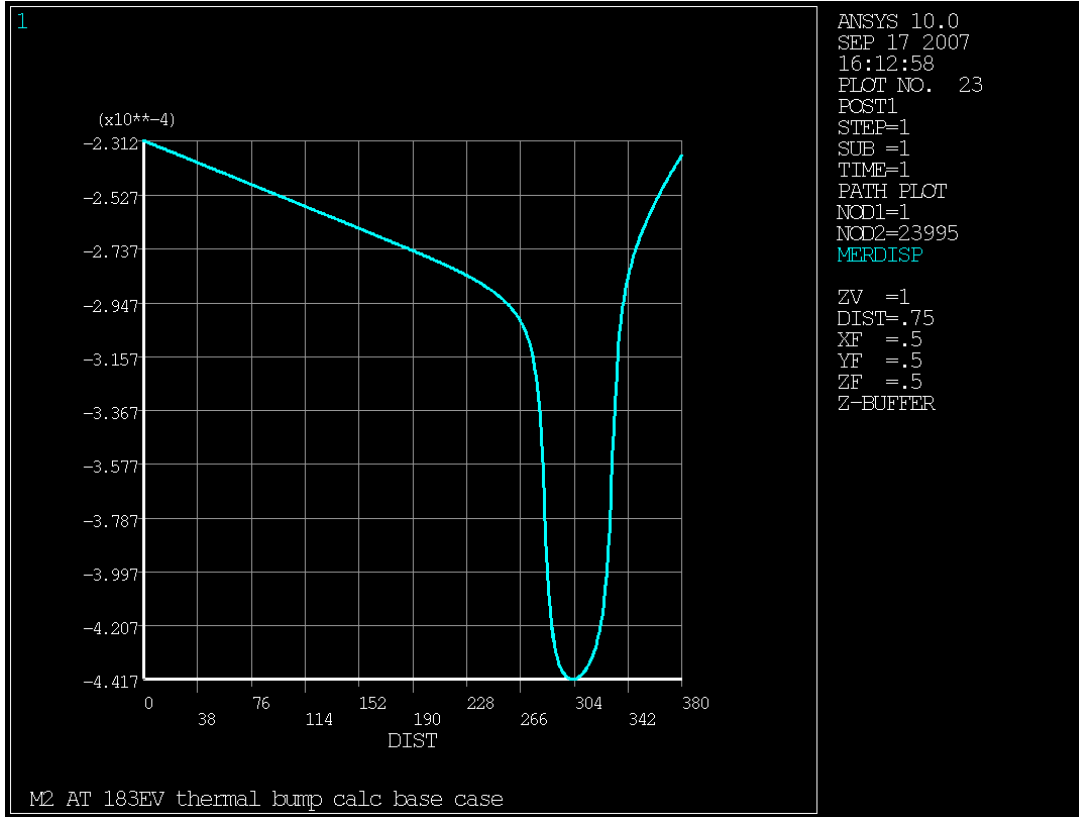
Figure 45. Meridional displacement plot, mm. Displacement is unequal at the two ends because the Z=380mm end is warmer than the z=0mm end. Peak displacement occurs shifted upstream from heat center for geometrical reasons.
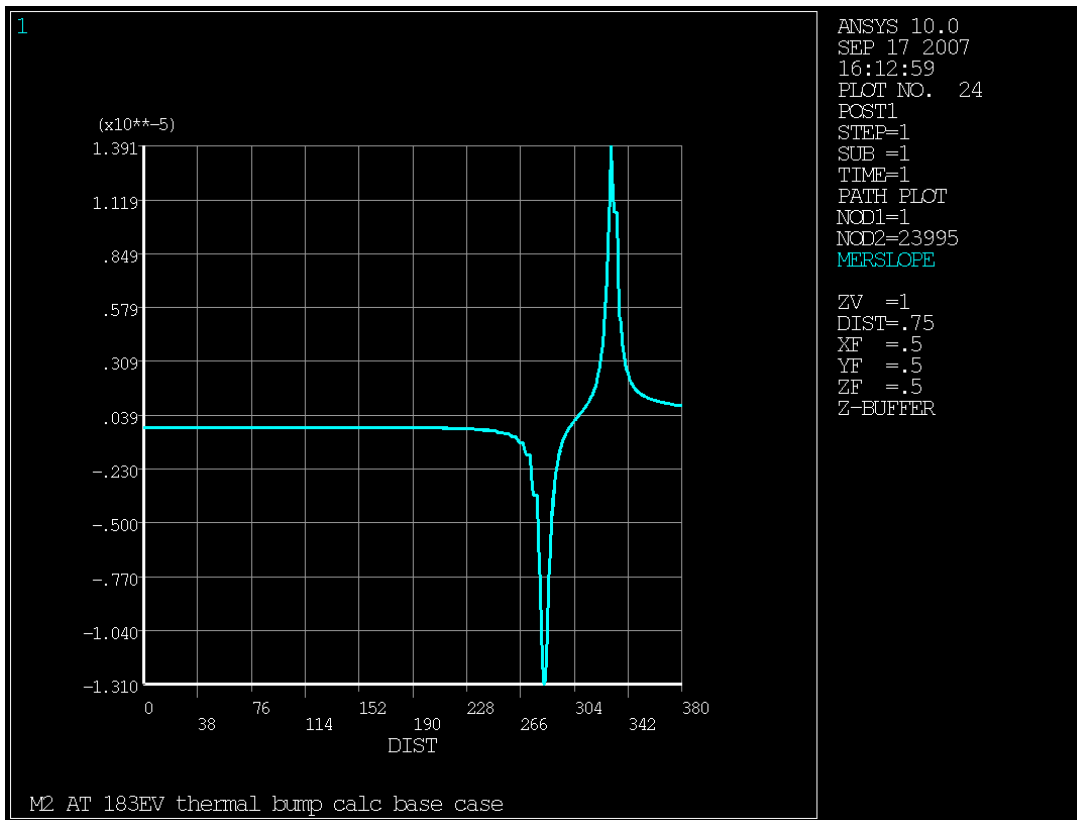
Figure 46. Meridional slope plot, radians. High curvature peaks occur at the front and back edges of the heat input area. The central slope is correctable but the end peaks are problematic.
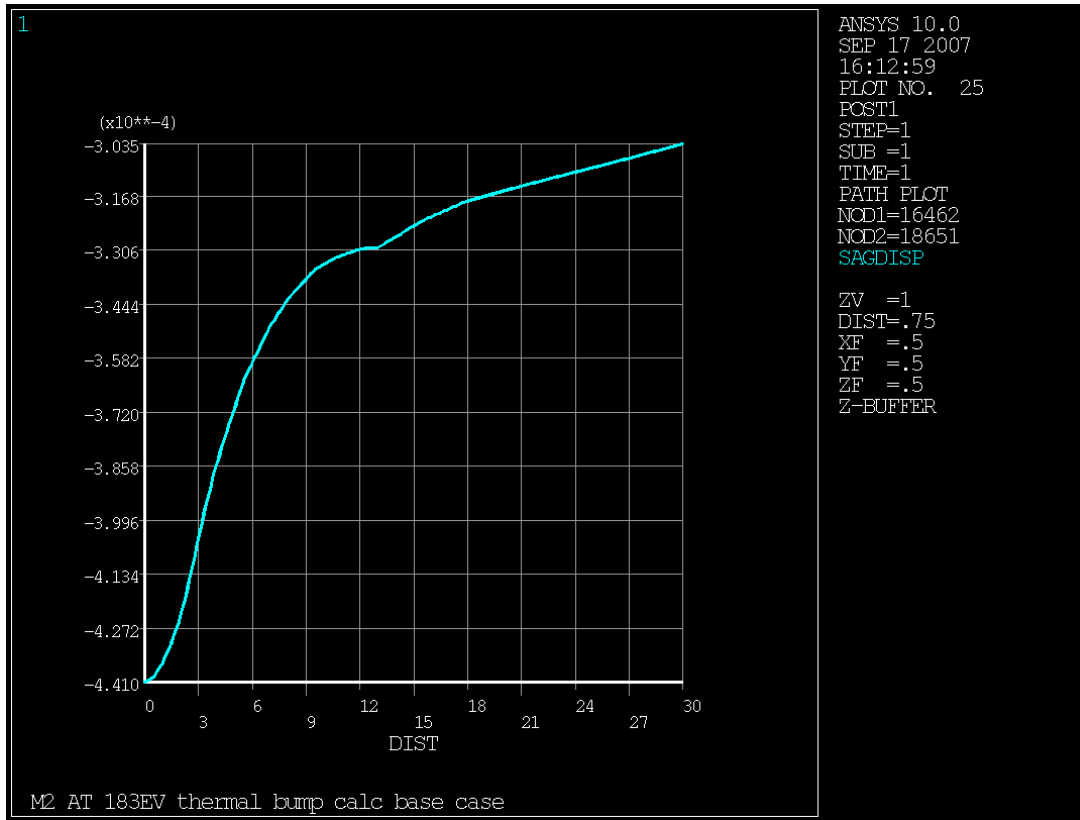
Figure 47. Sagittal displacement (mm) plot on path across midpoint of heat spot (Z=307mm). The range from 0 to 2.7mm is of interest for correction and appears highly correctable.
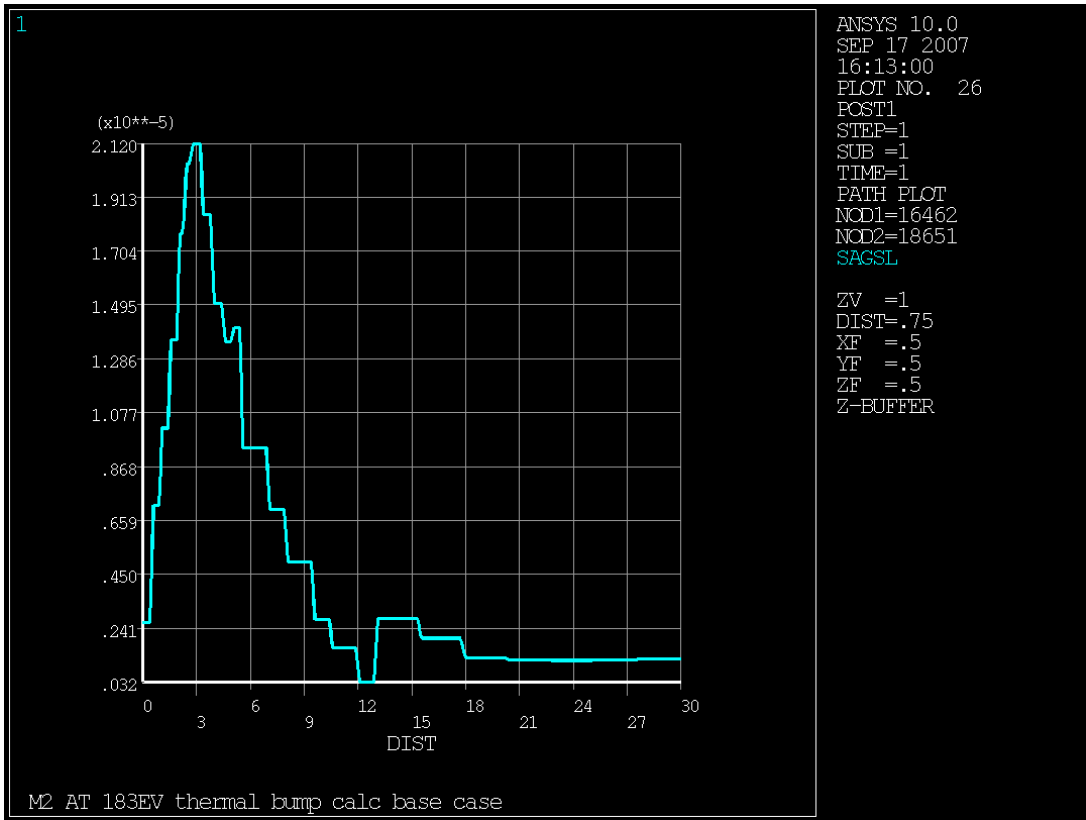
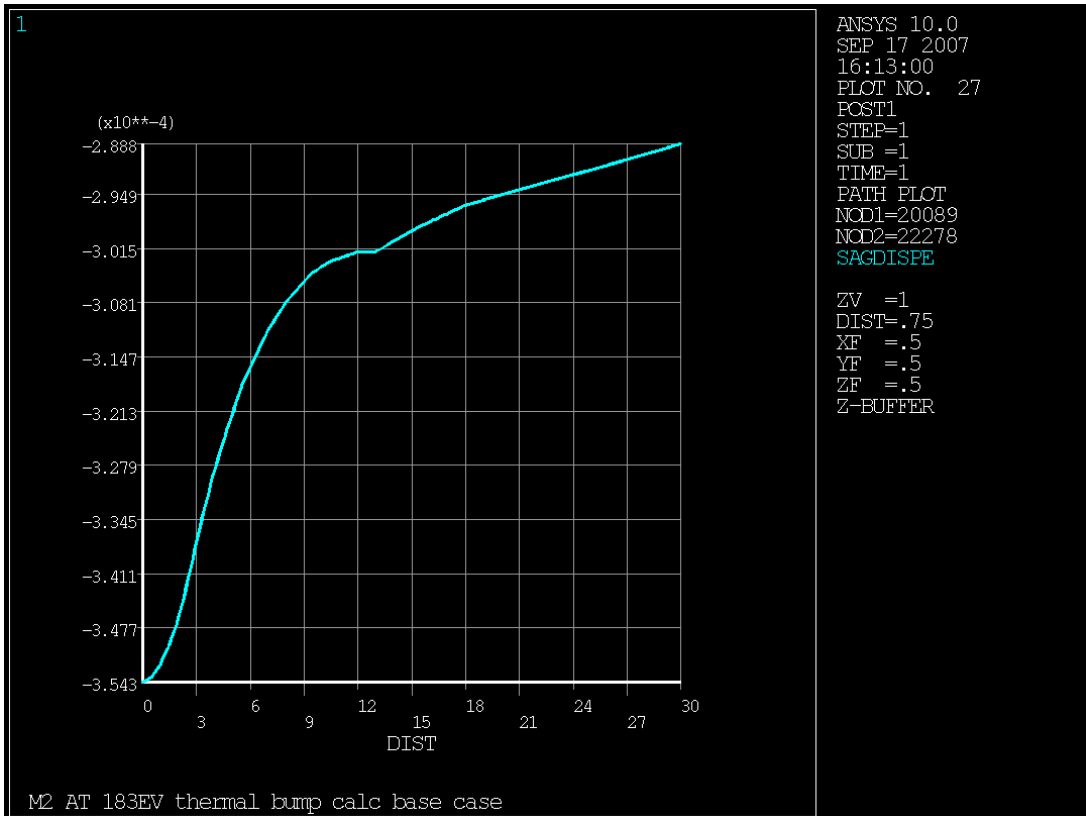**Figure 48. Sagittal slope (radians) on path through midpoint of heat spot (Z=307mm).**

Figure 49. Sagittal displacement on path at downstream edge of heat spot (Z=331mm).
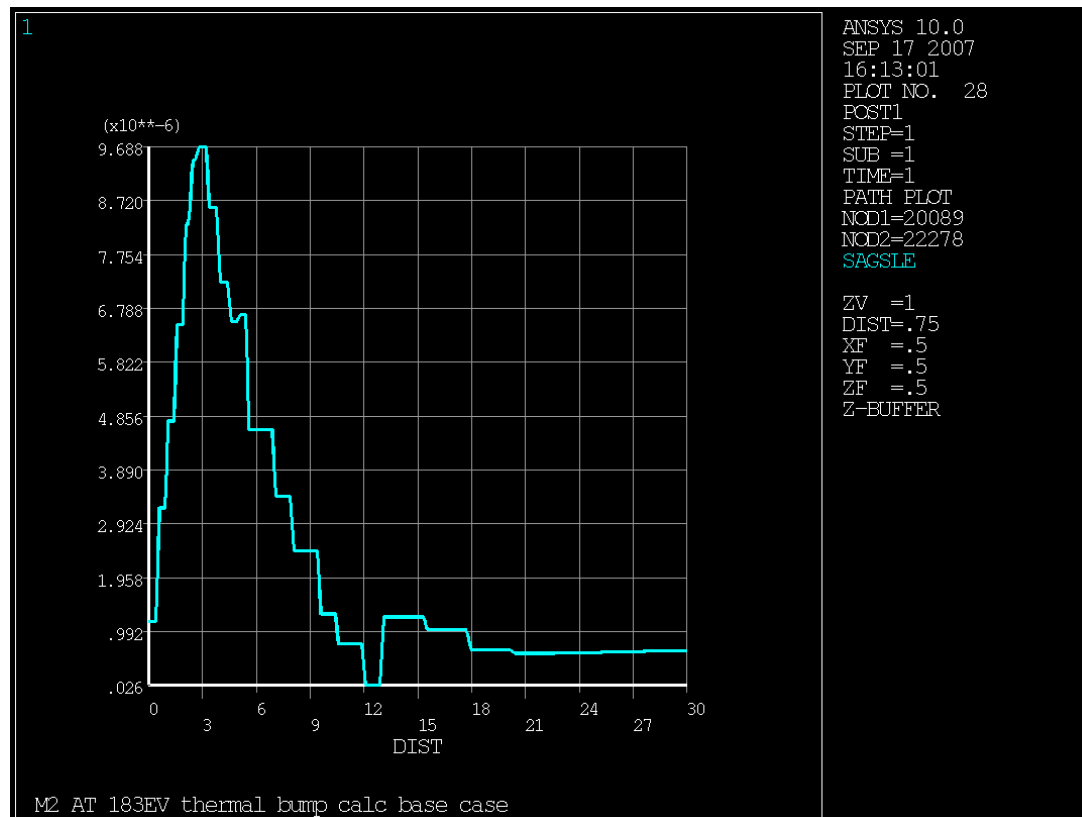
Figure 50. Sagittal slope on path at downstream edge of heat spot (Z=331mm). Note the peak slope is less than half the midpoint peak.

The resulting meridional and sagittal displacements were incorporated into a spreadsheet for analysis of slope and possibilities of compensation. It was determined the standard deviation of meridional slope after second order compensation was still several times too high, but central sagittal slope could be adequately compensated. Runs with a much thicker substrate (100 rather than 30mm) and with 3 fins rather than 5 were made. The 3-fin case showed minor changes in slope variation, with almost all parameters favoring the 5-fin case.

Subsequently a mesh refinement run was made on the base 5-fin case, and the resulting illuminated-surface displacements provided for ray tracing the deformed optic. Displacement and slope values matched within 11 percent between the base and refined runs, while temperature rise matched within one percent, giving confidence in the mesh quality. The ray tracing results predicted adverse effects on beam spot size downstream, confirming the conclusion from the spreadsheet based slope evaluation, and generating additional requests for ANSYS runs.

Some concern was expressed over the asymmetric meridional slopes and displacements such as shown in Figure 16. A model qualification run was made with the heat spot moved to centered axially at z=190mm. The resulting midpoint meridional slope was about -0.504×10^{-17} radians, 10^{-10} times lower than the absolute magnitudes of slope at z=189 and z=191mm, an excellent degree of symmetry. Some very small asymmetry is present since the difference between bulk coolant temperature and material reference temperature leads to axial expansion overall, and the structural constraint applied axially is at the Z=0mm (upstream) end. This would displace the midpoint about 0.5 micron downstream. At a rate of change of slope of 0.50295×10^{-7} radians/mm that is a tiny effect but still a much larger effect than the calculated asymmetry referenced to the midpoint. The asymmetry in slopes and displacements relative to heat spot midpoint is actually expected and necessary, as shown in the following figure.
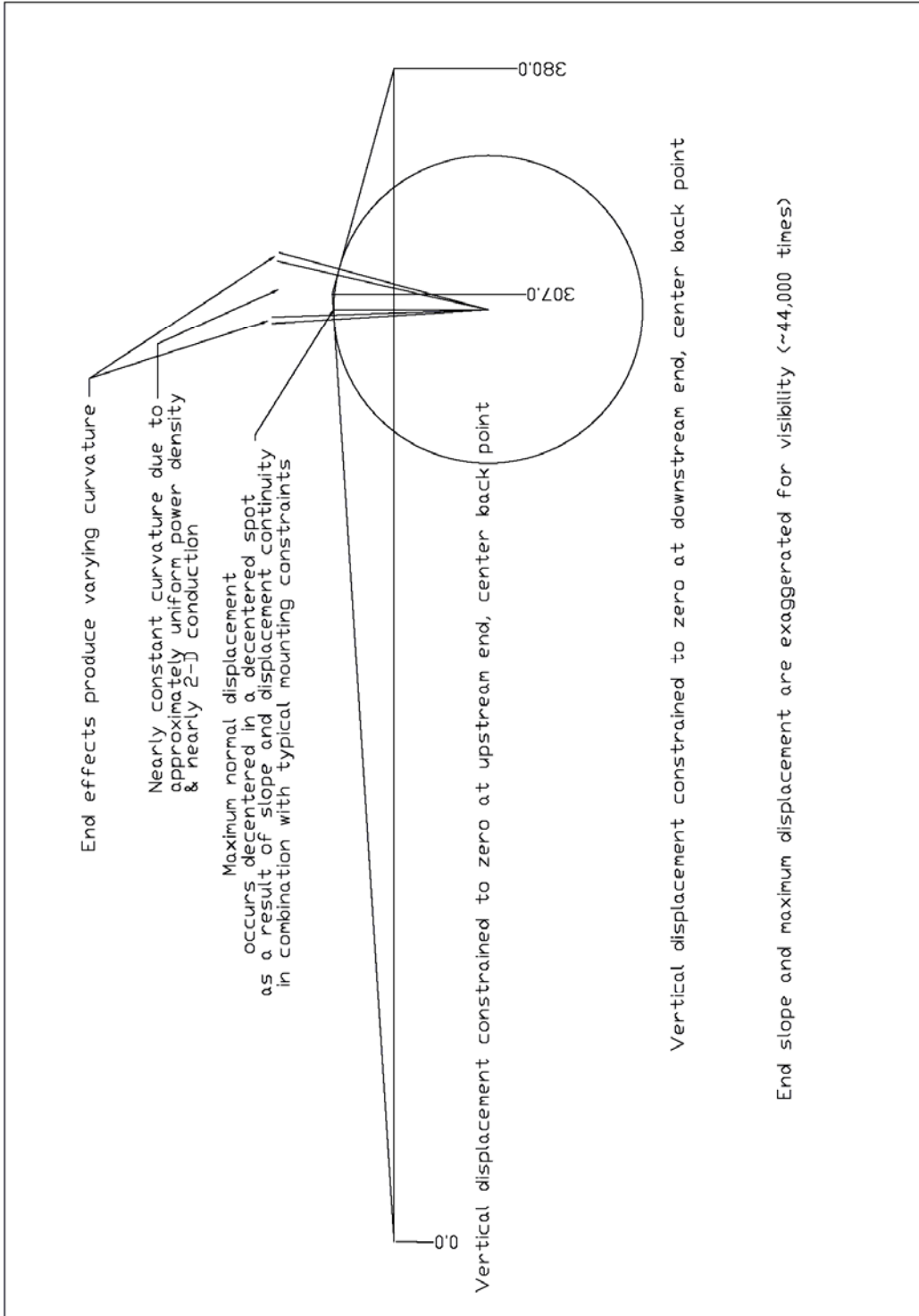
Figure 51. Asymmetric thermal load location generates asymmetric slopes and end displacements. Here the M2 optic is idealized as a slender bar with thermal bending over a segment.
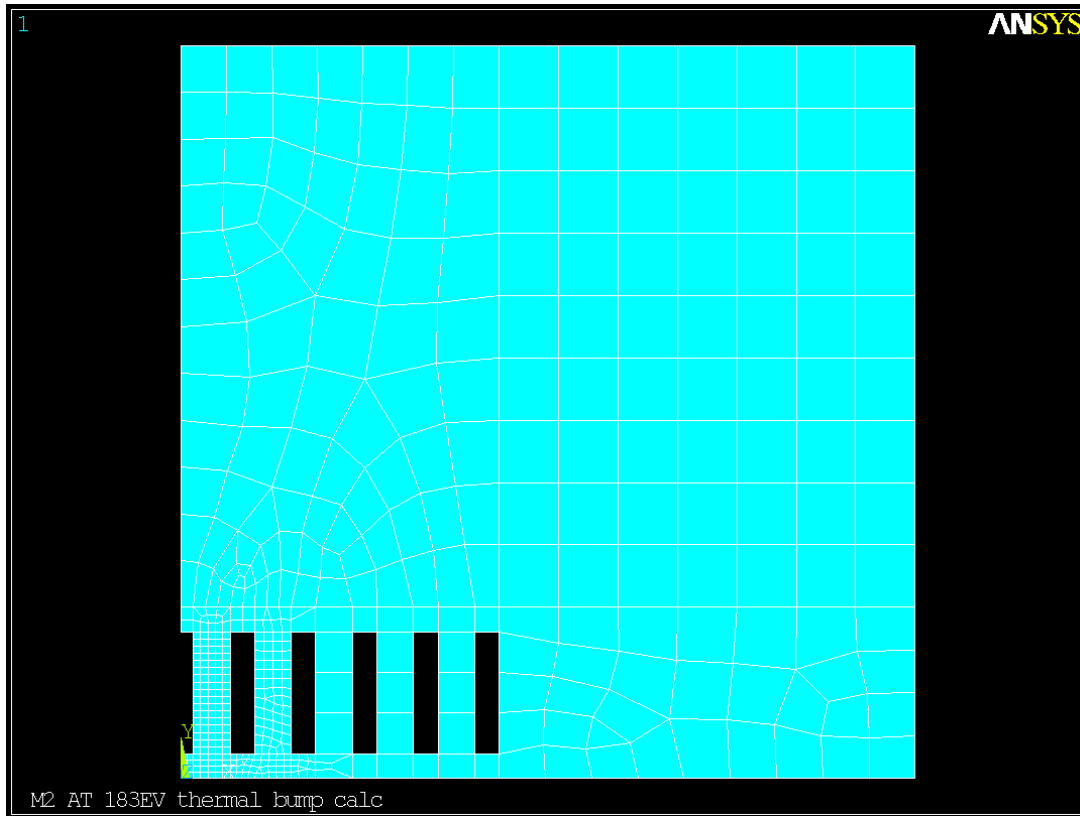
Figure 52. Refined mesh end view. The axial mesh spacing was also refined.
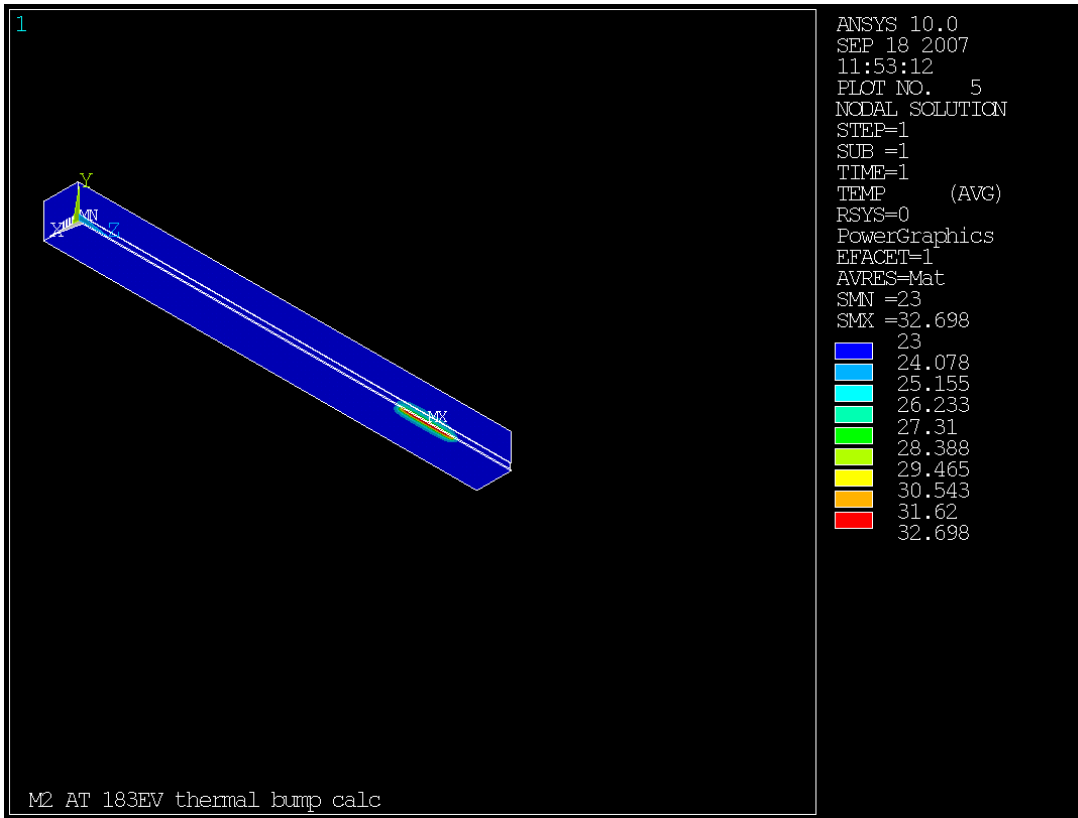
Figure 53. Maximum temperature rise above coolant bulk temperature with the refined mesh is 0.9% higher than coarse mesh run for same geometry & load case.
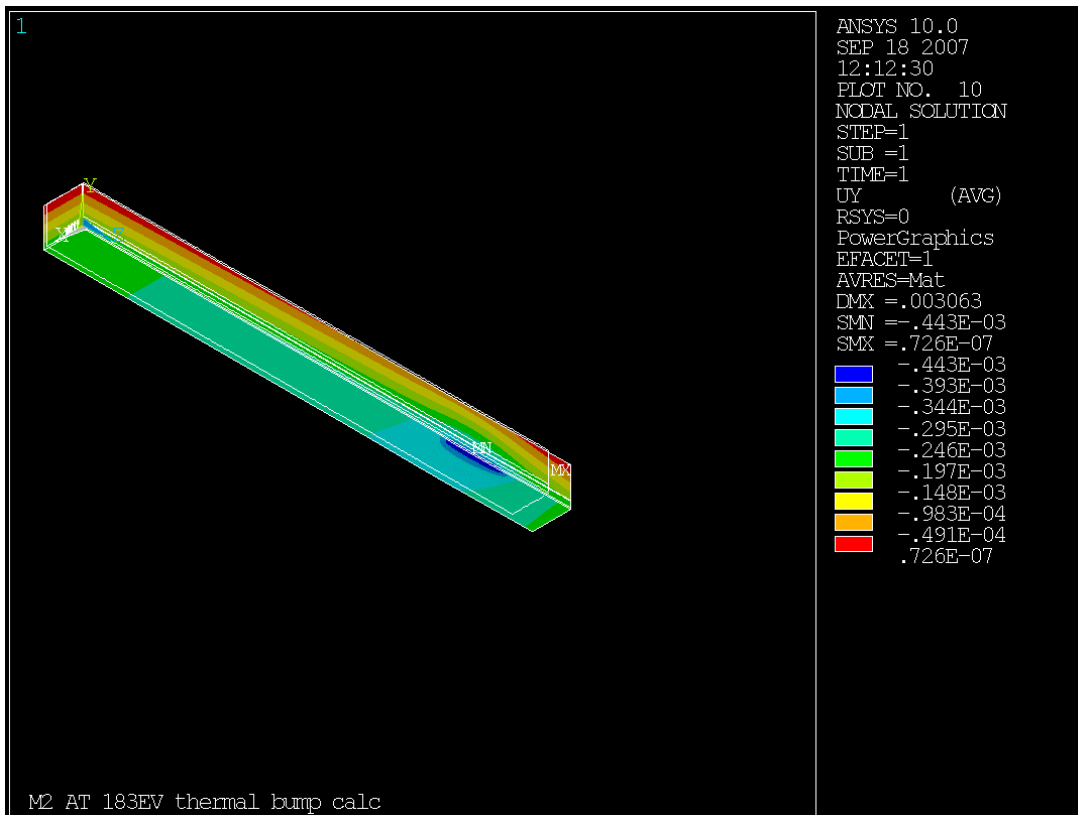

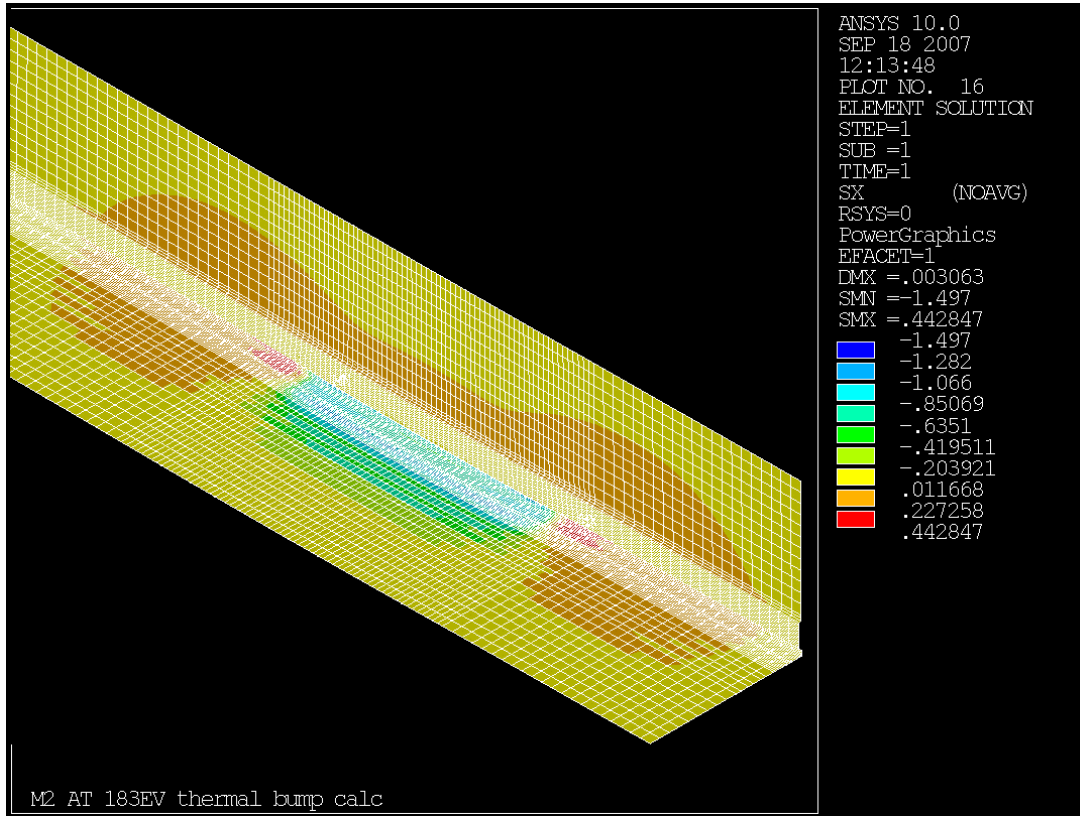**Figure 54. Refined mesh displacement in direction normal to the optical surface.**

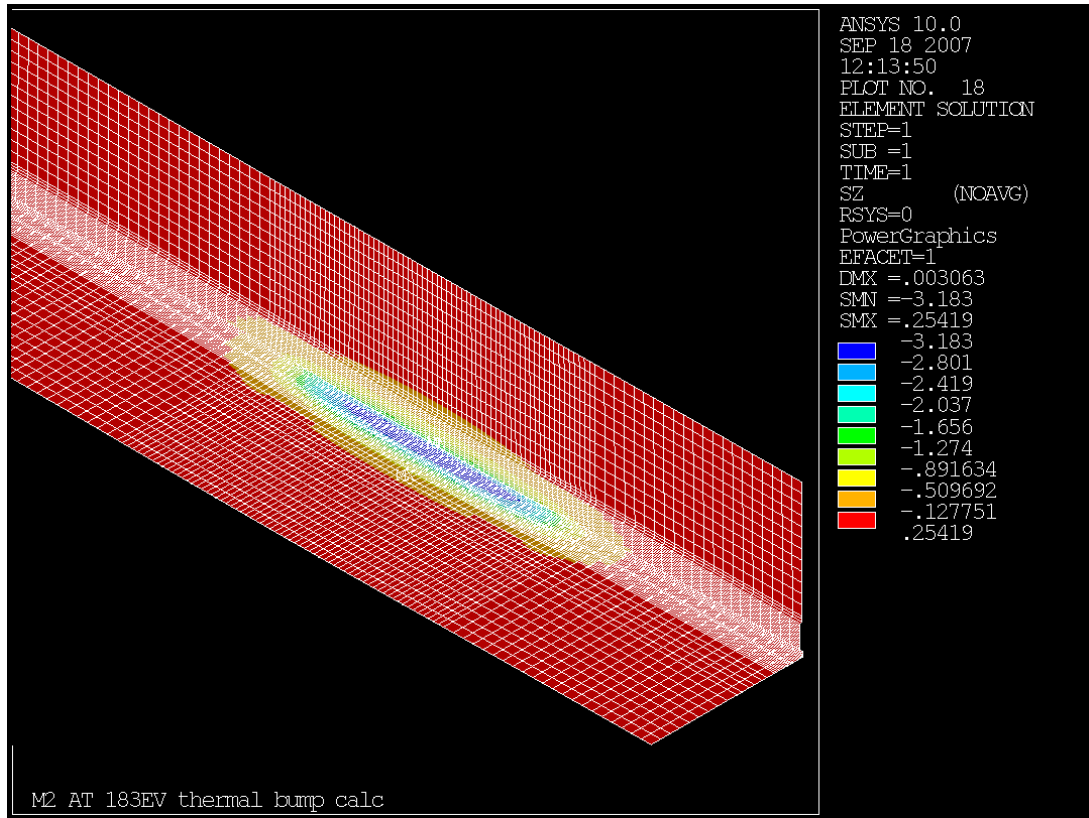**Figure 55. Refined mesh X axis stress.**

Figure 56. Refined mesh Z axis stress.

Table 2. Comparison of coarse and refined mesh 5-fin runs. The difference in slopes is largest at the edge sagittal value, at 11%.

Parameter	Coarse run	Refined run
Peak temperature, °C	32.612	32.698
Maximum displacement (which is axial), microns	3.062	3.063
Maximum normal displacement, microns	0.44175	0.44266
Maximum SDSG	0.48957	0.46697
Maximum SERR	0.124E-05	0.406E-06
SX extremes, N/mm^2	-1.403, 0.506	-1.497, 0.4428
SY extremes, N/mm^2	-0.2897, 0.4051	-0.3808, 0.3995
SZ extremes, N/mm^2	-3.176, 0.2272	-3.183, 0.2542
S3 extremes, N/mm^2	-3.176, 0.1052	-3.183, 0.0971
Meridional displ & slope, mm & microradians max	0.0004417, 13.91	0.0004426, 15.333
Central sagittal displ & slope, mm & microradians max	0.0004410, 21.2	0.0004419, 22.0
Edge sagittal displ & slope, mm & microradians max	0.0003543, 9.688	0.0003569, 10.77

Table 3. Comparison of 5-fin and 3-fin coarse mesh runs.

Parameter	Coarse 5-fin run	Coarse 3-fin run
Peak temperature, °C	32.612	32.679
Maximum displacement (which is	3.062	3.14

axial), microns		
Maximum normal displacement, microns	0.44175	0.457
Maximum SDSG	0.48957	0.69396
Maximum SERR	0.124E-05	0.146E-05
SX extremes, N/mm^2	-1.403, 0.506	-1.559, 0.4377
SY extremes, N/mm^2	-0.2897, 0.4051	-0.2710, 0.4281
SZ extremes, N/mm^2	-3.176, 0.2272	-3.156, 0.1867
S3 extremes, N/mm^2	-3.176, 0.1052	-3.156, 0.1442
Meridional displ & slope, mm & microradians max	0.0004417, 13.91	0.0004564, 13.99
Central sagittal displ & slope, mm & microradians max	0.0004410, 21.2	0.0004558, 20.86
Edge sagittal displ & slope, mm & microradians max	0.0003543, 9.688	0.0003683, 9.992

A requested run was with the length of heat spot increased from 48.046mm overall to 68mm overall. This was performed with the refined mesh.

Table 4. Comparison of refined mesh 5-fin base and extended heat spot runs.

Parameter	Refined base run	Extended spot run
Peak temperature, °C	32.698	32.719
Maximum displacement (which is axial), microns	3.063	3.111
Maximum normal displacement, microns	0.44266	0.472
Maximum SDSG	0.46697	0.45927
Maximum SERR	0.406E-06	0.421E-06
SX extremes, N/mm^2	-1.497, 0.4428	-1.476, 0.4559
SY extremes, N/mm^2	-0.3808, 0.3995	-0.3747, 0.3985
SZ extremes, N/mm^2	-3.183, 0.2542	-3.233, 0.2575
S3 extremes, N/mm^2	-3.183, 0.0971	-3.233, 0.0980
Meridional displ & slope, mm & microradians max	0.0004426, 15.333	0.0004721, 15.82
Central sagittal displ & slope, mm & microradians max	0.0004419, 22.0	0.0004697, 21.94
Z=331 sagittal displ & slope, mm & microradians max	0.0003569, 10.77 (downstream edge)	0.0004384, 21.54 (at Z=331, 10mm inside downstream edge of extended spot)

Extension of the heat spot lengthens the roughly cylindrical central portion of the normal displacements, improving the correctability of the distortions as intended. Normal displacements were provided to ray tracing to verify that.
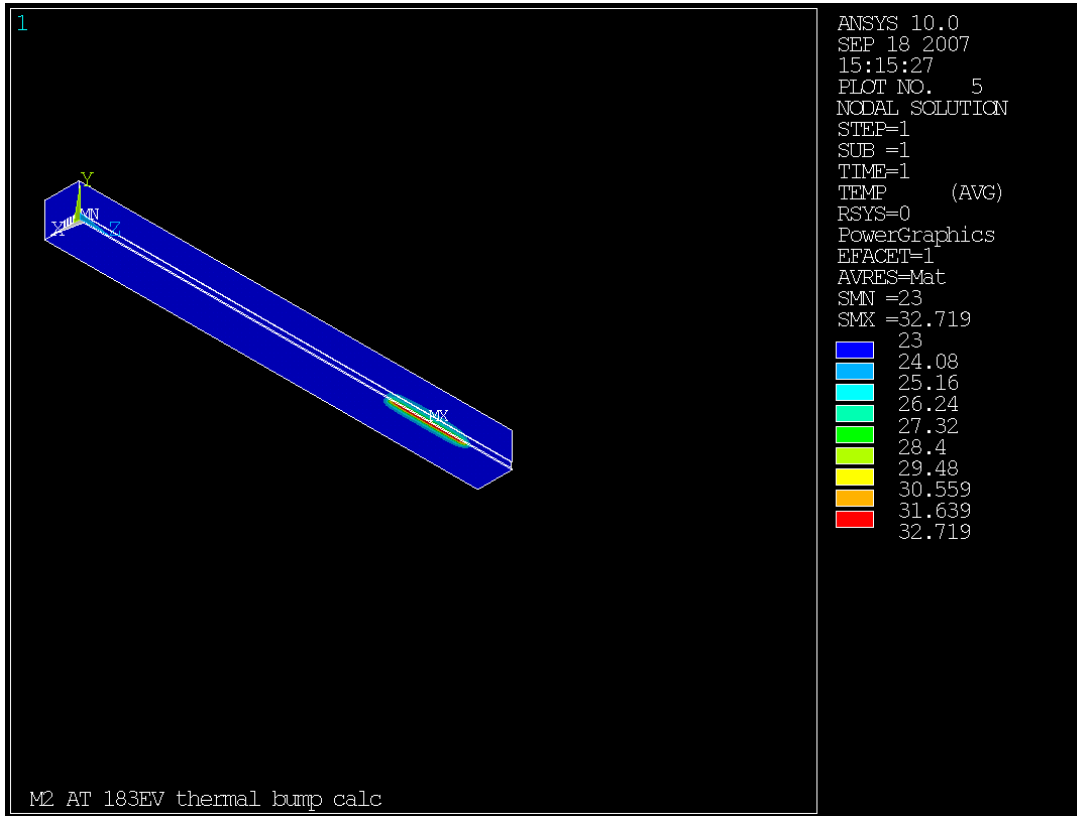

Figure 57. Temperature response of refined mesh 5-fin case with extended heat spot.
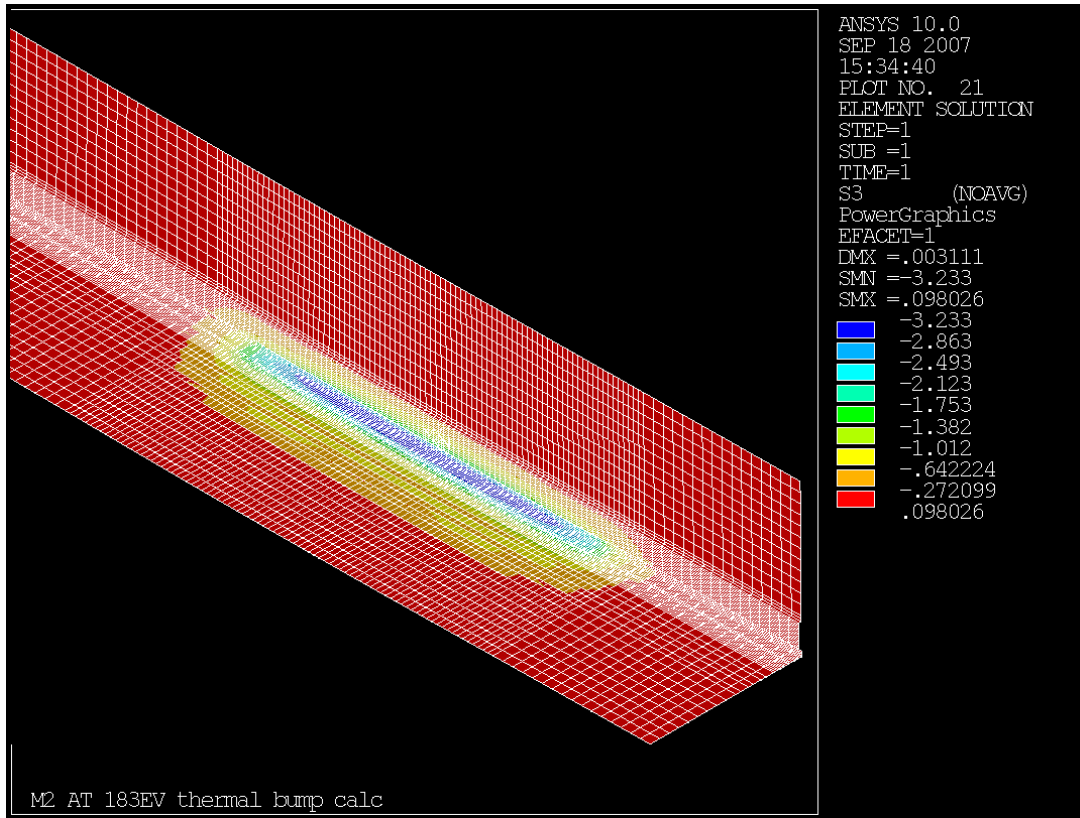
Figure 58. Refined mesh 5-fin case with extended heat load, showing third principal stress with mesh outline superimposed.

Stiffening the optic with a significantly thicker substrate appears to have only minor effects on slope, with 6% lower meridional slope and 6.3% higher edge sagittal slope.
Some results of the 100mm thick substrate case are shown below.

Table 5. Comparison of 100mm thick substrate to 30mm thick.

| Parameter	30mm	100mm
Peak temperature, °C	32.612	32.604
Maximum displacement (which is axial), microns	3.062	3.149
Maximum normal displacement, microns	0.44175	0.962
Maximum SDSG	0.48957	0.5159
Maximum SERR	0.124E-05	0.109E-05
SX extremes, N/mm^2	-1.403, 0.506	-1.45, 0.428
SY extremes, N/mm^2	-0.2897, 0.4051	-0.266, 0.4041
SZ extremes, N/mm^2	-3.176, 0.2272	-3.222, 0.2055
S3 extremes, N/mm^2	-3.176, 0.1052	-3.222, 0.0982
Meridional displ & slope, mm & microradians max	0.0004417, 13.91	0.000962, 13.08
Central sagittal displ & slope, mm & microradians max	0.0004410, 21.2	0.000962, 21.22
Edge sagittal displ & slope, mm & microradians max	0.0003543, 9.688	0.0008911, 10.30
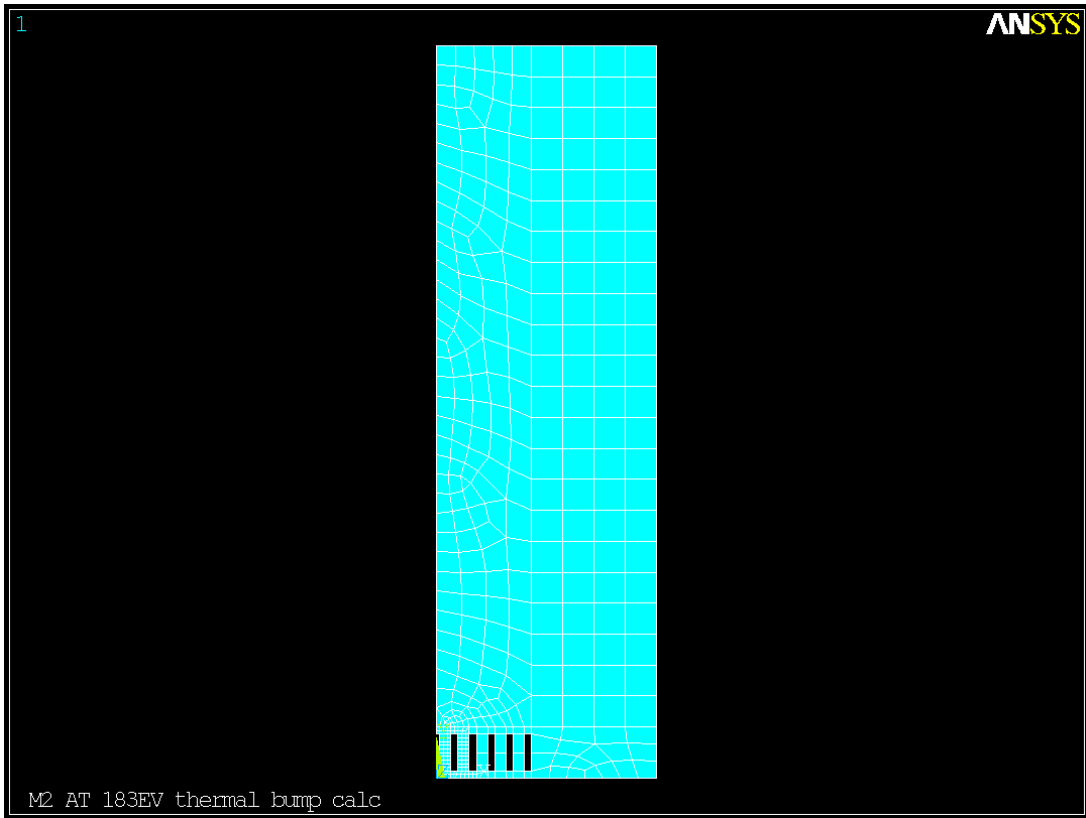
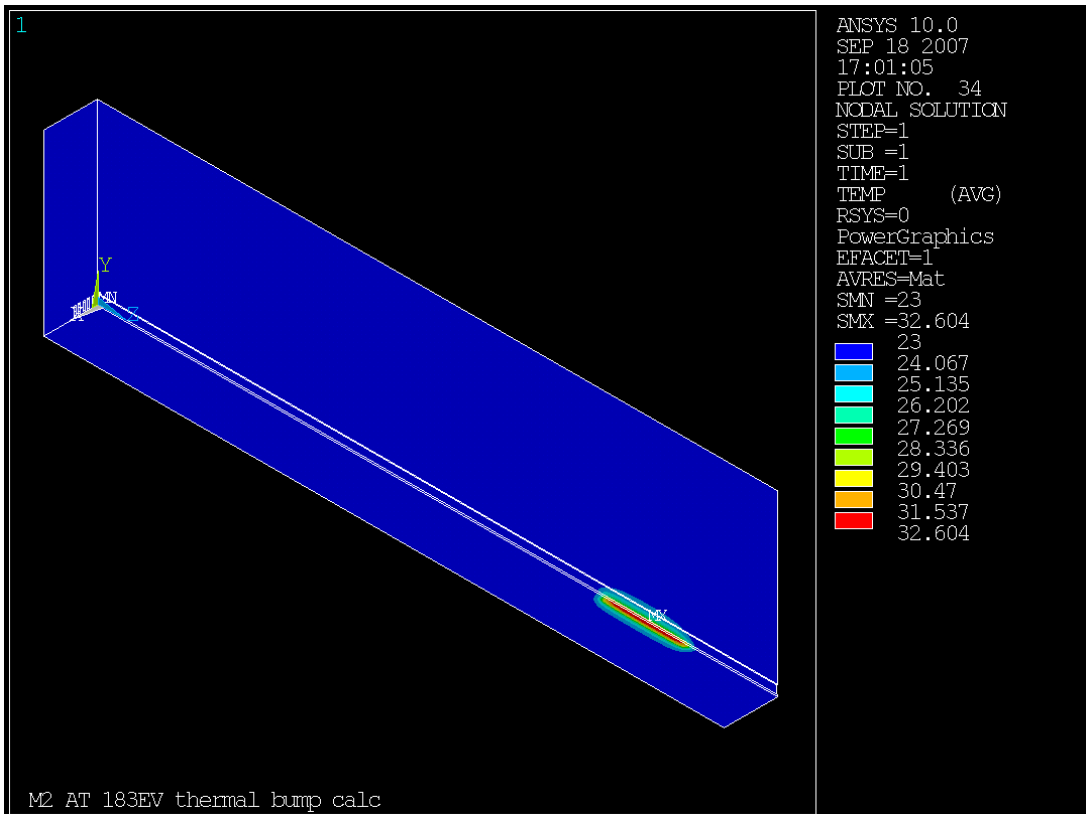**Figure 59. End view of mesh on 100mm thick case.**

Figure 60. Resulting temperature solution.
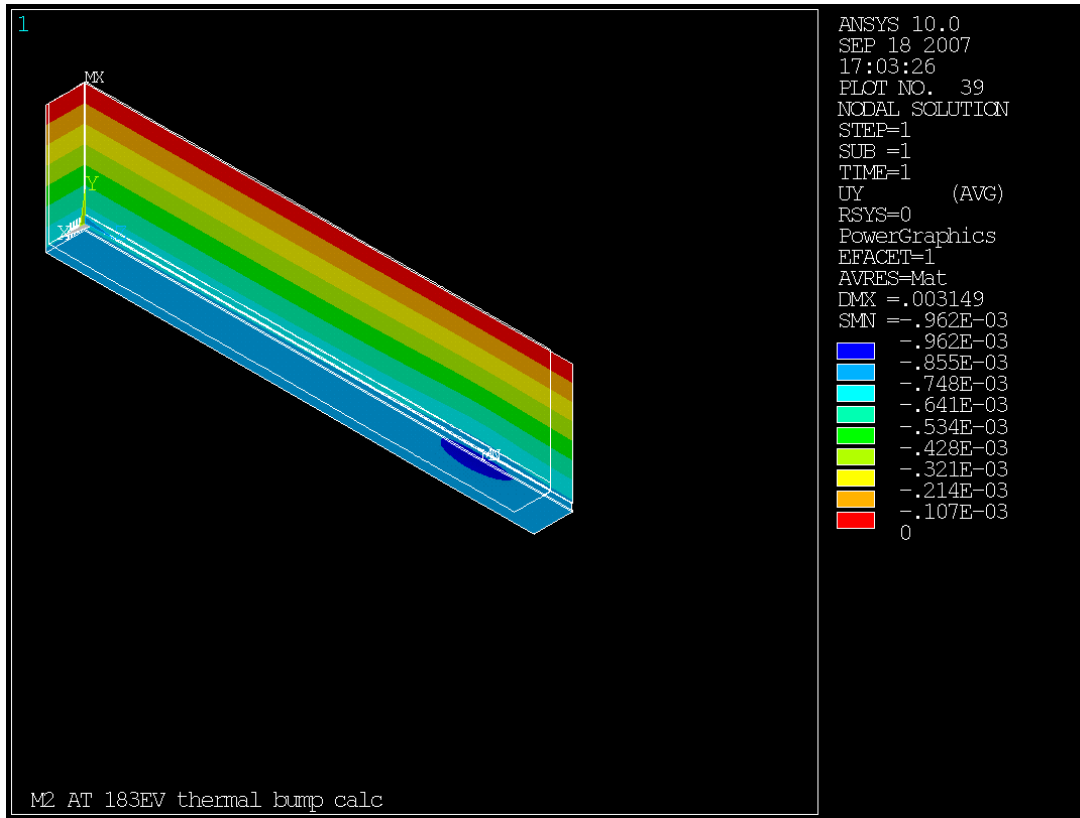
Figure 61. Displacement normal to the optical surface for 100mm thick substrate.
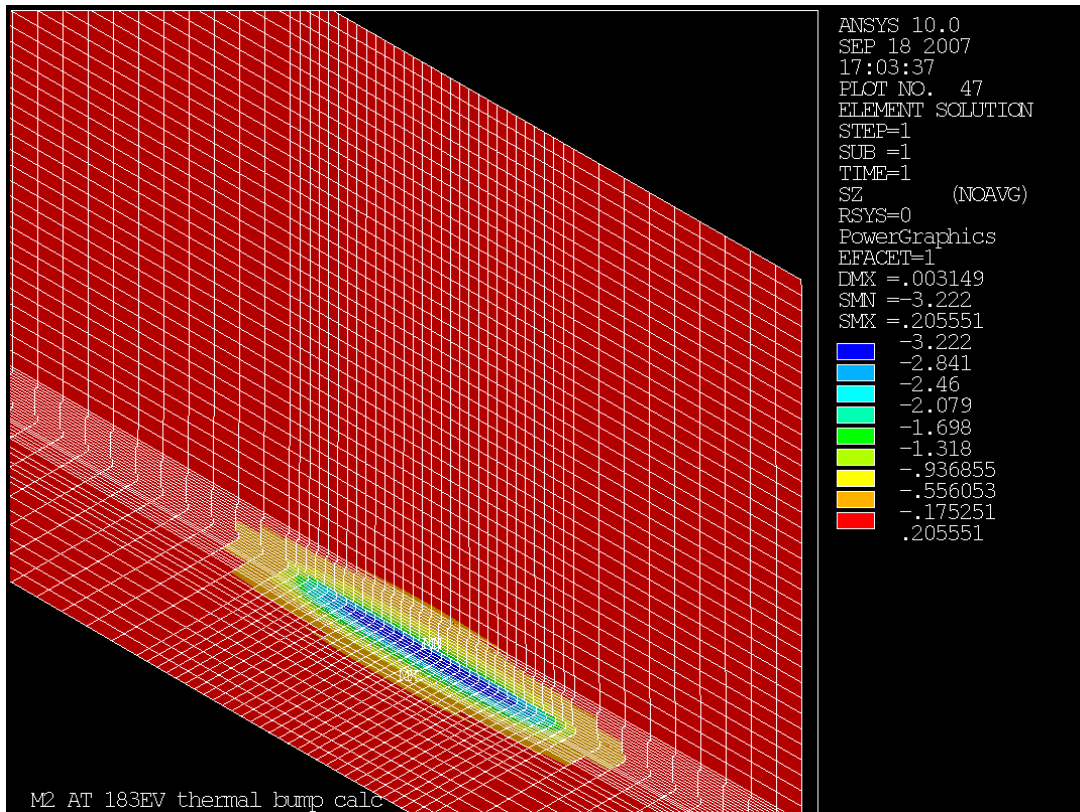

Figure 62. Z axis stress for 100mm thick substrate.

Summary

The M2 183eV operating case was selected for analysis as an expected worst case and determined to generate excessive distortion of the optical surface. A workaround was proposed, and simulated in ANSYS and in ray tracing, providing verification the workaround is sufficient to preserve optical figure at M2.

The 3-D parametric ANSYS model is adaptable to running many load and geometry cases. It still contains many approximations some of which should be removed in future design effort. With modification to handle generalized power density distributions, it will be applicable to additional optical elements in the beamline and additional beamline operating conditions. It is easily applicable to optimization studies. Variations in several variables were analyzed for effect on temperature and active optical surface shape. Evaluating surface slopes via path plots is an efficient way to forecast negative impact on ray tracing results & beamline performance.

The ANSYS outputs from differing meshes show that the temperatures and displacements reproduce well, and slopes to about 11% or better. Reproducibility of stresses is not as good; ANSYS measures of stress accuracy show that stress values from particular nodes & elements should not be relied on, as the values at a given node differ significantly among elements that have that node in common. However, the extreme values and the ranges of stress obtained reproduce reasonably well, and the extreme values are low in all cases. Peak thermal stresses obtained to date are low, below the level requiring acid etch. Stress concentrations and additional loads have not yet been examined. Uniform thermal expansion from reference temperature to (the slightly elevated) bulk coolant temperature is very significant in the overall displacement. These displacements were obtained with constraints applied at worst case locations (extreme ends of back surface) maximizing bulk expansion response and the effect of thermal bending on peak displacement. Real mirror mounting locations will straddle less than the optic's total length and so reduce the influence of thermal expansion on peak displacement. All simulation performed was steady state.